Fundamental Investigations into the Properties and Performance of Advanced Materials

by

Jacob J. Schichtel

A Dissertation Presented in Partial Fulfillment
of the Requirements for the Degree
Doctor of Philosophy

Approved May 2022 by the
Graduate Supervisory Committee:

Aditi Chattopadhyay, Chair
Lenore Dai
Anindya Ghoshal
Huei-Ping Huang
Yang Jiao
Jay Oswald

ARIZONA STATE UNIVERSITY

August 2022

ABSTRACT

Intelligent engineering designs require an accurate understanding of material behavior, since any uncertainties or gaps in knowledge must be counterbalanced with heightened factors of safety, leading to overdesign. Therefore, building better structures and pushing the performance of new components requires an improved understanding of the thermomechanical response of advanced materials under service conditions. This dissertation provides fundamental investigations of several advanced materials: thermoset polymers, a common matrix material for fiber-reinforced composites and nanocomposites; aluminum alloy 7075-T6 (AA7075-T6), a high-performance aerospace material; and ceramic matrix composites (CMCs), an advanced composite for extreme-temperature applications.

To understand matrix interactions with various interfaces and nanoinclusions at their fundamental scale, the properties of thermoset polymers are studied at the atomistic scale. An improved proximity-based molecular dynamics (MD) technique for modeling the crosslinking of thermoset polymers is carefully established, enabling realistic curing simulations through its ability to dynamically and probabilistically perform complex topology transformations. The proximity-based MD curing methodology is then used to explore damage initiation and the local anisotropic evolution of mechanical properties in thermoset polymers under uniaxial tension with an emphasis on changes in stiffness through a series of tensile loading, unloading, and reloading experiments. Aluminum alloys in aerospace applications often require a fatigue life of over 109 cycles, which is well over

the number of cycles that can be practically tested using conventional fatigue testing equipment. In order to study these high-life regimes, a detailed ultrasonic cycle fatigue study is presented for AA7075-T6 under fully reversed tension-compression loading. The geometric sensitivity, frequency effects, size effects, surface roughness effects, and the corresponding failure mechanisms for ultrasonic fatigue across different fatigue regimes are investigated. Finally, because CMCs are utilized in extreme environments, oxidation plays an important role in their degradation. A multiphysics modeling methodology is thus developed to address the complex coupling between oxidation, mechanical stress, and oxygen diffusion in heterogeneous carbon fiber-reinforced CMC microstructures.

ACKNOWLEDGMENTS

The completion of the research presented in this dissertation would not have been possible on my own. I would first like to express my appreciation to my advisor, Regents' Professor Aditi Chattopadhyay, for her guidance, encouragement, and advice throughout my doctoral studies. I am incredibly grateful for her support and supervision. I would also like to thank the members of my Supervisory Committee, Professor Lenore Dai, Professor Jay Oswald, Professor Huei-Ping Huang, Professor Yang Jiao, and Dr. Anindya Ghoshal for all their support and valuable feedback. I am thankful for the help and mentorship of Dr. Bonsung Koo, Dr. Siddhant Datta, and Dr. Karthik Rajan Venkatesan. I also would like to acknowledge Dr. Pedro Peralta and Dr. Luke Borkowski for their insights and discussions. In addition, I am grateful to all of my colleagues at Professor Chattopadhyay's research center including Khaled Khafagy, Ruslan Polichshuk, Mohamed Hamza, Md. Fazle Rabbi, Dr. Hyunseong Lee, Dr. Guoyi Li, Dr. Travis Skinner, Dr. Christopher Sorini, and Dr. Ashwin Rai for making the lab and office such a great place to work. Finally, I want to thank my friends and family for their encouragement and support.

I would also like to gratefully acknowledge the funding sources and program managers that supported the research presented in this dissertation. This research was supported by the National Defense Science and Engineering Graduate (NDSEG) Fellowship Program through the Air Force Office of Scientific Research (AFOSR) Sponsorship, the Office of Naval Research (ONR) under grant number N00014-17-1-2037 with program managers Dr. Anisur Rahman and Mr. William Nickerson, the ONR Defense University Research

Instrumentation Program (DURIP) award N00014-16-1-2012 through the use of the ultrasonic fatigue equipment, and the National Energy Technology Laboratory (NETL) under grant number DE-FOA-0001993 with program manager Matthew Adams.

TABLE OF CONTENTS

Page

CHAPTER Page

LIST OF TABLES

Table Page

LIST OF FIGURES

Figure Page

Figure Page

Figure Page

Figure Page

Figure Page

Figure Page

Figure Page

CHAPTER 1.

INTRODUCTION[*]

1.1. Background and Motivation

Since 1958 the Air Force has relied on its Aircraft Structural Integrity Program (ASIP) to ensure the structural safety of its aircraft while minimizing maintenance and replacement costs. The Air Force's ASIP is based on the philosophy of damage tolerance, which assumes the inevitable presence of flaws in materials and suggests an acceptable critical damage threshold, rather than relying on fail-safe redundancies or stringent safe-life requirements (Kim et al., 2006; Nees, 1995). Characterizing the material properties and understanding the evolution of damage in service loads and environments is crucial to predicting the remaining useful life (RUL). Materials used in aerospace engineering applications undergo many different types of mechanical and environmental loadings. Many load-bearing components of ground-transportation vehicles, airplanes, and wind turbines often experience 10^8-10^9 fatigue cycles over the course of the their lives (Mayer, 2016; L. Xu et al., 2018), and jet engine turbine blades regularly sustain temperatures over 1000°C, enabling additional degradation mechanisms including creep and oxidation (Khafagy, Sorini, et al., 2021). In addition to surviving conditions such as these, aerospace structures prioritize weight reduction to improve fuel efficiency, so maximizing the

[*] This chapter is based on the introductions in the author's previous publications (Schichtel et al., 2022; Schichtel & Chattopadhyay, 2019, 2020) and submitted manuscript (Schichtel & Chattopadhyay, 2022).

strength to weight ratio and minimizing overdesign are essential factors for aircraft components.

There is a large array of materials ranging from simple polymers and metallic alloys to advanced fiber-reinforced ceramic matrix composites, all with different distributions of properties such as weight, stiffness, fatigue strength, damage-tolerance, and heat and oxidation resistance. Thus, material systems must be carefully selected based on the given application and design requirements. Furthermore, informed designs require an accurate understanding of material behavior; any uncertainties or gaps in knowledge must be counterbalanced with heightened factors of safety, leading to overdesign. Therefore, building better structures and pushing the performance of new components requires an improved understanding of the thermomechanical response of advanced materials under service conditions. This dissertation provides fundamental investigations of some advanced materials: thermoset polymers, a common matrix material for fiber-reinforced composites and nanocomposites; aluminum alloy 7075-T6 (AA7075-T6), a high-performance aerospace material; and ceramic matrix composites (CMCs), an extreme-temperature material for high-efficiency turbine blades and other thermal applications.

1.2. Thermoset Polymers

Thermosetting plastics are made by mixing a hardening agent with a viscous liquid resin, which causes irreversible bonds to form between the polymer chains in the resin, creating a three-dimensional network of bonds in a process called curing. Thermosets are generally stiffer and stronger than thermoplastics, and they also have better performance

at high temperatures because the network of bonds helps them to maintain their shape. Thermosets such as cured epoxy resins have remarkable adhesive strength, high heat and chemical resistance, versatile manufacturability and relatively low cost, and their toughness can be substantially improved through the incorporation of reinforcement materials such as fibers and nanoparticles. These features make them one of the most common matrix materials for composites and substantiate their suitability for a wide range of applications from aerospace components and industrial coatings to electronic materials and biomedical systems (Domun et al., 2015; Jin et al., 2015; Rana et al., 2009). Conventional experimental methods for synthesizing and investigating the properties of new materials are slow and laborious. With the growth of data-driven computational material design strategies pioneered by the Materials Genome Initiative, the workflow for discovering and optimizing new thermoset materials is changing, reducing the need for the time-consuming trial-and-error approaches (Jain et al., 2013; Y. Liu et al., 2017; Ramprasad et al., 2017). Molecular dynamics (MD) simulations will be an important step both for developing and new materials without physical synthesis and testing, and for understanding matrix interactions with various interfaces and nanoinclusions at their fundamental scale. Though MD is not yet used as a primary validation tool for material development and characterization, with the improvement of molecular forcefields and the continued progression of computational capabilities, MD will likely prove to become increasingly valuable; so, it is imperative to establish logical frameworks to produce accurate, consistent data.

Although there has been increased research interest in the use of MD to understand material behavior, the majority of polymer research has been on linear homopolymers; the research of thermoset polymers is less comprehensive (C. Li & Strachan, 2015), likely due to the complexity of generating representative molecular structures. Ab initio quantum mechanical (QM) methods for modeling cure reactions are not feasible for large systems; even standard MD is generally limited to nanosecond timescales. The physical curing of thermoset polymers requires time on the order of minutes to days, so realistically representing the reaction physics of crosslinking under standard conditions at the atomistic scale is well beyond the capabilities of even the most powerful supercomputers. Thus, the introduction of some crucial assumptions is inevitable, and significant research efforts have been dedicated to developing reasonable techniques for generating these crosslinked network structures (C. Li & Strachan, 2015). Typical MD curing simulations do not capture the curing dynamics of crosslinking, reasoning that only the end result matters: a crosslinked structure that can be analyzed for properties (Yang & Qu, 2012). Coarse-grained MD simulations introduce additional assumptions by neglecting atomistic details to save computational expense (C. Li & Strachan, 2015). Early attempts at creating crosslinked systems involved using densely packed sets of manually pre-constructed oligomers to approximate a crosslinked system (Alian et al., 2015; Liao et al., 2009; Tack & Ford, 2008). However, these methods make weak assumptions about atomic connectivity and have since been replaced by more complex procedures.

The currently prevailing method for crosslinking utilizes an iterative multistep process for detecting and initiating bond changes based on a cutoff distance. This involves

activating reactive groups such as amines and epoxides as a preprocessing step and adjusting charges to maintain net neutrality (Demir & Walsh, 2016; C. Li, Medvedev, et al., 2012; C. Li & Strachan, 2010, 2011, 2015; Varshney et al., 2008; Wu & Xu, 2006; Yang & Qu, 2012). These simulations are usually performed at unrealistically high temperatures (≥500 K) to expedite curing (Demir & Walsh, 2016; C. Li, Medvedev, et al., 2012; C. Li & Strachan, 2010, 2011; Wu & Xu, 2006) and typically employ cutoff distances between 4 and 10 Å (C. Li & Strachan, 2015), well above the sum of the van der Waals radii. Some studies further increase the cutoff distance incrementally on successive iterations to achieve higher conversion degrees faster (Demir & Walsh, 2016; Varshney et al., 2008). Because bond lengths immediately following topology changes are significantly longer than their equilibrium lengths, periods of minimization and equilibration are required to avoid "blow up" errors. Most studies do not mention updating higher-order covalent bonding terms (angle, dihedral, improper), suggesting that these topological details were omitted. However, because these terms inevitably affect system dynamics, they should be updated as reported by Li and Strachan (C. Li & Strachan, 2010). After the desired crosslinking degree has been surpassed, the unreacted active sites are saturated with hydrogens, as discussed in (Demir & Walsh, 2016; Varshney et al., 2008; Wu & Xu, 2006; Yang & Qu, 2012). Alternatively, excess hydrogens may be eliminated during the curing simulation, depending on the manner of site activation (C. Li & Strachan, 2010, 2011). Finally, since the distribution of charges changes during cure reactions, the atomic partial charges are updated using methods such as the charge equilibration (QEq) method, the electronegativity equalization method (EEM), and the electronegative equalization-based

charge assignment (ECA) method (Demir & Walsh, 2016; C. Li & Strachan, 2010, 2011, 2015; Wu & Xu, 2006). The systems can then be cooled to operating temperatures.

Thermoset curing has proven to be a complex process, dependent on the specific constituents, cure environment, and the curing time-temperature profile (Jin et al., 2015), yet in addition to using high temperatures, large cutoff distances, and potentially neglecting higher-order covalent bonding terms, the above methodology disregards activation energy barriers. QM ab initio calculations can be used to optimize force field parameters and calculate activation energies by analyzing transition states (e.g., nudged elastic band method) (Henkelman et al., 2000), but their severe time and size constraints preclude their direct use for crosslinking simulations. Recently, Van Duin's group introduced a crosslinking methodology for simulating curing at moderate temperatures using reactive force fields (Vashisth et al., 2018). Their technique allows for a more accurate representation of the transition states, but the simulation requires significant manipulation of the reaction's activation energy by artificially providing energy to initiate reactions, and the system size is still quite limited compared to classical MD simulations. Li and Strachan demonstrated a two-stage chemistry model for MD to emulate activation energy discrepancies (C. Li & Strachan, 2010). In the first bonding stage, only primary amine reactions were permitted, and in the second, all reactions were enabled. This approach initiated the consideration of unequal activation energies in curing simulations, but it does not precisely quantify this integration specific activation energy values. Therefore, there is a need for a generalized MD crosslinking methodology that precisely integrates reaction dynamics and activation energy information.

Furthermore, understanding the initiation and progression of damage is essential for accurately modeling thermomechanical macroscopic material behavior beyond the elastic regime. Damage is distinct from other phenomena that involve permanent changes in a material such as hardening and plasticity because it encompasses the deterioration of a material's load carrying capability, as manifested in the degradation of stiffness. Continuum damage mechanics (CDM), which was originally introduced by Kachanov in 1958 and has since been further developed by Chaboche, Lemaitre, and many others, now provides a fully realized thermodynamic framework to describe the coupling effects between damage processes and stress-strain constitutive relations for practical engineering applications (Chaboche, 1988b, 1988a; Kachanov, 1986; Lemaitre, 1996). This framework rests on the assertion that damage is attributed to an effective volume loss due to the formation and coalescence of irreversible microdefects such as cracks and voids, which reduces the effective area over which a force is distributed, thus increasing the effective stress. The apparent continuum level stress is related to the effective stress through one or more damage parameters, which can be integrated into a thermodynamically consistent model through the application of internal state variable (ISV) theory to represent specific damage mechanisms (Coleman & Gurtin, 1967). This concept has been extended to account for numerous mechanisms such as nonlinear damage progression, anisotropic damage progression, and creep and fatigue damage, as well as damage specific to brittle or ductile materials or specific material architectures (Bonora, 1997; Chaboche, 1988b, 1988a; Matzenmiller et al., 1995; S. Murakami, 1988).

However, because damage models are predominantly defined phenomenologically to some extent, they are often only valid for very specific applications, or they require parameters that are difficult to determine experimentally. Sometimes these additional parameters are manually calibrated to fit specific experimental results, which can lead to skewed assessments of the accuracy of a model. Thus, there is a need to develop physics-based damage models that enhance fidelity and reduce empiricism. Multiscale modeling, which allows the modeling of physical mechanisms at the relevant length scale, is a natural progression for damage modeling since damage and macroscopic behavior occupy disparate length scales (Elliott, 2011). However, the complexities associated with accurately capturing damage initiation and propagating the information across the length scales remain a challenge. MD simulations can offer potential solutions to these issues by either directly establishing a damage evolution curve at the nanoscale or calculating parameters that are difficult to measure experimentally. Because MD simulations ideally make few assumptions beyond the specified boundary conditions and the choice of force field, they can be described as computational experiments. Thus, MD allows for a physics-based modeling methodology as opposed to explicitly detailing expected behaviors.

Bridging atomistic information to continuum scale damage and response is challenging due to the disparity in time and length scales. Initial attempts to bridge the length scales regarded the bond energy density of an MD system with a bond-order potential as a measure of bond breakage and connected it to a damage variable (Koo et al., 2016; Rai et al., 2017; Subramanian et al., 2017). However, the bond energy density may not directly correspond to bond breakage because plastic molecular reorientations and elastic stretching

also affect the bond energy density. Furthermore, the bond breakage in these studies was artificially augmented with ultra-high strain rates that exceed the atomic thermal vibration frequency, and bond breakage may not be the only cause of damage. In another study, a cumulative damage evolution index was developed based on atomic coordination numbers in a largescale Nickel system. However, a single unload-reload experiment did not exhibit stiffness degradation despite showing the nucleation and coalescence of nanovoids since they closed upon unloading (Cao & Wei, 2007).

A significant amount of research demonstrates the ability of MD to emulate various damage mechanisms. MD tensile tests performed on copper crystals with varying vacancy fractions exhibited decreasing Young's Moduli with increasing vacancy fractions (Chang, 2002). Unloading and reloading processes were performed on nickel nanowires post-yield, but stiffness degradation was not observed despite the stress drops and significant plastic deformation (Setoodeh et al., 2008). Hysteresis loops were obtained for the cyclic loading of thermoplastic polymers (Yashiro et al., 2010) and amorphous thermoset polymers (C. Li, Jaramillo, et al., 2012); yet the stiffness did not seem to diminish with successive cycling, despite the accumulation of plastic strains. Mechanically induced cavitation was demonstrated in a thermoset epoxy using classical force fields, although some major flaws in the system definition for this study prohibit a serious evaluation of the results (Neogi et al., 2018). Many more studies demonstrate the ability of MD to capture various additional damage mechanisms (Branicio et al., 2008; Cao & Wei, 2007; Devanathan et al., 2010; Komanduri et al., 2001; Meng et al., 2016; Potirniche et al., 2006; Seppälä et al., 2004; Szlufarska, 2006; Tang et al., 2010; Walsh et al., 2003; Yang & Qu, 2014). Nevertheless,

despite the myriad studies on damage related mechanisms in MD, there has been no reported study on damage initiation and progression in MD systems that directly connects to stiffness degradation in a material under mechanical loading.

1.3. Aluminum Alloys

Due to their high strength to weight ratio and relatively low cost, aluminum alloys have become integral to the aerospace industry. In particular, AA7075-T6, a heat-treated wrought aluminum alloy, is one of the most commonly used materials for highly stressed aerospace structures. Aircraft undergo significant cyclic loading making fatigue an essential consideration for reliability; in fact, fatigue is the single most common cause of failure (Bhaumik et al., 2008). Fatigue occurs when a component experiences cyclic stresses that are below the static strength of the material. Fatigue failure is generally divided into two main stages: crack initiation and crack growth, which is subdivided into stable crack growth and unstable fast fracture. Conventional fatigue testing utilizes servo hydraulic test machines to apply cyclic loads to a coupon at a frequency between 0.1 and 200 Hz (L. Xu et al., 2018). However, aluminum alloys in aerospace applications often require a fatigue life of over 10^8 or even 10^9 cycles, which is well over the number of cycles that can be practically tested at this conventional testing frequency (L. Xu et al., 2018). Reaching these high numbers of cycles requires a different testing approach: ultrasonic fatigue frames.

Study of fatigue in the ultra-high cycle regime is performed with ultrasonic fatigue testing equipment, which cycles at approximately 20 kHz using a piezo-electric converter

with a sonotrode to amplify displacements applied to the specimen. Although numerous ultrasonic fatigue testing systems exist (Ilie et al., 2020), they all operate under the same principles. Unlike traditional fatigue testing machines that use an external loading frequency different from the natural frequency of the specimen, ultrasonic testing equipment utilizes the natural frequency of the specimen to excite the axial tension-compression resonant mode. This allows the machine to produce relatively high strain in the specimen through a standing wave, despite the relatively low displacements applied to the end of the specimen.

Recent research studying fatigue in very high cycle regimes on the order of 10^6 to 10^{10} cycles (also referred to as ultra-high cycle regimes) has added complexity to the conventional understanding of fatigue and endurance limits (Newman, 2015). In the high cycle regimes (generally on the order of 10^4 to 10^6 cycles), materials largely exhibit an apparent endurance limit in which increased cycling does not induce failure, cracks generally initiate at defects on the surface of the specimens, and the effects of the cycling frequency are not thought to significantly influence the fatigue life. However, the invention of ultrasonic fatigue testing frames enables higher testing cycle counts, which in turn challenge these traditional understandings of fatigue. Numerous different ultrasonic fatigue frame designs have been used with various specimen geometries to study various metals with different fabrication methods and treatments under different types of fatigue loading and loading environments, as has been summarized in Mayer's recent review article (Mayer, 2016). However, the understanding of fatigue conducted at ultrasonic frequencies

is still not as well developed as that of fatigue tested at conventional frequencies, and there are still some areas of study which are not fully understood.

The effects of cycling frequency on the results of fatigue testing are important to consider because the results of fatigue tests conducted under ultrasonic frequencies may not be directly applicable to applications that cycle at more typical frequencies. The intensity of the effects of frequency on fatigue life is material dependent, with aluminum alloys (both cast and wrought) generally exhibiting low frequency dependence (Caton et al., 2003; Holper et al., 2003; Mayer, 2016; Mayer et al., 2001, 2013; Papakyriacou et al., 2002; Stanzl-Tschegg et al., 2012), especially compared to low-carbon and medium-carbon steels (Guennec et al., 2014; Mayer, 2016). The "frequency effect", which generally results in increased fatigue strength, can be attributed to several competing factors including increased strain rate, internal temperature, and reduced environmental effects. Because the plastic deformation of face-centered cubic (fcc) crystal systems is known to be relatively insensitive to cycling frequency, the high strain rate induced by ultrasonic cycling frequencies is thought to have little impact on fatigue strength of aluminum alloys. Therefore, any frequency effects observed in aluminum alloys are attributed to the impact of frequency on environmental degradation rather than the strain rate (Holper et al., 2003; Schneider et al., 2016). Indeed, some studies show significant frequency effects for aluminum alloys, attributed to environmental influences (Schneider et al., 2016; Zhu et al., 2008). In addition, while some metals such as steel undergo a transition from surface initiations to interior crack initiations (fish-eye failures) around 10^6 cycles (Kirkham & Liaw, 2002; Sakai et al., 2001, 2010), aluminum alloys are often thought to primarily

experience surface initiations even in the very high cycle regime (Bathias et al., 2001; Lesperance et al., 2021; Mayer et al., 2013; Y. Xue et al., 2007). Nevertheless, consensus has not yet been reached as some studies show subsurface failures in the very high cycle regime (Gao et al., 2020; Stanzl-Tschegg et al., 2016; L. Xu et al., 2018).

Aluminum alloys are typically thought not to have an endurance limit (Kirkham & Liaw, 2002; Mayer, 2006, 2016; Mayer et al., 2001; Takahashi et al., 2014), although some studies suggest that there may still be a limit in the very high cycle regime (He et al., 2015; Wang et al., 2006, 2010; L. Xu et al., 2018). Size effects on fatigue life are well documented for ultrasonic fatigue testing, particularly for steel (Furuya, 2011; Paolino et al., 2014; H. Xue et al., 2018), though some aluminum alloys with special processing don't appear to exhibit any size effects (Stanzl-Tschegg et al., 2012). Some fractographic studies have analyzed the fracture surfaces of AA7075-T6 subjected to ultrasonic fatigue (Arcari et al., 2012; Gao et al., 2020; Stanzl-Tschegg et al., 2016; Wang et al., 2010), but these studies are limited in scope and show different fracture features, leaving room for a more comprehensive fractographic analysis under standard conditions. In addition, the effects of surface mechanical attrition treatment (SMAT) have been studied recently for AA7075-T6 under ultrasonic fatigue loading, but this is different from typical abrasive roughness because it involves compressive impact loadings that generate local plastic deformation, which actively strengthens the surface region and can thus improve life despite the increase in surface roughness (Gao et al., 2020). In addition, given that the probability of subsurface failures increases with decreasing load and increasing life, it is unclear whether the surface roughness has greater impact in the high cycle regime than the very high cycle regime.

Based on conventional fatigue studies, one would expect fatigue life to diminish with increasing surface roughness, but to the best of the authors' knowledge, this has not yet been explicitly studied in the ultra-high cycle fatigue regime where internal crack initiations are more prevalent.

Furthermore, there are currently no American Society for Testing and Materials (ASTM) standards for ultrasonic fatigue testing. Finite element analyses (FEA) have been performed to develop various designs and calculate stress distributions (Almaraz et al., 2017; Lesperance et al., 2021; Myung & Choi, 2016; Paolino et al., 2014), but no probabilistic studies have yet been conducted to analyze the sensitivity of the resonant frequency and stress amplitude to variations in geometry and material properties. Nonetheless, because ultrasonic fatigue testing depends on the resonant frequency of the specimen, the accuracy of test specimen dimensions affects ultrasonic fatigue experiments in multiple ways. In addition, ultrasonic fatigue testing requires a small specimen size in order to attain axial tension compression resonant modes at 20 kHz so small differences in geometry can lead to greater effects on stress distributions. Therefore, although a considerable number of studies have been reported on aluminum alloys subjected to ultra-high cycle fatigue testing, more work must be done to further understand some of these fundamental ideas.

1.4. Ceramic Matrix Composites

CMCs offer better high-temperature performance and lower density compared to metals and superalloys, and they demonstrate several significant improvements over

monolithic ceramics including increased toughness, more gradual failure modes, good creep and oxidation resistance, and thermal shock stability at high temperatures (Arai et al., 2019; Borkowski & Chattopadhyay, 2015; LEWIS, 2000). As a result, CMCs are an attractive material for high-temperature applications such as hot-section jet engine components and hypersonic flight applications, which are targeted to withstand temperatures over 1500°C (Bale et al., 2013; Goldberg, 2012; Goldsmith et al., 2015).

Monolithic ceramics are typically hindered by their inherent brittleness; they tend to fail suddenly and without warning. CMCs overcome this setback with fiber bundles and specially designed weaves, which can adequately impede local damage and prevent catastrophic failures through various toughening mechanisms such as fiber/matrix debonding, crack deflection, crack bridging, transformation toughening and fiber pullout (Bale et al., 2013). The interface between fibers and the matrix is made intentionally weak by the coatings applied to the fiber in order to enable these damage propagation mechanisms; if the interface was strong, CMCs would fail similar to the brittle failures of monolithic ceramics. As load is applied to CMCs, microcracks nucleate in the matrix from voids or matrix flaws due to the inherent stress concentrations and propagate until they encounter a fiber. The weak interfacial bond fails and allows the fibers to slide, relieving some of the crack intensity through these crack deflection and frictional sliding energy dissipation mechanisms. More cracks propagate through the matrix in this manner until enough energy is dissipated or the material fails (Tracy, 2014). The irregular CMC microstructure is also key to CMC performance. The CMC manufacturing processes such as chemical vapor deposition (CVD), polymer infiltration and pyrolysis (PIP), chemical

vapor infiltration (CVI), and liquid silicon infiltration (LSI) inevitably lead to unevenly shaped and randomly distributed voids. This porosity leads to variability in material properties, which is one of the significant obstacles to CMC application.

Carbon fiber-reinforced silicon carbide matrix (C/SiC) CMCs are one of the most widespread fiber-reinforced CMCs and are already in use for aero engine exhaust nozzle flaps, nose cones, and brake discs (An et al., 2021; Longbiao, 2015), but the carbon fibers are thermodynamically unstable in the presence of oxygen (BAXTER & FORDHAM, 2000; Jacobson et al., 2001; Yin et al., 1994). The development of better environmental barrier coatings (EBCs) that minimize CMC oxidation and volatilization is an ongoing area of largely confidential research (K. N. Lee et al., 2021). At temperatures above ~800°C, the SiC matrix tends to react with oxygen to form a protective viscous silica (SiO_2) layer that fills microcracks reduces oxygen ingress to the fibers and fiber interphases, but mechanically induced damage and the time spent transitioning to service temperatures still pose serious risk of component oxidation.

Environmental studies have shown that there are two primary regimes for the oxidation of carbon fibers in C/SiC CMCs: the reaction-controlled regime and the diffusion-controlled regime. Tests conducted at lower temperatures are reaction-limited, while tests performed at higher temperatures are typically diffusion limited, with the transition temperature lying somewhere between 600°C and 1000°C (Halbig, 2008; Halbig et al., 2008; Halbig & Cawley, 2008). This transition temperature ultimately depends on the ratio between effectivity diffusivity and the reaction rate, which is affected by the stress, the environment, and the porosity, tortuosity, and constrictivity of the microstructure. CMCs

contain a high density of defects due to the manufacturing process, which have been shown to significantly impact their constitutive response (Borkowski & Chattopadhyay, 2015; Goldsmith et al., 2013; Khafagy, Datta, et al., 2021; Skinner & Chattopadhyay, 2021). Tensile stresses in CMCs produce microcracks and open existing microcracks in the matrix, which serve as airflow channels for oxygen, thereby increasing the rate of oxidation. Thus, the size, distribution, and morphology of these manufacturing induced micro-cracks and porosity effect not only the mechanical response but also the oxidative response (BAXTER & FORDHAM, 2000; Yu et al., 2021). This coupling between damage and oxidation causes C/SiC CMCs constant stress tests at high-temperature to exhibit creep-like strain behavior with the strain increasing over time, eventually accelerating toward final failure. This response, is causally distinct from creep with experimental tests having shown that this creep-like strain response can occur at temperatures below the creep regime (Halbig et al., 2008). Therefore, the heterogenous, highly variable microstructure of CMCs combined with an oxidative, high-temperature service environments leads to complex thermal-chemical-mechanically dependent behavior.

1.5. Objectives

Following are the principal objectives of this work:

1. Develop a more efficient and accurate method for creating MD crosslinked networks using the underlying physics of curing.
2. Study damage in thermoset polymers at the atomistic scale and investigate the efficacy of using MD based damage models.

3. Analyze the fracture surfaces of AA7075-T6 under ultrasonic fatigue loading and evaluate the size effects, surface roughness effects, and frequency effects across different fatigue regimes.
4. Model the complex coupling between oxygen diffusion, carbon fiber oxidation, and damage in CMCs across the different temperature regimes.

1.6. Outline

The document is structured as follows:

Chapter 2 establishes an improved proximity-based MD technique for modeling the crosslinking of thermoset polymers. The molecular structures are analyzed based on the incorporation of cure temperature, cutoff distance, and reaction probability into the Arrhenius equation, providing important insights into the pitfalls of some commonly used assumptions in crosslinking simulations. For validation, a variety of these systems are tested for their ability to capture the effects of temperature and crosslinking degree on material properties.

Chapter 3 uses the all-atom MD methodology established in Chapter 2 to study damage initiation and the local anisotropic evolution of mechanical properties in thermoset polymers under uniaxial through a series of tensile loading, unloading, and reloading experiments. The efficacy of incorporating MD damage data into multiscale models is evaluated considering the sensitivity of results to topological variation.

Chapter 4 presents a detailed study of AA7075-T6 under ultrasonic fatigue loading. The geometric sensitivity, frequency effects, size effects, surface roughness effects, and

the corresponding failure mechanisms for ultrasonic fatigue across different fatigue regimes are investigated. Fatigue-fracture behavior is evaluated via detailed scanning electron microscopy (SEM) fractography, and sensitivity studies conducted using FEA based modal analyses and probability studies determine dominating sources of life variability for typical ultrasonic fatigue specimens.

Chapter 5 proposes a multiphysics methodology and corresponding numerical scheme for modeling the complex interactions between oxygen diffusion, matrix cracking, oxidation, and the state of stress in C/SiC CMCs at the microscale. The developed model is implemented and tested using FEA simulations of various stressed and unstressed oxidation tests of stochastic representative microstructures to analyze strain acceleration behavior and the fundamental differences between the reaction-limited and diffusion-limited regimes.

Chapter 6 reviews the major contributions of this work and discusses the future work of addressing the complex coupling between oxygen diffusion, oxidation reaction, anisotropic damage, and deformation in typical material architectures using a custom finite element.

CHAPTER 2.

IMPROVED MOLECULAR DYNAMICS CROSSLINKING METHODOLOGY[*]

2.1. Introduction

This chapter explores the exceptional capabilities of an improved proximity-based MD technique for modeling the crosslinking of thermoset polymers. The novel methodology enables realistic curing simulations through its ability to dynamically and probabilistically perform complex topology transformations while selectively minimizing high potential energy groups. The molecular structures are analyzed based on the incorporation of cure temperature, cutoff distance, and reaction probability into the Arrhenius equation, providing important insights into the pitfalls of some commonly used assumptions in crosslinking simulations. In addition, this work discusses the necessity of using thermal disturbance to break metastable configurations. Finally, a variety of these systems are tested for their ability to capture the effects of temperature and crosslinking degree on material properties. This leads to new perspectives for the strain hardening phenomenon, the sensitivity of stiffness calculations, and the evolution of the Poisson's ratio. A holistic view of the glass transition temperature (T_g) is demonstrated through its manifestation in each of these mechanical properties.

A novel proximity-based reaction algorithm developed by Gissinger et al. (Gissinger et al., 2017) is utilized for creating complex polymer networks and its probabilistic features

[*] This chapter is based on the author's previously published journal article (Schichtel & Chattopadhyay, 2019).

are exploited to establish a formulation for incorporating activation energy information into curing simulations via collision theory and the Arrhenius equation. The capabilities of this reaction algorithm have been under-recognized; its advantages are multifold. The algorithm efficiently integrates reactions into isothermal-isobaric (NPT) and isothermal-isochoric (NVT) simulations, eliminating the need for an iterative approach and more accurately representing system dynamics. This incidentally allows for precise determination of crosslinking degree, since topology changes occur continuously rather than all at once at the end of each iteration. All bonded and nonbonded terms (including higher-order covalent terms and partial charges) are updated dynamically. This prevents inaccurate hinge-like molecular linkages that result from neglecting angle-based covalent terms and eliminates the need for external charge equalization techniques, which can be computationally expensive for large-scale simulations (C. Li & Strachan, 2010). In addition to these advantages, the generalized framework is simpler to use than the current methods and can be easily adapted for different constituents and incorporating nanoreinforcement materials.

This methodology is used to study the effects of temperature, cutoff distance, activation energy probabilities, and random seeds on reaction rates and ratios, which provides essential insights into the pitfalls of some commonly used assumptions in crosslinking simulations. The need for using elevated temperatures to improve the molecular structure of a polymer network is disambiguated, as this process mimics the results of computationally impassable reaction kinetics by perturbing metastable molecular configurations. Finally, a variety of these systems are subjected to uniaxial tensile tests to

examine their ability to capture the effects of temperature and crosslinking degree on strength, stiffness, and the Poisson's ratio. This provides a holistic view of the T_g through its manifestation in these mechanical properties and evokes new perspectives for the strain hardening and softening phenomena, the sensitivity of stiffness calculations, and the dependence of the Poisson's ratio on the state of deformation.

2.2. Crosslinking Methodology

2.2.1. Initialization

The all-atom MD simulations were performed in LAMMPS (large-scale atomic/molecular massively parallel simulator) (Plimpton, 1997). A general-purpose classical force field, the Merck Molecular Force Field (MMFF) was implemented using parameters generated from SwissParam (Zoete et al., 2011) and reformatted for use in LAMMPS, though this framework should work for any classical force field. Harmonic functions were used for the bond, angle, and improper potentials, and the CHARMM (chemistry at Harvard macromolecular mechanics) functional form was used for dihedral interactions. The particle-particle particle-mesh (PPPM) method was used to capture long-range coulombic interactions in K-space, and Lennard Jones force switching functions were used for the pairwise interactions with a cutoff of 10 Å. This is therefore a complete classical force field, which demonstrates the full functionality of this methodology. Although the parameters used were not specifically developed for these constituents, this

force field has been previously proven to yield accurate T_g results for these constituents (Koo et al., 2014).

For this study, diglycidyl ether of bisphenol-F (DGEBF) also known as EPON862 or bis F, one of the most common epoxy resins (Domun et al., 2015), was used with the curing agent, diethylenetriamine (DETA), as shown in Figure 2.1. This hardener has a slightly more complex implementation compared to the more commonly used hardener diethyltoluenediamine (DETDA) since it contains a secondary amine group in addition to the two primary amine groups. As has been done for DGEBF and DGEBA in other simulations, DGEBF were employed without any repeated units (Demir & Walsh, 2016), due to the unavailability of relevant data for this molecule in published literature. However, it is worth noting that varying the number of repeat units will affect both the molecular weight between crosslinks (M_C) and the relationship between the weight and stoichiometric ratios, thus altering the structure and properties. For all simulations, 695 DETA molecules and 850 DGEBF molecules were used for a total of 50,450 atoms, thus maintaining the experimental weight ratio of 100:27 for DGEBF to DETA (Sun et al., 2008). This large system size was chosen to reduce measurement noise and fluctuations, especially for pressure, which is fundamental for stress calculations. Furthermore, size-dependence is markedly reduced for larger systems due to the increased degrees of freedom; Li and Strachan found that relatively large systems (16,000 to 65,000 atoms) exhibit only weak size-dependence (C. Li & Strachan, 2015).

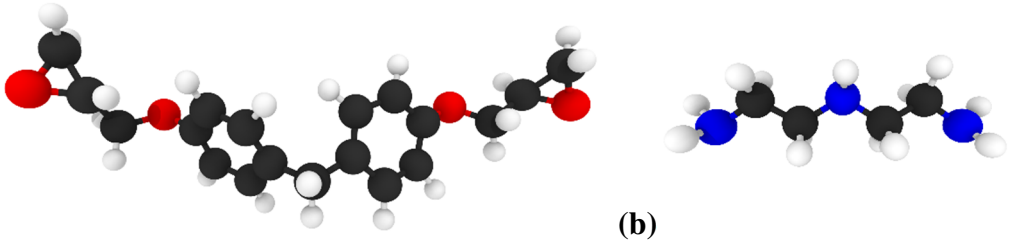

(a) **(b)**

Figure 2.1. Molecular Structures of (a) the DGEBF Resin and (b) the DETA Hardener.

The Packmol software (Martínez et al., 2009) was used to initially distribute molecules in the simulation. All molecules were randomly dispersed, as has been done in the previous studies (Demir & Walsh, 2016; C. Li & Strachan, 2010, 2011; Tack & Ford, 2008; Varshney et al., 2008; Yang & Qu, 2012). This assumption neglects the role of molecular diffusion on the resultant structure, but molecular diffusion at standard temperatures is too slow to be modeled within current computational limits. Nevertheless, this assumption should have a minimal impact on the structure given the isotropy of polymeric materials even at the microscale. Periodic boundaries were applied in all directions. After the molecules were distributed, energy minimization was performed to lower the high potential energy of the initial configuration. Prior to crosslinking, the liquid systems were fully equilibrated with 20 ps of NVT simulation followed by 500 ps of NPT simulation at atmospheric pressure and curing temperature. The conjugate gradient method was used for all minimization procedures, and Nose-Hoover thermostats and barostats were used to control the temperature and pressure with standard damping coefficients and 0.5 drag during the relevant time integration steps. Newton's equations of motion were integrated with 1 fs timesteps.

2.2.2. Crosslinking Procedure

The superimpose algorithm of the bond/react function in LAMMPS modifies molecular topology during time-integrated MD simulations based on custom-defined cutoff distances and probabilities. When two corresponding bonding atom types fall within a specified cutoff distance, the algorithm examines the surrounding topologies to determine whether they match the pre-reaction templates, which include all bonded, van der Waals, and electrostatic interactions. If they match the templates and the pre-defined probability is met, then the topological changes are executed according to the reaction map and post-reaction template. Because these sudden changes in covalent definitions result in high energy configurations, the reactive sites are subjected to an adjustable minimization period. The details of the superimpose algorithm are discussed more comprehensively by Gissinger et al. (Gissinger et al., 2017). The reaction maps, templates, and adjustable parameters require meticulous definition to attain the desired results. Note that the number of maps needed to describe all possible reactions increases multiplicatively when the bonding descriptions of neighboring reactive sites are coupled. For example, if two unique reactive groups are within two bonds of each other, their dihedral terms may overlap, which necessitates templates for both the reacted and unreacted cases. With the constituents in this study, only three maps are needed, but if the central amine was coupled to the primary amines, then seven maps would be required.

Using this reaction procedure for dynamic crosslinking simulations provides several distinct advantages over today's dominating MD methods. The template mapping process eliminates the need for preprocessing activation and post-processing hydrogenation steps

and preserves the true topology of the unreacted sites. The built-in topology conversion process greatly simplifies topology transformation, avoiding the need for additional charge equalization processes and automatically converting higher-order bonding terms, thereby preventing hinge-like crosslinks caused by incomplete bonding descriptions. Furthermore, having bond formation integrated into NPT simulations deposes the iterative approach and more accurately emulates the system's dynamics: viewing the trajectory files confirms elegant transitions. Due to the continuous nature of bond formation and selective minimization, the speed of crosslinking simulations may also increase, making lower curing temperatures and cutoff distances more accessible, the benefits of which are discussed in Section 2.2.3. Because the topological changes occur continuously during NPT simulations rather than concurrently at the end of each iteration, this procedure permits more precise control of the crosslinking degree. The probability feature can also be exploited to provide new functionality for tuning reaction rates as detailed in Section 2.2.3. This generalized framework can be easily adapted for employing different constituents and incorporating nanoreinforcement materials, as well as for constructing structures that can be further investigated with reactive force fields.

The cutoff distance was set to 3.25 Å, the sum of the van der Waals radii, as justified in Section 2.2.3, unless otherwise specified. Although the methodology is capable of modeling multistep reactions, the crosslinking reactions were modeled in a single step. This approach may actually be a better representation, especially when the first elementary reaction is the rate-determining step (RDS) because it avoids the intermediary minimization periods that may prolong the transition states. These topology changes

violate the conservation of momentum, so the net momentum was periodically removed to avert system drift. The function allows the custom definition of the maximum distance reacting atoms can travel during minimization, as well as the number of minimization steps for each reaction. These are complementary parameters since the maximum atom travel distance affects the amount of minimization required to stabilize the reaction. For the constituents in this study, the rate of crosslinking increases for lower minimization periods because it advances the availability of the secondary amine reaction. However, higher maximum travel can significantly increase the temperature of the system, since the temperature is proportional to the average of the atomic velocities squared. The speed of each reacting atom was limited to 0.05 Å per fs timestep, which, for this cure temperature, ranks the kinetic energy of a hydrogen atom traveling at this speed just within the top 5% of all atoms in the system, as calculated from the Maxwell-Boltzmann kinetic energy distribution. Thus, this designation limits the speed of reacting atoms to a reasonable value. After some preliminary experiments, a corresponding minimization period of 100 timesteps was selected. Together, these parameters balance kinetic energy influence and system stability with the duration of the minimization period.

2.2.3. Incorporation of the Arrhenius Equation

The prevailing crosslinking simulation methodology does not attempt to account for relative reaction rates. The only existing attempts have been indirectly altering the collision frequency factor using the two-stage iteration approach (C. Li & Strachan, 2010) or manipulating the activation energy for the reactive force field (Vashisth et al., 2018). Here

a more robust quantitative approach for controlling relative reaction rates using the Arrhenius equation is offered:

$$k = Ae^{-\frac{E_A}{RT}}, \tag{2.1}$$

where k is the rate constant, A is the frequency factor, E_A is the activation energy, R is the universal gas constant, and T is the temperature. The rate constant is essentially the number of reactions that occur per second while the frequency factor is the number of properly oriented collisions per second. The quantity $e^{-E_A/(RT)}$ is the probability that any given collision will result in a chemical reaction. The frequency factor is inherently modeled in MD through the proximity-based approach. The definition of "collision" for large molecules is somewhat ambiguous, especially for non-gas phases. A properly oriented collision occurs when the reacting atoms fall within the sum of the van der Waals radii since it is the closest those atoms would get without the influence of their kinetic energy. Note that this is smaller than typical MD simulations and thus less likely to force undesirable high energy configurations. MD automatically considers several complex influences on the frequency factor including steric effects, the evolving concentrations of reactants, and the reciprocal effects of temperature causing both an increase in kinetic energy and a decrease in density. Manipulating the cutoff distance or using two-stage chemistry models (C. Li & Strachan, 2010) effectually modifies the frequency factor. It is generally assumed that activation energy does not change with temperature; the Arrhenius equation accounts for temperature dependence with the T in the exponent. The relative probabilities calculated from the exponential term of the Arrhenius equation are employed

as the probability terms for the crosslinking reactions. Therefore, all aspects of the rate constant are incorporated into curing simulations.

First, a metric is established to compare the results of crosslinking simulations under differing conditions. There is currently not a computationally efficient way to track the changes in the spread of molecular sizes, especially for tracking "infinite" periodic connections, so instead the structure was tracked through the ratio of amine constituents. Primary amine reactions attribute to the formation of chains while secondary amine reactions attribute to the formation of crosslinks; thus, the amine constituent ratio affects the M_C, which has been shown to influence material properties (Crawford & Lesser, 1999; Unger et al., 2019). Comparing results tracked against the step count is problematic for comparisons, so the normalized amine constituent percentage was tracked verses crosslinking degree. To demonstrate the validity of this metric, five crosslinking simulations were performed with unique random distribution seeds and compare the results at a probability of 0.001, as shown in Figure 2.2(a). The low standard deviation of these results indicates that despite the random initial configurations, the amine ratios are nearly identical at any given degree of conversion. Note that only a single random seed was used for the remainder of these crosslinking experiments to avoid the associated increase in computational costs.

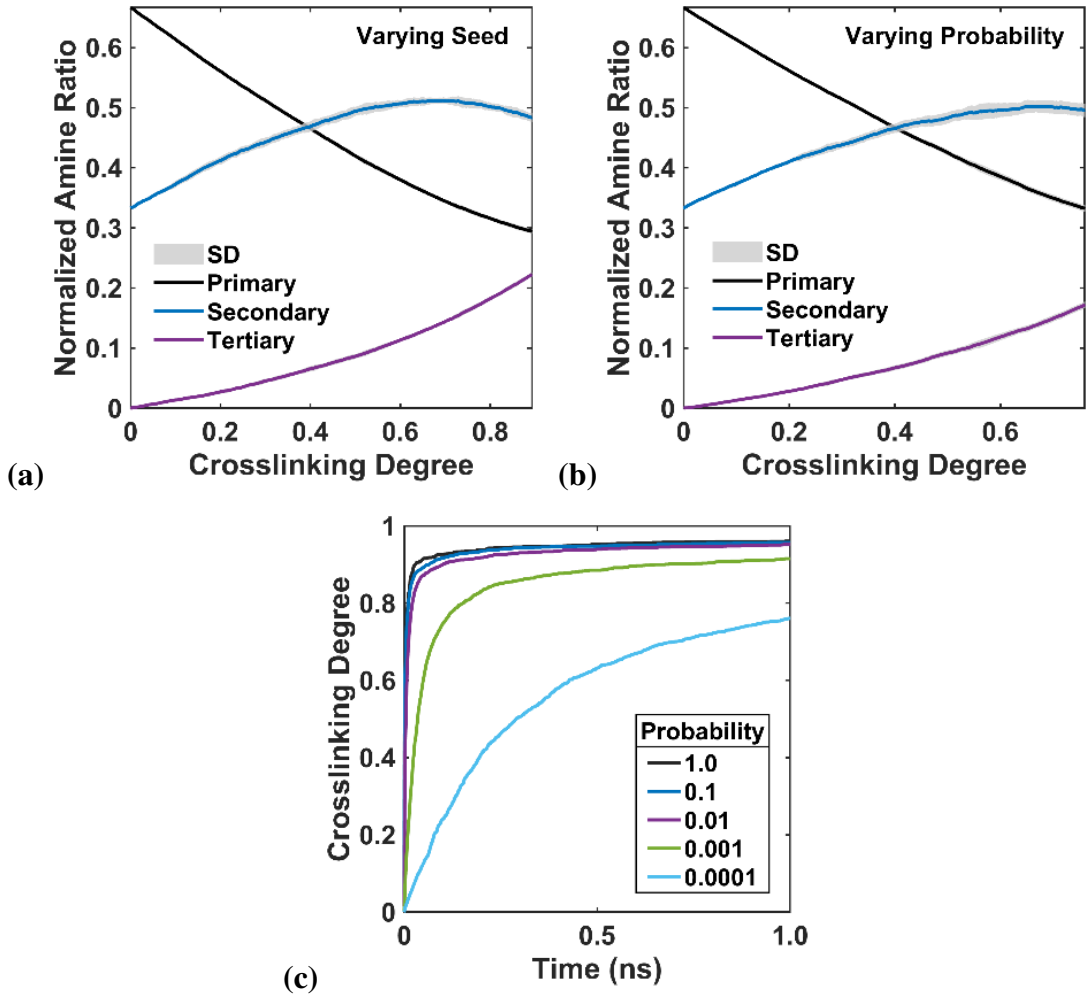

Figure 2.2. Normalized Amine Ratio Means and Sample Standard Deviations (SD) for (a) Five Randomly Seeded Samples With Reactions at 0.001 Probability and (b) Five Samples With Reaction Probabilities Ranging From 1.0 to 0.0001, and (c) Crosslinking vs. Step for Varying Reaction Probabilities.

In this next set of experiments, the dependence of the structure on the reaction probability was tested by comparing the normalized amine ratios of curing simulations performed with varying reaction probabilities. Figure 2.2(b) indicates that the probability has a negligible effect on the amine distribution at any given crosslinking degree for identical reaction probabilities. This is an advantageous result because it provides a physical justification for the usage of higher than realistic reaction probabilities to save

computation time. In contrast, Figure 2.2(c) shows the effect of probability on the rate of crosslinking. Lower probabilities require significantly more time to achieve the same degrees of conversion, which is why the max crosslinking in Figure 2.2(b) is only 76%.

The influence of higher reaction probabilities on the temperature at the onset of curing simulations was also analyzed. The temperature versus time plots for the first 1% of the crosslinking simulation for varying reaction probabilities are shown in Figure 2.3(a), illustrating the initial temperature spikes that occur for higher reaction probabilities. In order to further understand these temperature spikes, the atomic distribution of kinetic energy was analyzed at 600 timesteps – the location of the temperature peaks. The simulated probability density functions (PDFs) were plotted as a normalized histogram of the atomic kinetic energies with 160 bins, and the theoretical PDFs were calculated according to the Maxwell-Boltzmann energy distribution for the temperature at that timestep. The plots for the 1.0 and 0.001 reaction probability cases are shown in Figure 2.3(b). The 0.001 case closely matches the theoretical distribution, while the 1.0 case deviates significantly from its theoretical distribution. Though the average kinetic energy for the 1.0 case designates a higher temperature, the most probable kinetic energy appears unchanged. In addition, a distinctive spike is seen at $2.1 \cdot 10^{-22}$ J for the 1.0 case, which directly corresponds to the kinetic energy of a reacting hydrogen atom traveling at the maximum allowed speed. This spike is not observed for lower reaction probabilities. These observations indicate that the temperatures for the higher probability cases are initially changing in an unphysical manner. Although the temperature has been observed experimentally to increase during cure, these temperature changes do not accurately

represent this process, and the usage of a numerical thermostat prevents any longer-term temperature changes. Because these temperature deviations are highly transient, they have minimal impact on the final molecular structure as shown through Figure 2.2(b); nevertheless, it is likely that the standard deviations of the amine ratios for probabilities at or below the threshold of 0.001 would be further reduced with the more consistent temperature profile. Therefore, unless otherwise specified, subsequent simulations were performed at a probability of 0.001 to reduce initial temperature spikes and more accurately represent system dynamics.

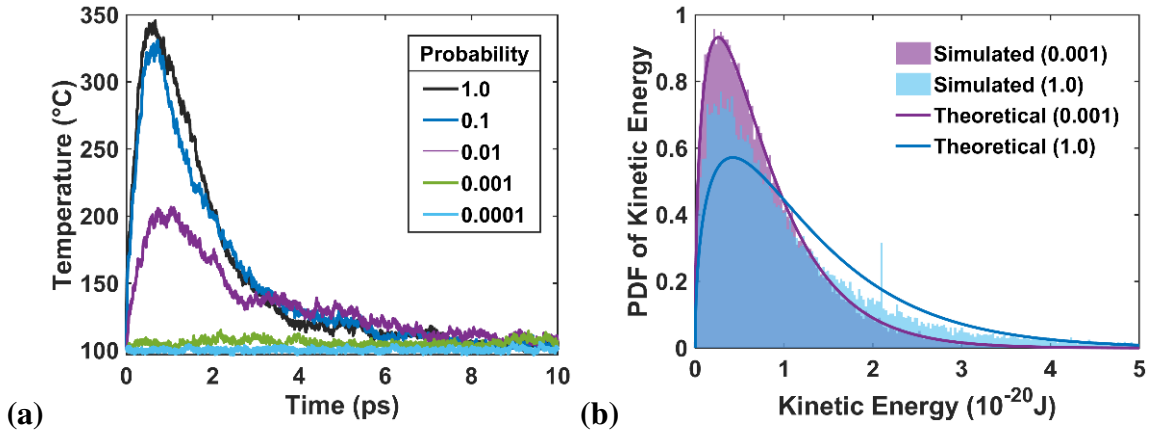

Figure 2.3. (a) Temperature vs. Time for the First 1% of the Curing Simulation With Varying Reaction Probabilities and (b) the Simulated and Theoretical PDFs Calculated at the Location of Temperature Peaks for the 1.0 and the 0.001 Probability Cases.

The amine reaction energies given by Chiao (Chiao, 1990) were used to demonstrate the incorporation of activation energy into curing simulations. Even though these reactions are for slightly different molecules, they still work to bolster the assertion that having unequal reaction probabilities impacts the network structure. Using these activation energies, the probabilities for reactions to occur on any given collision were calculated to

be $9.49 \cdot 10^{-11}$ for the secondary amine reaction and $1.95 \cdot 10^{-8}$ for the primary amine reaction at 100°C using the exponential term of the Arrhenius equation. As expected, these probabilities are far too low to be directly used in the crosslinking simulations, but as previously justified through Figure 2.2(b) a probability of 1.0 for primary amine reactions and 0.004869 for secondary amine reactions was used to accelerate curing simulations while maintaining their relative probabilities. Figure 2.4 shows that unlike the previous experiments, this does indeed have a major effect on the amine distribution. In addition, the individual effects of high cure temperature (800 K) and higher cutoff distance (4.5 Å) were tested, and the effects of these variables were isolated by comparing to a baseline simulation conducted with standard cure temperature (100°C), low cutoff distance (3.25 Å) and equal reaction probabilities. It is interesting to note that the high-temperature case reached 100% conversion while the higher cutoff distance case did not. Most resins at realistic temperatures do not achieve 100% conversion due to steric hinderances. Moreover, Figure 2.4 shows that temperature and cutoff distance also alter the amine distribution trajectories. This is an important distinction. While most MD crosslinking methodologies utilize high temperatures, high cutoff distances, and equal reaction probabilities, the results shown in Figure 2.4 reveal that these assumptions impact the final molecular structure. Though these details are not obvious enough to trigger detection, they are significant enough to affect results. Therefore, to generate an accurate thermoset system, it is necessary to account for the activation energies, use realistic curing temperatures, and employ a reasonable cutoff distance.

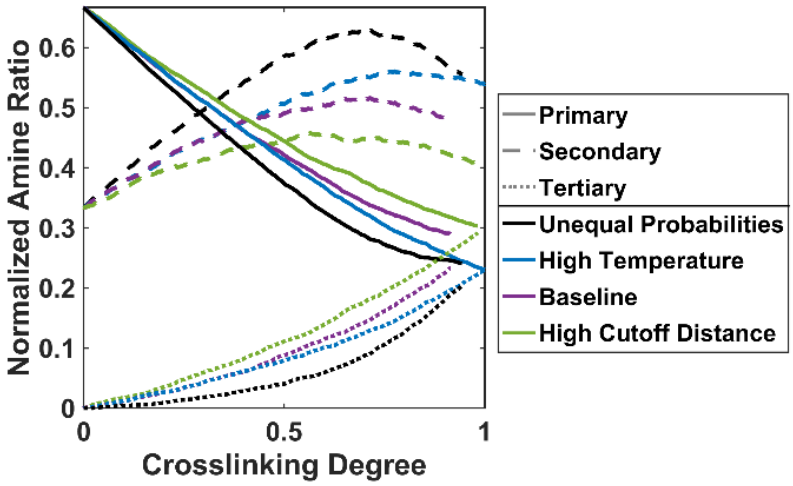

Figure 2.4. Normalized Amine Ratio vs. Crosslinking Degree Computed for Respective Simulations With a High Cure Temperature (800 K), High Cutoff Distance (4.5 Å), and Unequal Reaction Probabilities Compared to a Baseline Simulation Conducted With Standard Cure Temperature (100°C), Low Cutoff Distance (3.25 Å), and Equal Reaction Probabilities.

2.2.4. Assumptions of Diffusion

Another ubiquitous assumption inherent in molecular dynamic curing simulations is the assumption that the hardener molecules are randomly dispersed within the resin before the crosslinking simulations begin. This assumption is rationalized because the constituents thoroughly stirred. However, at the nanoscale, molecules are unlikely to be evenly distributed from macroscale mixing, so there will inevitably be resin-heavy and hardener-heavy regions. This could lead to a thermoset that, at the nanoscale, has regions with high crosslinking degrees and regions with low crosslinking degrees, which would have an impact on macroscale properties. Material failure stems from the weakest regions of the material, and the homogenous distribution of resin and hardener neglects the likelihood of weaker regions in macro materials resulting from unequal diffusion. This assumption is largely unaddressed in literature and is a difficult assumption to test because diffusion

occurs at a higher timescale and it is difficult to determine what an actual distribution would look like after mixing, but in an exploratory attempt to test the validity of the evenly dispersed assumption, two additional equilibrated RUCs were developed as shown in Figure 2.5. Two potential configurations are shown at this scale; one configuration has bands of resin and hardener (Figure 2.5(a)), while the second has spheres of hardener encased within resin molecules (Figure 2.5(b)). Note that the images in Figure 2.5(b) and Figure 2.5(d) have the resin molecules removed in the left half of the image so that the resin can be visualized. At room temperature, the molecular diffusion is too slow for nanosecond timescales, so the simulations are compared at 800 K, which essentially accelerates the diffusion. Preliminary tests of simulations at low temperatures appeared to form crosslinked barriers at the interfaces between hardener and resin but continuing those simulations at high temperatures did not seem to hinder further diffusion, suggesting that the molecular diffusion was just too slow to simulate at low temperatures. The results may not directly correlate with how the comparison would look at room temperature, but the accelerated diffusion and accelerated reaction rates should help to balance the two assumptions.

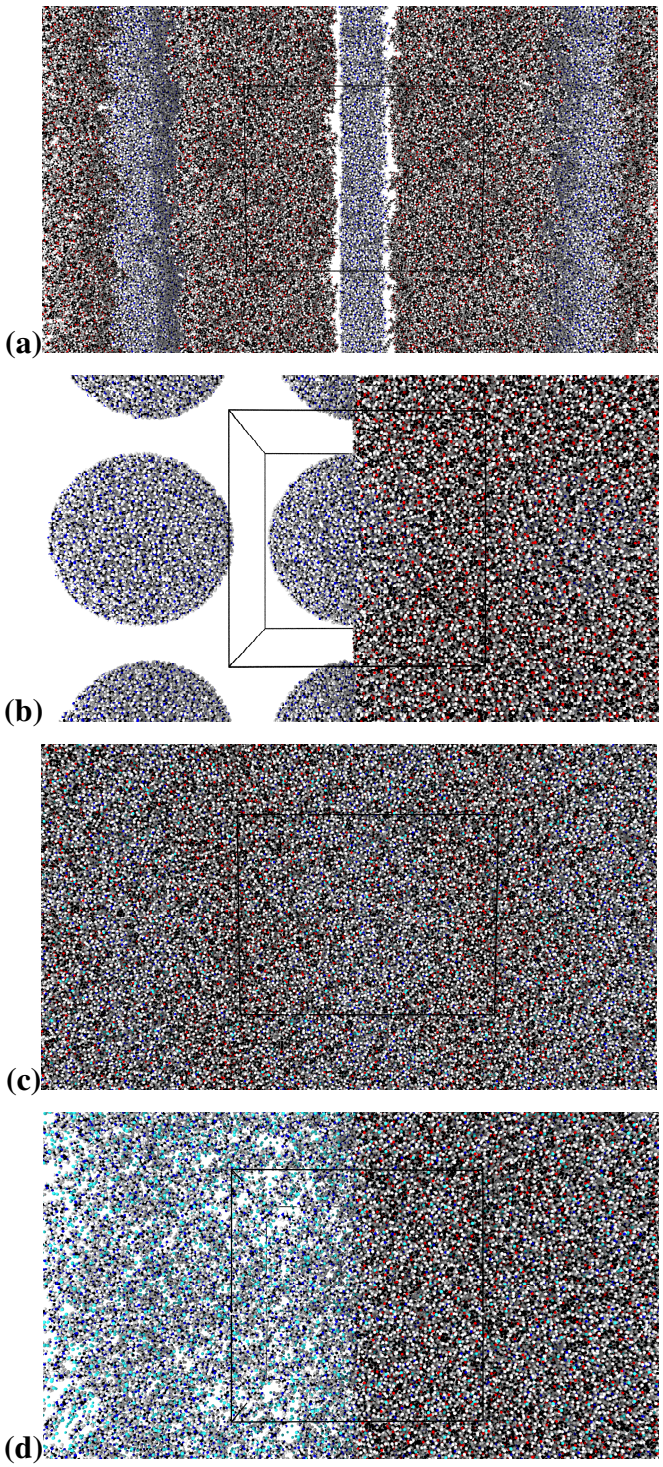

Figure 2.5. Boxed Repeating Unit Cells Shown Before (a),(b) and After (c),(d) the Diffusion/Reaction Simulation Steps for the (a),(c) Banded and (b),(d) Spherical Initial Equilibrium Conditions for the Hardener Molecules.

The post-cure images shown in Figure 2.5(c) and Figure 2.5(d) show that the crosslinks are evenly distributed despite the heterogeneous initial conditions, and the results are compared more quantitatively in Figure 2.6 by comparing the normalized amine ratios for each configuration, similar to the previous section. These results show that the banded and spherical initial configurations produce indistinguishable crosslink networks in terms of the amine ratios. They do vary slightly compared to the dispersed configuration but much less than the other assumptions such as temperature, cutoff distance, and dissimilar reaction probabilities as shown in Figure 2.4. This suggests that the assumption of randomly distributed constituents is reasonable.

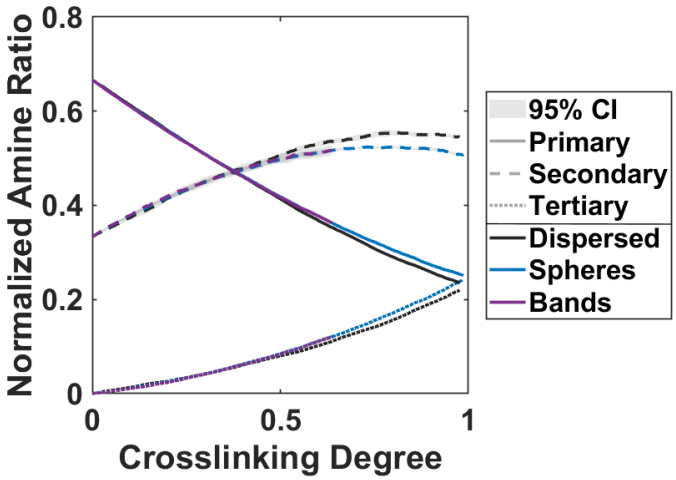

Figure 2.6. Normalized Amine Ratio vs. Crosslinking Degree for Molecular Dynamic Systems at 800 K Starting With Hardener Molecules Dispersed Collected in Nanospheres, and Separated Into Stripe Bands.

2.2.5. Density Considerations

Although using higher probabilities was shown to not alter the amine distribution, this assumption is not devoid of consequences. After crosslinking, the systems were

equilibrated using 1 ns of NPT simulation at test temperature, and the densities were observed to plateau, yet initial tensile testing simulations exhibited worse mechanical properties at low temperatures for high crosslinking degrees compared to low crosslinking degrees. Comparison of the densities between samples revealed that this was due to the considerably lower relative density, since stiffness is essentially governed by the strength and density of covalent bonds. Though the number of bonds is higher for higher degrees of crosslinking, with lower mass density, the bond density eventually decreases. The density was found to be higher for higher degrees of conversion for equilibration at high temperatures but reversed at low temperatures. A similar trend was observed by Bandyopadhyay et al. (Bandyopadhyay et al., 2011), but its adverse effects on mechanical properties were not mentioned. Because the higher-order bonding terms are completely defined in the systems in this study, the steric restrictions are more severe; other studies that neglect these terms and allow hinge-like molecular connections may not encounter this issue due to the unnatural flexibility of their systems. Thermosets with higher degrees of crosslinking do have greater dimensional stability, which can lead to lower densities at temperatures well below the cure temperature compared to thermosets with a lower degree of cure, so it is important to determine whether the large density disparity is an artificial consequence of the accelerated kinetics or merely a physical consequence of the dimensional stability.

To investigate this issue, the density evolution was examined during crosslinking simulations. Figure 2.7(a) shows the variation in density over crosslinking for varying probabilities at the standard cure temperature. These curves show three distinct events: first

the density increases suddenly due to the initial bond changes drawing molecules together; next, this rapid initial shrinkage generates high energy configurations causing the system to expand; finally, because the rate of crosslinking has slowed considerably, the network slowly contracts toward a metastable configuration. This observed density evolution is not physical, but rather is a consequence of the accelerated reaction kinetics caused by the usage of higher probabilities. To verify that this is the cause, another series of curing simulations were performed at 800 K, which, according to the Arrhenius equation, corresponds to a much higher average reaction probability of around 0.0001. Although this is obviously unphysical and would realistically enable competing degradation reactions, it is still valuable for comparison. Figure 2.7(b) shows that the results that differ considerably from that of the low-temperature curing. Since these simulations are much closer to the calculated reaction kinetics, the density increases in a nearly linear trend as the probability approaches 0.0001. This validates the interpretation of the Arrhenius equation, but also confirms the need for supplementary measures to correct the density for curing simulations at standard temperature with limited timescales.

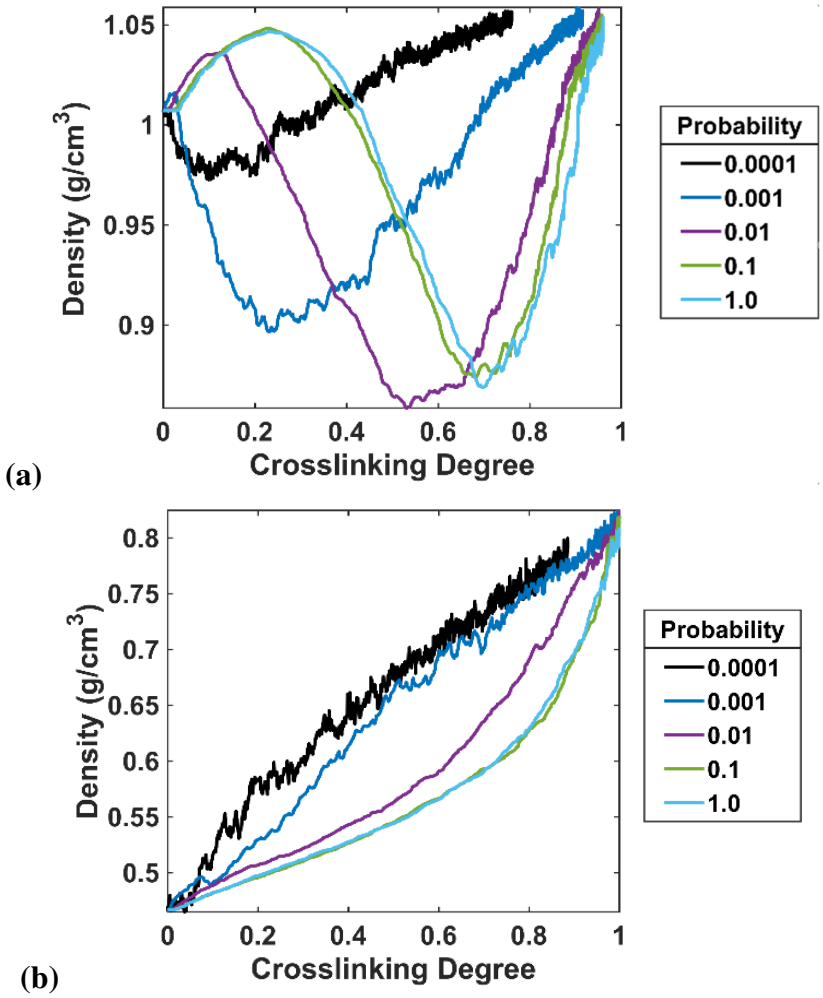

Figure 2.7. Density vs. Crosslinking for (a) Standard Curing Temperature (373 K) and (b) High Temperature (800 K) at Varying Reaction Probabilities.

While using high temperature for curing alters the amine ratios as shown in Section 2.2.3, using a high-temperature annealing period after crosslinking can increase the density without altering the amine ratios. High temperature gives systems energy to disrupt metastable configurations and find lower energy configurations closer to global minimums. Because most crosslinking simulations in literature are performed at elevated temperatures, they already require cooling simulations to bring the systems to testing temperatures, which is often doubled as a method for determining the T_g. Several studies recognize that high-

temperature curing reduces strain energy (C. Li, Medvedev, et al., 2012; C. Li & Strachan, 2010; Varshney et al., 2008), but this study emphasizes that it is actually the process of cooling from a high temperature that generates a more relaxed system; thus a post-cure annealing process is necessary to relax three-dimensional networks for curing performed at lower temperatures. Figure 2.8 shows the density profile as the temperature is heated to 1000 K and then slowly cooled back down to testing temperature for a variety of crosslinking degrees. The zoomed region highlights that the initial equilibrated densities are lower than the densities after the annealing simulation, especially for higher crosslinking degrees. This demonstrates that the thermal agitation successfully garnered lower density configurations even though the original densities had already plateaued with NPT equilibration. Accordingly, the potential energy was also observed to decrease. Figure 2.9 shows a sample 95% crosslinked cell with 1 nm sectional views before and after the annealing process. The nanovoids highlighted in Figure 2.9(b) exemplify the high potential energy regions maintained even after equilibration, while Figure 2.9(c) shows the section more relaxed after undergoing the annealing process. Higher cooling rates were found to be less effective, but the optimal anneal temperature and cooling rate was not investigated. A more thorough investigation may further shift systems toward global minimums and further improve accuracy at lower temperatures. In summary, the curing itself should not be done at high temperature because that affects the amine constituent ratios, but a post-crosslinking, high-temperature anneal is necessary to force the system out of metastability and produce a more relaxed polymer network, especially for testing at lower temperatures. This is not representative of a physical process but rather a numerical

tool to produce results that emulate the results that would be achieved with time frames beyond current computational limits.

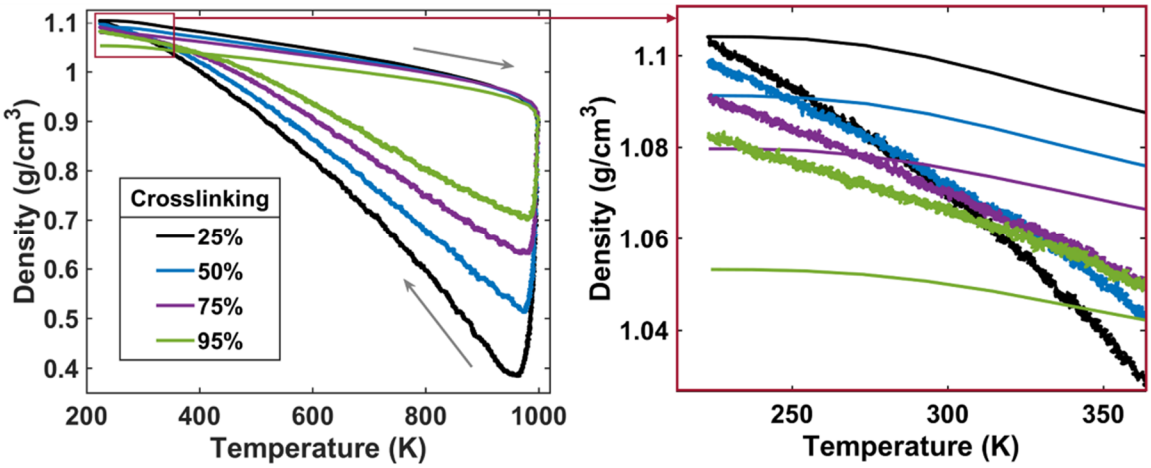

Figure 2.8. Density vs. Temperature During the Post-Cure High-Temperature Annealing Simulations.

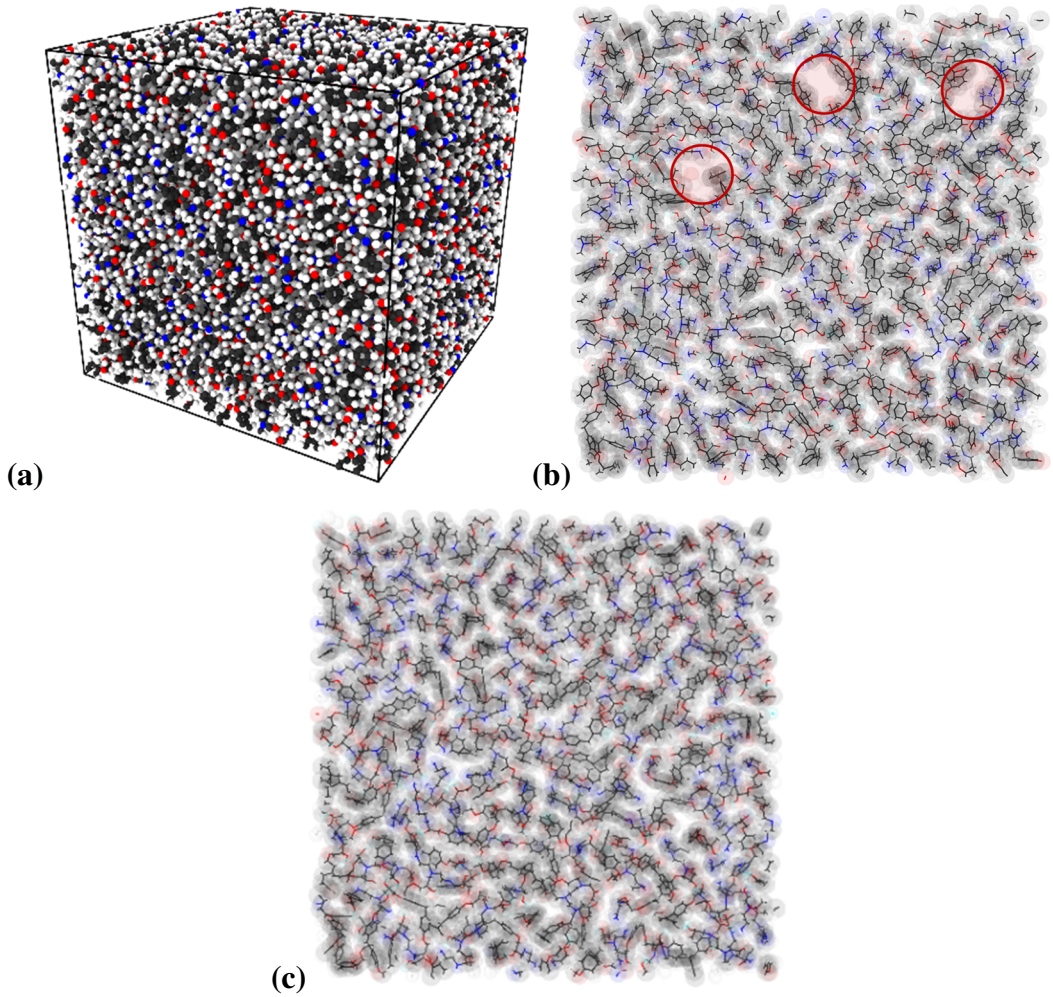

Figure 2.9. (a) A Sample 95% Crosslinked Representative Unit Cell (RUC) at 0°C With 1 nm Sectional Views (b) Before and (c) After the Annealing Process.

2.3. Thermomechanical Response

Of the three main MD methods for determining material properties, the dynamic test, which relates most closely to the experimental process, was shown to have the best accuracy (C. Li & Strachan, 2015). Therefore, using the developed methodology, uniaxial tensile tests for 25, 50, 75, and 95% crosslinked systems were conducted at temperatures of interest ranging from -50 to 250°C to analyze their ability to simulate the effects of

temperature and crosslinking degree on strength, stiffness, and the Poisson's ratio. In this study, thermal degradation mechanisms were limited to property variation due to increased thermal molecular vibrations; mass volatilization is another viable aspect of thermal degradation, but this was not considered.

2.3.1. Tensile Testing Method

Once the systems were equilibrated at the testing temperatures, tensile deformation was applied to the simulation box at a constant engineering strain rate of 10^9 s^{-1}, a standard strain rate for MD, which corresponds to a deformation velocity well below the atomic thermal vibration frequencies. Box deformation was used because it involves less manipulation compared to affine transformation and group deformation, although these differences were not observed to be significant. A constant engineering strain rate was used to emulate constant displacement rate tensile tests, while also eliminating acceleration of strain at higher strains, since the discrepancy between engineering and true strains becomes increasingly prevalent at higher strains. The NPT ensemble was employed at the desired temperatures, and atmospheric pressure was applied in the off-loading directions. To reduce sampling errors, five distinct representative unit cells (RUCs) were randomly generated with unique seed numbers for each case. In addition, ergodic assumptions were applied such that the arithmetic means and sample standard deviations were calculated over 1000 timesteps. This allows for a better interpretation of the pressure-related terms, which otherwise fluctuate substantially on MD length scales. The ergodic averaging and high data

resolution combined with averaging over multiple systems together enable the results to be sufficiently smooth such that no extraneous smoothing algorithms are required.

It should be noted that these experiments were not performed to failure. The classical molecular force fields used do not allow bond breakage, so further straining causes the epoxy to disentangle rather than fracture. When testing reactive force fields, only around 0.1% of bonds broke, even for complete material scission, which occurred past 100% strain. Therefore, neglecting bond breakage is a reasonable assumption to make when studying system response at pre-failure strains. Classical force fields are intended to represent the system in near equilibrium positions, so excessive deformations are outside their intended use; thus, simulations were limited to 40% strain. Reactive force fields could easily be implemented after the curing simulations, but they generally require system-specific parameterization, which is beyond the scope of this work. The basic Reax Force Field (ReaxFF) was found to yield higher stresses, similar to those reported by Odegard (Odegard et al., 2014), and require significant computational expense.

2.3.2. Thermomechanical Results

Conventional MD studies on the thermomechanical properties of thermosets evaluate the T_g by identifying the kink in the bilinear regression of the density versus temperature plot; therefore to provide standard T_g plots for 25, 50, 75, and 95% crosslinked systems, the density trajectories retained from the annealing simulations are shown in Figure 2.10 with estimated bilinear regressions. As expected, the intersections indicate increasing dimensional stability and T_g with increasing crosslinking degree. Though the precise T_g

values are sensitive to the points chosen for the linear regression and may vary depending on the cooling rate, the qualitative trend should remain. This study goes beyond this typical analysis to directly relate the T_g to its impact on the mechanical properties; the characteristic sigmoidal trends associated with T_g-dependent properties have been computed for the strength, stiffness, and Poisson's ratio and compared for the varying degrees of cure, complementing the typical density-based T_g calculations.

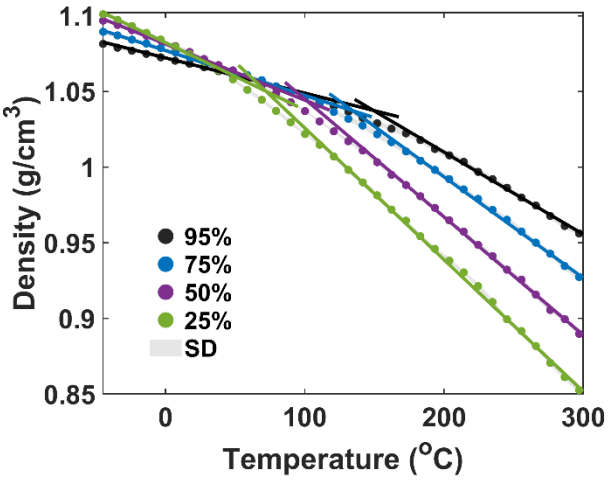

Figure 2.10. Density vs. Temperature for Systems With 25, 50, 75, and 95% Crosslinking. Bilinear Fits are Shown to Visualize the Shifting T_g.

2.3.2.1. Strength

The virial stresses of each atom were averaged at each timestep to obtain the spatially averaged stress. Although the bulk velocity of the system is ideally null, care was taken to remove the bulk atomic mean velocity from the kinetic part of the virial stress calculation to better represent the continuum level stresses as detailed by Subramaniyan et al. (Subramaniyan & Sun, 2008). These measures enable the simulation stresses to approach the continuum Cauchy stress, though the stresses and strains in the RUC should not be

directly compared to macroscopic stresses and strains from tensile testing due to MD time and length scale incompatibilities. The high strain rates result in increased strength, especially for polymers due to their viscoelastic response (Fu et al., 2017), and the high strains to failure in MD simulations are attributed to the small sample sizes, which preclude strain localization (C. Li & Strachan, 2010, 2011).

The stress-strain curves for 25 and 75% crosslinking across a range of temperatures are shown in Figure 2.11. The harmonic potentials of the classical force field do not emulate bond breakage; however, the simulations are seen to capture nonlinear plastic deformation in the form of chain sliding and reorientation, enabling relative strength estimation. The results of Figure 2.11 demonstrate that the strength is increased for higher degrees of crosslinking, and the strength of the material degrades with increasing temperature, which aligns with experimental studies. This also makes intuitive sense when considering the behavior of the molecular system as the temperature increases; higher temperatures stimulate increased molecular vibration, which increases the likelihood of the system encountering configurations with lower potential energy, thereby relaxing some of the stress. For the systems with 25% crosslinking, the stress fluctuates close to zero at higher temperatures, indicative of a viscous liquid state; however, systems with higher degrees of conversion still maintain stress at high temperatures. This is expected for fully cured thermosets since the crosslinks preclude the possibility of a liquid state. In addition, after the initial elastic response, the systems exhibit slight softening behavior at lower crosslinking degrees and strain hardening at higher crosslinking degrees. The systems with lower crosslinking degrees soften because the molecules can reorient to absorb

displacement energy. In contrast, the low flexibility of highly crosslinked systems only permits limited reorientation and sliding for stress absorption, causing the stress to continue to increase with increasing strain.

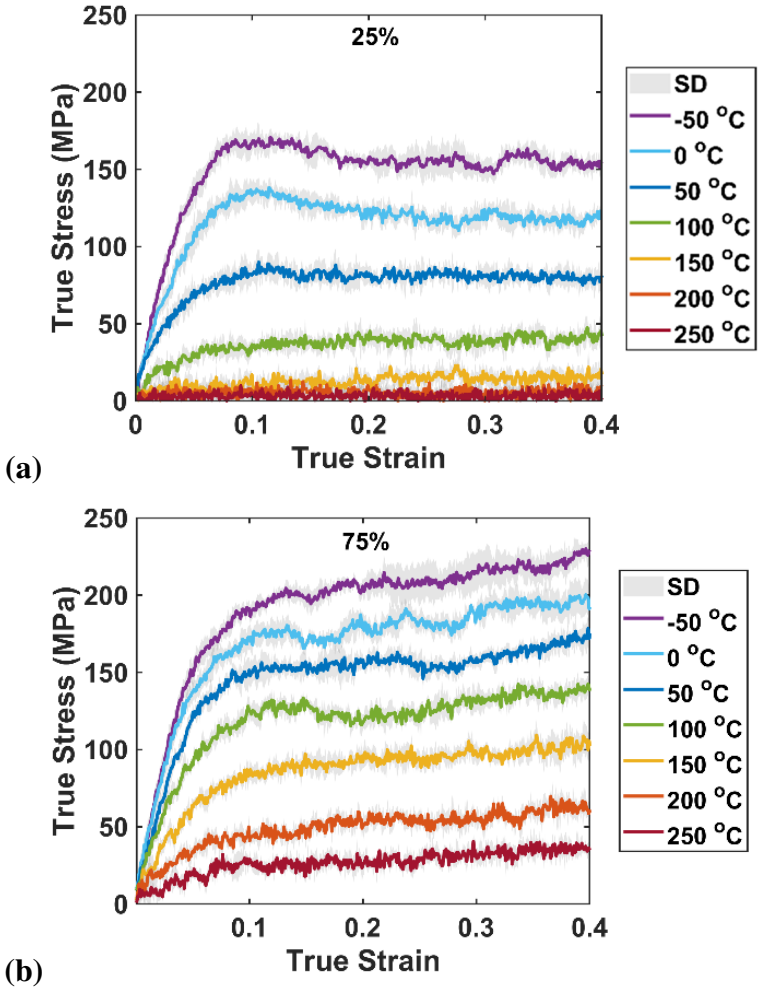

Figure 2.11. Stress-Strain Means and Standard Deviations (SD) for Systems With (a) 25% and (b) 75% Crosslinking Over a Range of Temperatures From -50 to 250°C.

To compare the results for a large number of systems simultaneously, the stress for various systems at 20% strain was calculated to represent relative material strength in the regions where the slopes have diminished appreciably. Note that these values are not meant

to be taken as the ultimate or yield strengths, but rather a metric for consistent comparison of the strengths between the various systems. The strengths are plotted against temperature for systems with 25, 50, 75, and 95% degrees of crosslinking in Figure 2.12. These results show the tail-end of sigmoidal behavior typical of properties altered by the T_g. The rightward shift of the curves with increasing degree of cure represents the shift in T_g; the systems with higher crosslink densities have higher T_g points.

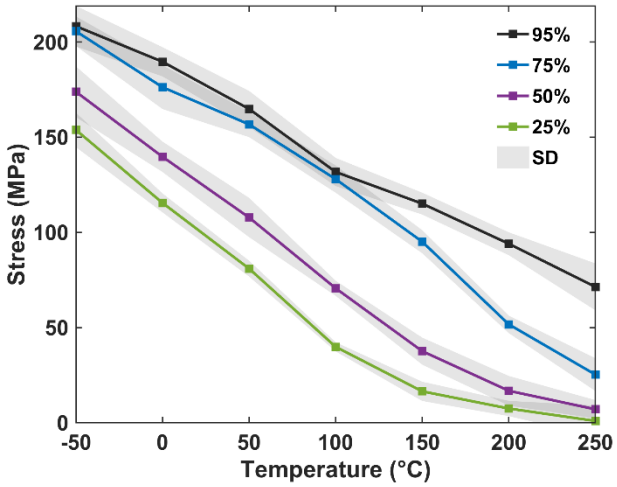

Figure 2.12. Material Strength Means and Standard Deviations (SD) at 20% Strain for Systems With 25, 50, 75, and 95% Crosslinking Across a Range of Temperatures From -50 to 250°C.

2.3.2.2. Stiffness

The Young's modulus at each temperature was computed by finding the slope of the linear regression of the initial portion of the stress-strain curve and averaging over all the randomly seeded systems. Something that should perhaps be more transparent in MD is the sensitivity of these calculations to the averaging region, so the Young's modulus and its standard deviation is shown by averaging up to each point of strain up to 10% strain.

This is not meant depict the evolution of stiffness with strain, but merely to show the sensitivity of Young's modulus to the averaging cutoff point. These plots are shown for 25 and 75% crosslinking at varying temperatures in Figure 2.13, which successfully demonstrate stiffness degradation with increasing temperature. These results show significant instability for the Young's Moduli calculated below 2% based on both the mean values and larger standard deviations. Then the calculated stiffness decreases with increasing strains due to the nonlinear behavior. In response to these results, stiffness is calculated by averaging the stresses up to 2% strain, but these exact values should be regarded cautiously because of the unsteady nature of the stiffness calculations as illustrated in Figure 2.13. In the future it may be desirable to consider extrapolating the stable results for 2% strain onwards back to 0% strain to achieve a slightly higher, more accurate result. Neglecting to consider this and averaging over longer periods may contribute to the reason stiffness values recorded in MD are often conveniently close to experimental values.

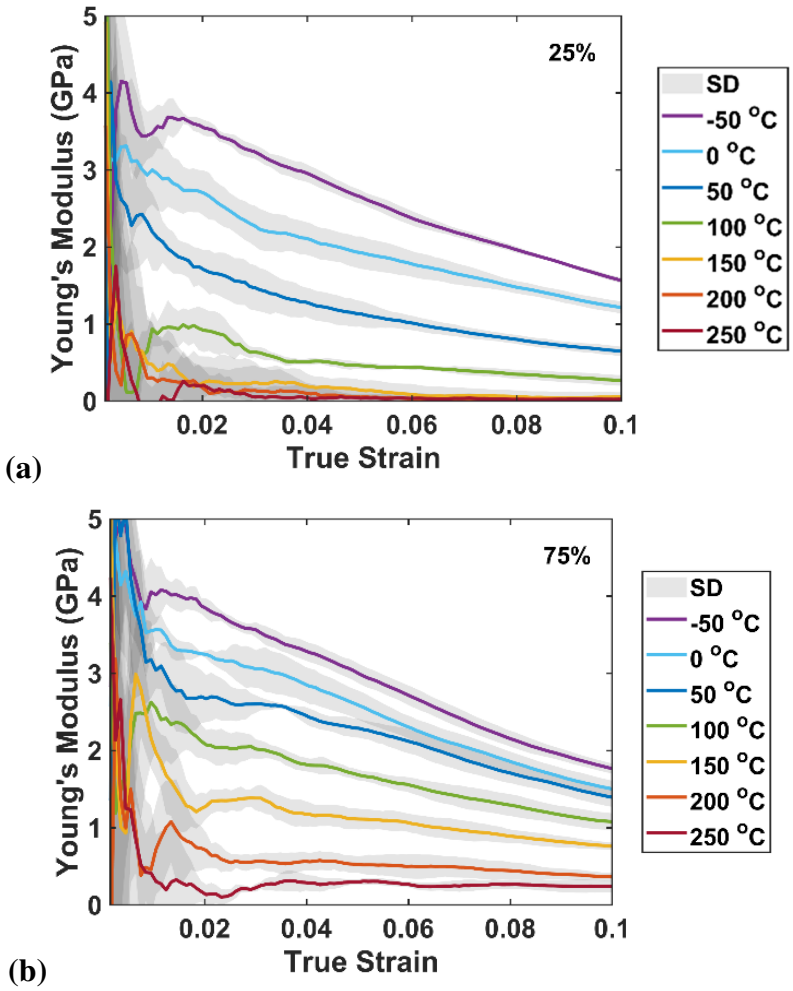

Figure 2.13. Sensitivity Analysis: Means and Sample Standard Deviations (SD) of Stiffness for Systems With (a) 25% and (b) 75% Crosslinking as Calculated by Averaging up to Each Point of Strain for a Range of Temperatures From -50 to 250°C.

To compare the Young's moduli for varying temperatures and crosslinking degrees simultaneously, the stiffness was calculated using strains up to 2% and plotted the values against temperature for each set of crosslinked systems as given in Figure 2.14. Similar to the strength results, these results adhere to the sigmoidal trend shifted by the T_g. The Young's Modulus would continue to level off for higher temperatures and should increase at a slower rate for lower temperatures, but these temperatures are outside of the range of

interest, so they were not explored. The stiffness of the 95% crosslinked case is seen here to be lower than the other cases, but this is likely due to the failure of the crosslinking to find a high density, low energy configuration for such a high degree of crosslinking. As discussed in Section 2.2.5, further refinement of the post-crosslinking anneal process should further improve the system structure for cases of extremely low temperature and high crosslinking. Because stiffness depends on the immediate system response, it is more sensitive to this initial state than the strength.

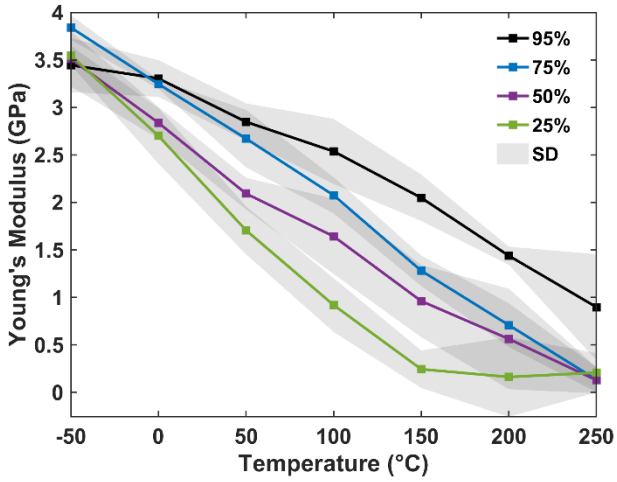

Figure 2.14. Young's Modulus Means and Sample Standard Deviations (SD) Calculated up to 2% Strain for Systems at 25, 50, 75, and 95% Crosslinking Across a Range of Temperatures From -50 to 250°C.

2.3.2.3 Poisson's Ratio

The Poisson's ratio is important to analyze because it is directly related to the rate of density changes, and its changes provide information on the state of the material. Furthermore, in combination with the Young's Modulus, the Poisson's ratio enables the complete definition of the elastic properties under the assumption of isotropy using a single

computational experiment. The Poisson's ratio was calculated according to the differential definition using the average of the off-axis strains divided by the applied strain. In this paper, the calculated Poisson's ratio will be referred to as the apparent Poisson's ratio to emphasize that they are defined by the total strains up to that point rather than the instantaneous Poisson's ratio defined by the strain differentials over each timestep. Because this definition of the Poisson's ratio is hysteretic, it does introduce some lag in depicting changes; however, the values are far more stable than the instantaneous definitions, and they emulate the experimental measurements of Poisson's ratio. The calculations for the apparent Poisson's ratio at 25 and 75% crosslinking are plotted in Figure 2.15. These results show that the Poisson's ratio generally increases with increasing temperature, corresponding to increased molecular mobility, which gives the system more flexibility to conserve volume. In the 25% crosslinking case the Poisson's ratio increases toward 0.5, which corresponds to a volume conserving deformation, indicative of liquid flow. In the 75% crosslinked case, this effect is much more prominent at temperatures above 100°C indicating that this phenomenon is activated at the T_g. In addition, the Poisson's ratio is seen to increase as the simulation progresses, revealing the onset of plastic flow. A Poisson's ratio of 0.5 corresponds to constant volume deformation, which in general suggests plastic deformation. So, monitoring the increase of the Poisson's ratio with deformation effectively monitors plastic response. Furthermore, for simulations run to higher strains, the Poisson's ratio subsequently decreased, revealing the onset of damage, a precursor to failure.

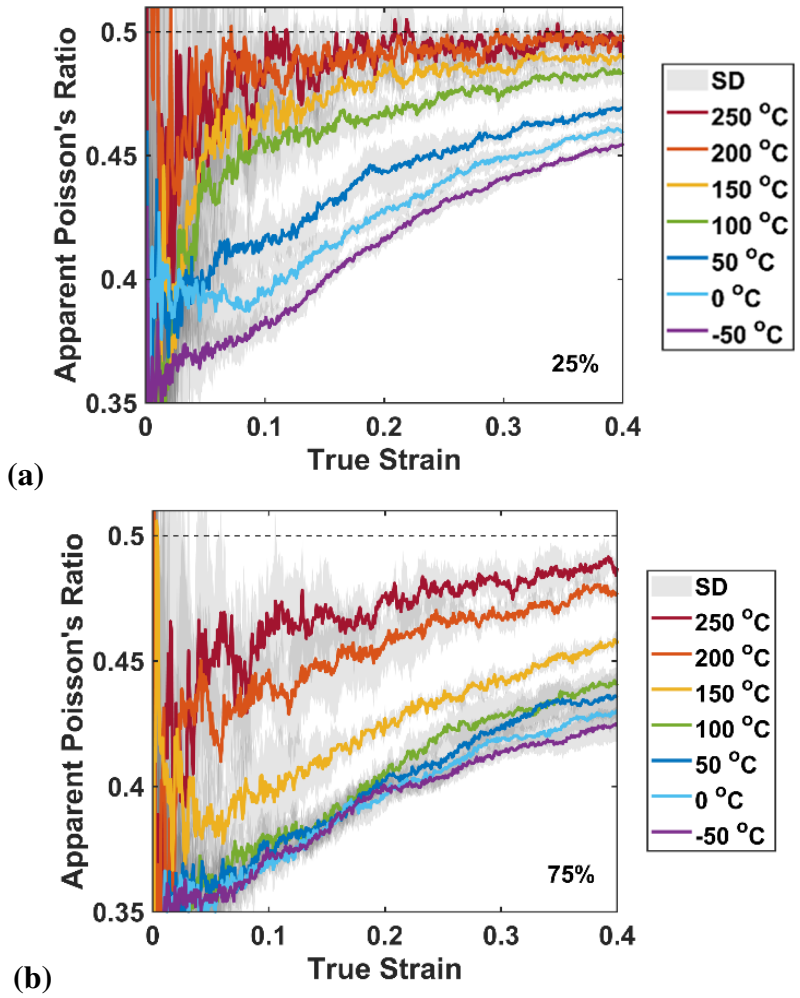

Figure 2.15. Apparent Poisson's Ratio Means and Sample Standard Deviations (SD) for 25 and 75% Crosslinking for Systems With (a) 25% and (b) 75% Crosslinking for a Range of Temperatures From -50 to 250°C.

In parallel with the results for strength and stiffness, the apparent Poisson's ratio was identified for systems of varying crosslinking degrees to plot simultaneously across a range of temperatures. The apparent Poisson's ratio was taken at 10% strain since this is past the initial instability but before the Poisson's ratio has increased substantially. These calculations are plotted in Figure 2.16 using a reversed y-axis to highlight the correlation to the other properties in the sigmoidal trend expected for properties influenced by the T_g.

Again, the up-rightward shift of the curves with increasing degree of cure represents the shift in T_g; the systems with higher crosslink densities have higher T_g points.

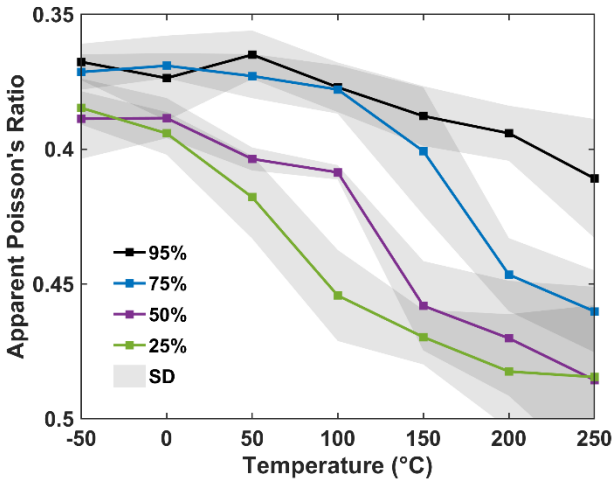

Figure 2.16. Apparent Poisson's Ratio Means and Sample Standard Deviations (SD) Calculated at 10% Strain for Systems at 25, 50, 75, and 95% Crosslinking Across a Range of Temperatures From -50 to 250°C.

2.4. Summary

In this chapter, a significantly improved methodology for modeling the crosslinking of thermoset polymers using a dynamic, proximity-based MD reaction algorithm was established and tested, and the physics-based integration of activation energy information directly into these crosslinking simulations was formulated. The effects of various crosslinking conditions on the resultant molecular structure were demonstrated through the apportion of the different amine types, underlining the consequences of some commonly used MD crosslinking assumptions. This information can be used to correlate MD structures to experimental structures using near-infrared (NIR) spectroscopy, as done by Unger et al. (Unger et al., 2019). In addition, the role of high temperature in system

relaxation was elucidated, and through the analysis of density evolution and reaction kinetics, the need for a slow-cool, post-cure, high-temperature annealing process to amend molecular systems was illustrated, especially for high conversion degrees and low temperature testing.

To analyze the effects of temperature and crosslinking degree on strength, stiffness, and the Poisson's ratio, a variety of systems generated with this methodology were subjected to uniaxial tensile testing. The strength and stiffness were shown to degrade with increasing temperature while the Poisson's ratio was shown to increase. The sensitivity of stiffness calculations to the averaging regions was demonstrated, and changes in the Poisson's ratio were linked to different states of the deformation process. Furthermore, the characteristic sigmoidal trend associated with T_g-dependent properties was observed for each of these mechanical properties. The shift in these curves was observed for different crosslinking degrees, indicating the T_g disparity. This provides a unique look at T_g variation between different systems through its impact on the mechanical properties, complementing the typical density-based calculations. Therefore, the effectiveness of the crosslinking method in generating MD thermoset polymer networks was demonstrated. The robust curing methodology works for any reactants and accommodates any classical forcefields; so in the future, new thermoset materials can be accurately modeled if activation energy and force field parameters can be determined via ab initio methods, thereby reducing the need for trial-and-error fabrication and experimental testing, and greatly expediating the material development process.

CHAPTER 3.

ATOMISTIC STUDY OF DAMAGE IN THERMOSETS*

3.1. Introduction

The proximity-based MD curing methodology developed in the previous chapter is used to explore the evolution of the state of a material under uniaxial loading with an emphasis on the correlation to changes in stiffness. The simulations were conducted for a thermoset polymer to demonstrate the ability of MD to model damage in a complex material, but the presented damage analysis methodology should work equally well for other materials. Property changes were related to explicit changes in stiffness through a set of carefully orchestrated uniaxial tensile loading, unloading, and reloading experiments for multiple samples. The combined effects of damage and anisotropic changes in stiffness associated with molecular bond alignment were successfully captured and related to the state of deformation, and the results for both reactive and classical forcefields were compared to investigate the role of bond breakage in the progression of damage in crosslinked polymers. The void fraction is quantified, revealing sudden initiation points and consistent growth rates, which are correlated to averaged changes in stiffness, and the state of deformation. In addition, the misleading portrayal of results employing Lagrangian or partially Lagrangian stress-strain pairs for these high molecular strains is elucidated, and the benefits of using differential property definitions as opposed to the cumulative average

* This chapter is based on the author's previously published journal article (Schichtel & Chattopadhyay, 2020).

values are illustrated. However, due to the prohibitive variation caused by the highly localized nature of damage, the limitations of using MD simulations to define damage initiation for multiscale models must be addressed.

3.2. Molecular Model

3.2.1. System Definition

The framework detailed in Chapter 2 was used to generate six cured epoxy periodic RUCs, each from a random distribution of 1000 DGEBF resin and 817 DETA hardener molecules, maintaining the experimental 100:27 weight ratio for DGEBF to DETA (Sun et al., 2008). The epoxy was cured at 100°C to a crosslinking degree of 80%, as defined by the number of epoxide groups, annealed at 600 K to relax the structure, and finally slow cooled to an equilibrated temperature of 20°C. The resultant thermoset epoxy is a common matrix material for composites (Domun et al., 2015). These 59340-atom systems are moderately large for all-atom MD thermoset models, which helps to reduce noise and size-dependence (C. Li & Strachan, 2015).

All MD simulations were implemented using LAMMPS software (Plimpton, 1997). The classical Merck Molecular Force Field (MMFF), complete with bond, angle, and improper terms obtained from SwissParam, was employed for curing and classical testing (Zoete et al., 2011). Lennard Jones force switching functions were used for pairwise interactions with a cutoff of 10 Å, and the PPPM method was used for long-range coulombic interactions in K-space. This classical force field has been previously shown to

yield accurate results for these constituents (Koo et al., 2014). In order to compare results for force fields with and without the potential for bond breakage, the equilibrated systems were copied and converted to ReaxFF, a reactive force field specially parameterized for hydrocarbons (Van Duin et al., 2001). The parameter set used (Singh et al., 2013) has been previously validated according to the bond strengths of various parameter sets (Subramanian et al., 2017). The conversion required an initial minimization period followed by 50000 timesteps of equilibration to allow the system to adjust and the density to re-equilibrate. One fs timesteps were used for the classical forcefield while smaller timesteps of 0.5 fs were needed for the bond order force field.

3.2.2. Test Method

The uniaxial tension tests were conducted by applying a constant engineering strain rate to the simulation box. A constant engineering strain rate was employed using a prescribed box deformation velocity to emulate constant displacement rate tensile tests. A strain rate of 10^8 s^{-1} was used for the classical force field while a strain rate of 10^{10} s^{-1} was used for the reactive force field. The relatively low strain rate was used for the classical cases to provide more data points to use for ergodic averaging enabling smoother, more precise results, in addition to being closer to macroscale strain rates. The higher strain rate was used for the reactive forcefield to negotiate the high computational expense inherent in bond order force fields. The velocities caused by these moderate strain rates are far lower than the velocities induced by the thermal vibration frequency; even at 10^{10} the root mean square velocity of the slowest atom (oxygen) is an order of magnitude higher than the

extension velocity. The NPT ensemble was utilized with atmospheric pressure applied only in the off-loading directions to emulate standard conditions. Nose-Hoover thermostats and barostats were used to control the temperature and pressure with standard damping coefficients and 0.5 drag. The tensile loading was performed to 250% extension, at which point considerable damage was seen to have accumulated, amounting to 25 million and 250 thousand timesteps for classical and reactive force fields, respectively.

It is impossible to perform both unloading and continued loading experiments from a single material state on a physical specimen. This highlights another advantage of MD over traditional experimental testing: the timeline of a single specimen can be split; any number of distinct loading paths can be performed on the exact same RUC. To determine the precise Young's modulus at several points along the uniaxial stress-strain curves, complete snapshots of the state of the system were saved at various strain increments, and unloading and reloading experiments were subsequently performed from those snapshots. Thus, the Young's modulus of the material at the original point along the stress-strain curve is the stiffness calculated from the reload test. The unloading experiments were implemented with displacement-controlled unloading, which was terminated when the average stress over a range of timesteps fell below zero. The unloading was followed by a brief equilibration period, although this step is largely unnecessary since the stress was brought to zero gradually. Ergodic assumptions were utilized; the mean values were calculated over 10000 timesteps for the classical systems and 100 timesteps for the bond order systems, unless otherwise specified. This averaging is necessary for an accurate interpretation of the pressure-related terms, which otherwise fluctuate substantially in MD length scales.

Furthermore, the sampling errors were reduced by averaging over the six RUCs. These techniques enable the results to be sufficiently smooth such that no extraneous smoothing algorithms were required. The multitude of simulations performed were collectively computationally intensive, with an overall cost of close to one million CPU hours.

3.3. Results and Discussion

3.3.1. Comparison of Finite Deformation Stress-Strain Measures

The time and length scale restrictions inherent in MD simulation inevitably lead to significantly higher stresses and strains compared to macroscale experiments. The high strain rates necessary in MD simulations heighten stress values, and this effect is augmented for polymers due to their viscoelastic behavior (Fu et al., 2017). The high strains in MD simulations are linked to their inability to localize strain due to the small sample sizes (C. Li & Strachan, 2010, 2011; Meng et al., 2016). Even though thermosets are macroscopically homogeneous, they exhibit heterogeneity at the nanoscale, which causes strain to localize in regions with the highest stress concentrations. Therefore, even though thermosets typically exhibit brittle behavior in macroscale, they undergo large plastic deformation in the vicinity of failure. For MD studies focusing on the elastic regime, the choice of stress and strain measures is fairly inconsequential, but for studies extending into to the plastic and failure regimes, it is necessary to choose an appropriate finite strain measure. This is especially important in the current study because elastic unloading and reloading simulations are conducted at high strains, and an arbitrary choice can lead to

misleading interpretations of the data, particularly for stiffness measurements from unloading-reloading experiments.

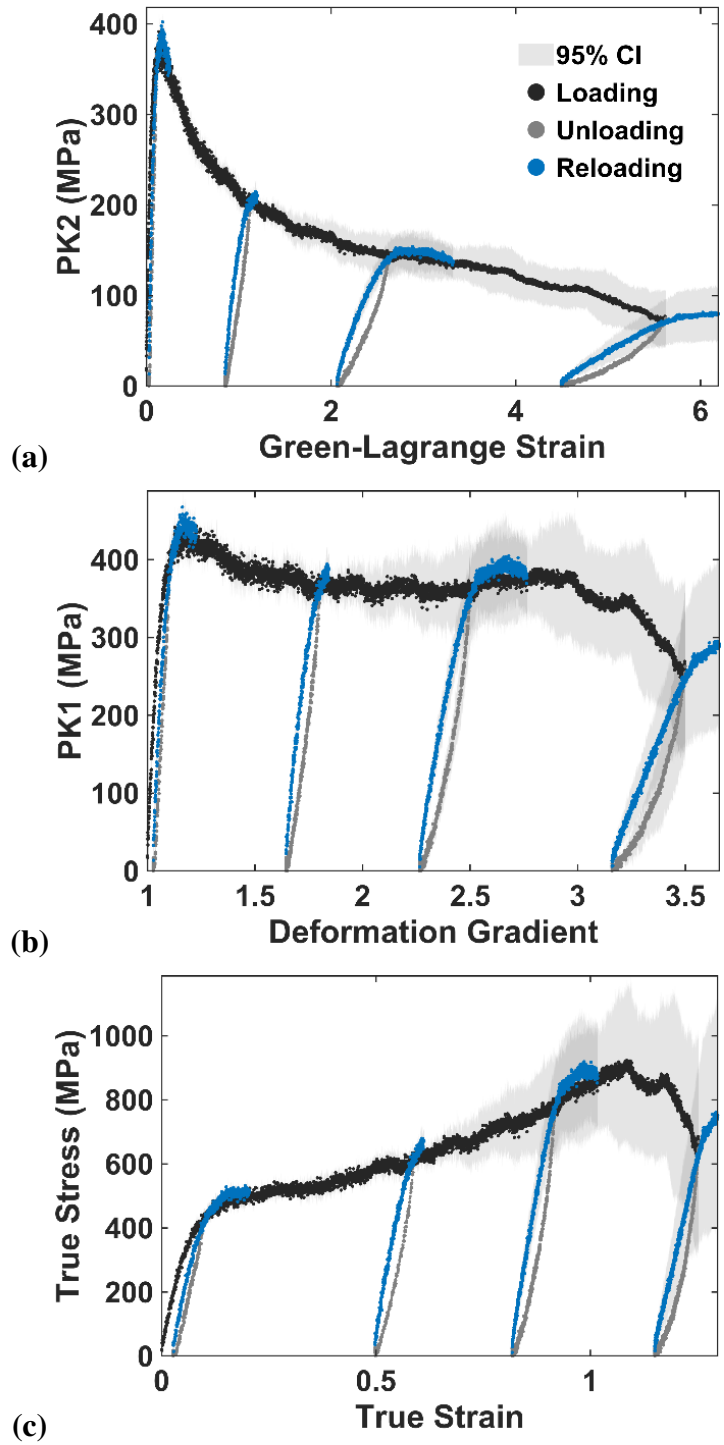

Figure 3.1. Uniaxial Tensile Loading Results for Molecular Dynamics (MD) Reactive Force Field Simulations Expressed via Conjugate Stress-Strain Relationships in (a) the Lagrangian Frame, (b) the Mixed Eulerian-Lagrangian Frame, and (c) the Fully Eulerian Frame.

The comparison of the stress-strain results for the reactive force field MD simulations are shown Figure 3.1 using three large deformation theory energy-conjugate stress-strain pairs: deformation gradient (F) – first Piola-Kirchhoff stress $(PK1)$, Green-Lagrange strain (E) – second Piola-Kirchhoff stress $(PK2)$, Hencky/logarithmic/true strain (ε_{True}) – Cauchy true stress (σ). The confidence interval (CI) for each segment is calculated using the sample standard deviation of the six samples. The CI for the unloading simulations is not shown because it required averaging in both dimensions. Since the material is in the principal axes, the 1-1 component of F is equal to the stretch ratio (λ), which is commonly used for large deformation analysis of rubber-like materials (Karimi et al., 2015). Though F is not technically a strain, it is identical to the engineering or the Biot strains scaled by one with these uniaxial loading conditions. In general, the true stress is not work conjugate to the true strain, but under the special case of uniaxial stress they are conjugate. The energy and power densities for each of the three pairs shown were calculated and found to be identical, but the plots show drastically different interpretations of the same data set. The unloading and reloading trajectories for the $PK1{:}\,F$ and $PK2{:}\,E$ relationships seem to suggest substantial stiffness degradation as the experiments progress; however, this is merely an artifact of the frames of reference. Because these two stress-strain relationships relate partially and fully to the reference configuration, respectively, the large geometrical changes distort the appearance of behavioral changes at high strains. Therefore, it is imperative to use purely spatial frames when trying to isolate changes in material behavior such as stiffness from geometrical changes in high strain MD simulations.

3.3.2. Direct Measurement of Damage and Induced Anisotropy

The true stress-strain results for the reactive and classical forcefields are compared in Figure 3.2. The stress magnitude discrepancy between the potentials is a product of both the difference in strain rates and the force field parametrization, but qualitatively, the results are similar. Both show an initial yielding followed by a plastic regime with gradual strain hardening, and the reloading stresses in both cases slightly overshoot the flow stresses and then continue following the base monotonic load path. The flow stress is similar to what has been observed in some experiments and other MD simulations, and may be attributed to the relatively low equilibration time (Cao & Wei, 2007; Sun & Wagoner, 2011). In addition, both force fields exhibit energy dissipative hysteresis loops indicative of viscoelastic behavior, as seen in physical experiments as well as in previous atomistic studies on cyclic loading (Cao & Wei, 2007; Yashiro et al., 2010). The primary difference between the averaged simulations is the stress drops observed in the reactive simulations at high strains. Averaging results over multiple sample systems reduces sampling errors and is more computationally efficient than simply using larger systems, but because damage initiation is sensitive to local topology, the size effects become more prevalent in MD simulations performed within the damage regime. This is what causes the expansion of the confidence interval for loading starting around 60% strain in Figure 3.2. Consequently, merely viewing the means and standard deviations of the results leads to an inadequate description of the results.

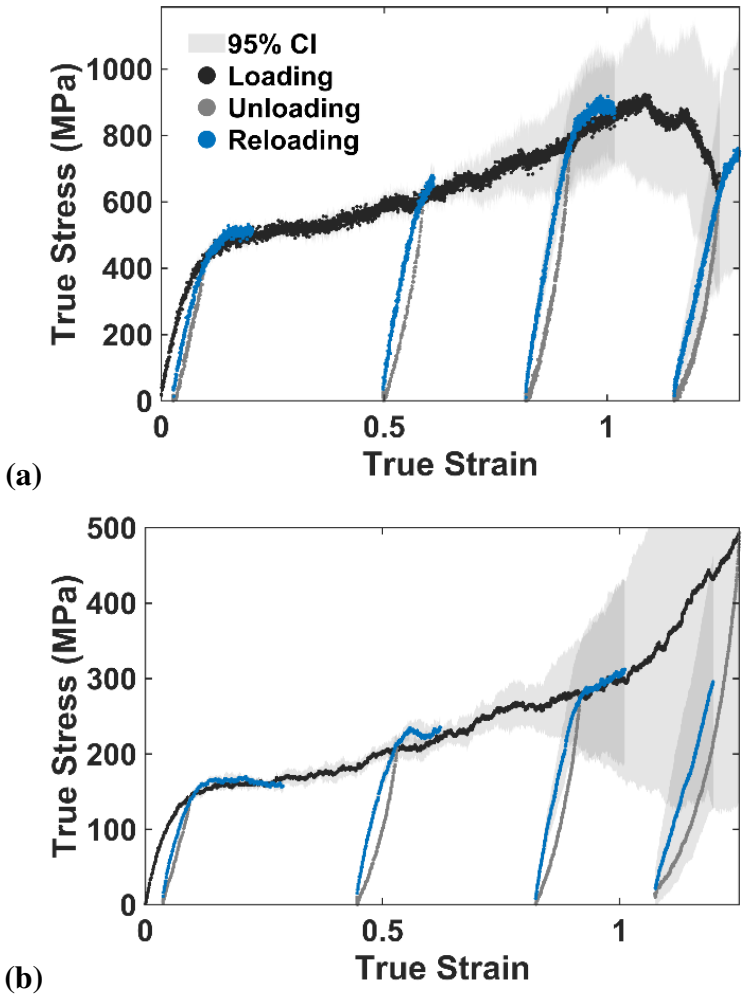

Figure 3.2. Averaged Stress-Strain Results for Molecular Dynamics (MD) Loading Simulations Using (a) Reactive and (b) Classical Force Fields.

The stress-strain response for individual samples, obtained using both the classical and reactive force-fields, are presented in Figure 3.3. For clarity, only the base loading trajectories are shown, and the bond order forcefield results were averaged over a larger interval than was used in the previous figures. These results illustrate the source of variation at high strains: damage initiates at varying values of strain due to the differing initial topologies. In addition, for the classical simulations, the high stress of a single outlier case (sample 4) distorts the average even further. In classical force fields, bonds are generally

permanent, and the bonding terms are harmonic. Consequentially, bond stretching far from equilibrium positions causes unrealistically high stresses, which is the primary limitation of the classical forces in mechanical testing simulations. Most of the classically defined sample molecular structures were able to reorient to find lower energy configurations that relieve stress; however, the molecular structure of sample 4 was unable to find such a configuration, forcing the bonds to stretch to unnatural lengths. Although sample 4 also exhibited the highest stresses for the reactive force field simulations, the capacity for bond breakage allowed it to relieve some stress via molecular scission when it was unable to do so through reorientations. An average of over 53% of the atoms in these 80% crosslinked systems are connected in a single periodic molecular network structure, so inevitably, at some strain, every classical case would eventually fail to reorient to lower stresses thereby experiencing steep increases in bond energy and precluding failure simulation. Higher crosslinking degrees would further inhibit the ability of a thermoset structure to find lower energy configurations via pure reorientation. In contrast, larger systems would provide more opportunities for finding stress relieving arrangements.

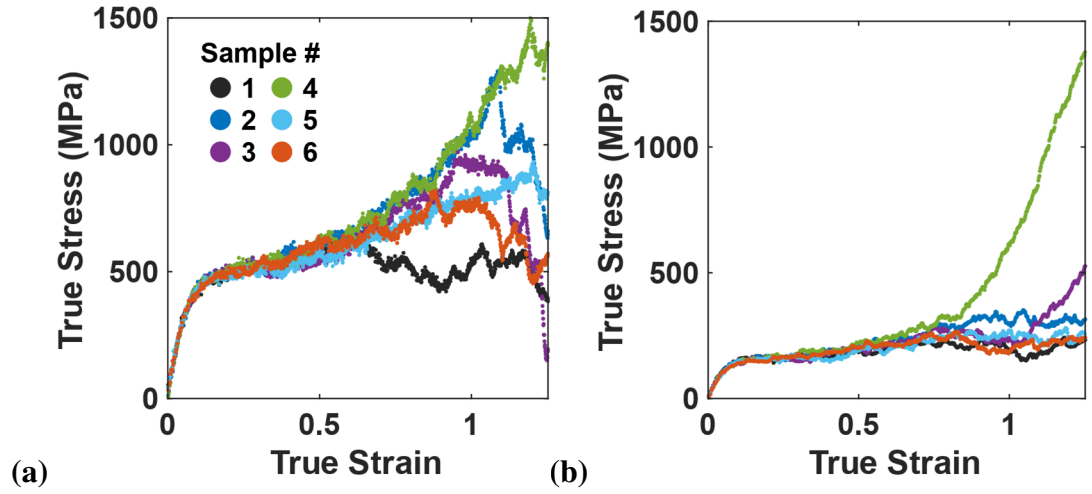

Figure 3.3. Stress-Strain Results for Individual Molecular Dynamics (MD) Loading Simulations Using (a) Reactive and (b) Classical Force Fields.

Damage cannot be directly inferred from the base stress-strain loading simulations since softening and hardening behaviors may not be directly coupled to changes in stiffness. Hence, stiffness changes were directly calculated using the reloading simulations. Ideally, the Young's Modulus calculated from an unloading simulation would be identical to the Young's Modulus calculated from the corresponding reloading simulation; however, the viscoelastic behavior, nonequilibrium conditions, and the nonlinear elasticity caused by molecular alignment cause the initial unloading stiffness to be slightly higher than the stiffness calculated from reloading. Thus, for consistency the evolution of the stiffness was tracked by calculating Young's Moduli for the initial portions of each reloading simulation, up to 2% strain. In addition, the mechanically induced anisotropy was quantified by also reloading the system in an off-axis direction and comparing changes in stiffness and yielding. Figure 3.4 shows the evolution of the stiffness in the on-axis and off-axis directions for both the reactive and classical force fields. Although not shown, it is also

interesting to note that in conjunction with the on-axis hardening, the strength in the off-axis directions consistently decreased with increasing strain.

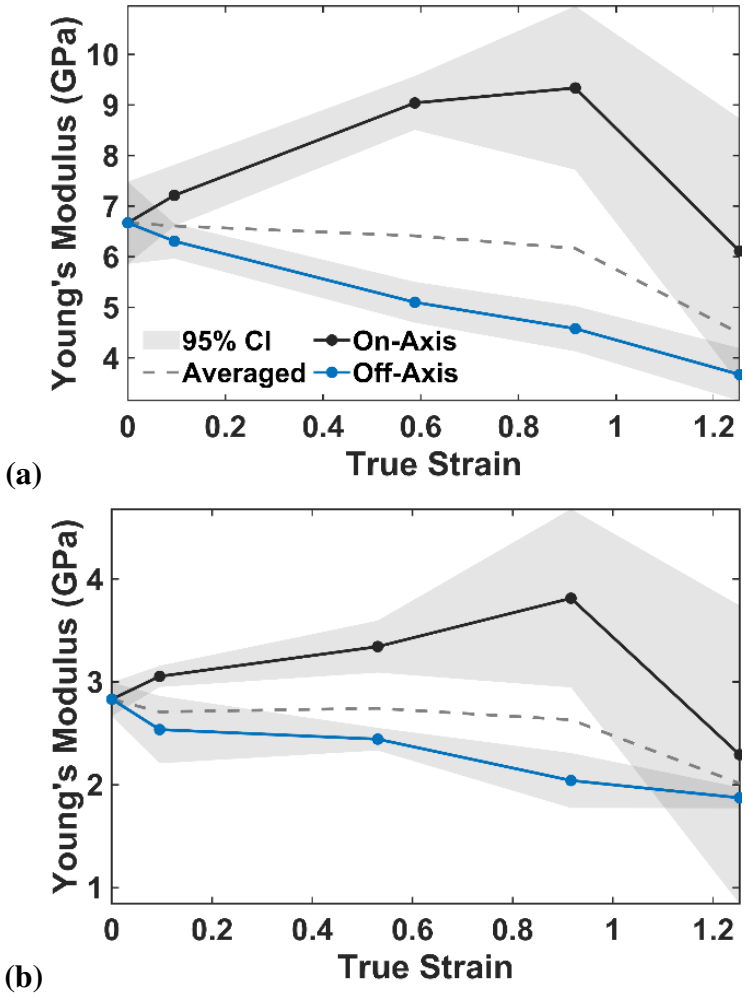

Figure 3.4. Averaged Stiffness in on Axis and off Axis Directions at Each Unloading Point for (a) Reactive and (b) Classical Force Fields.

Figure 3.4 demonstrates several interesting results. The stiffness in the on-axis direction increases for the first three reloads, while the off-axis stiffness decreases. Since the stiffness of a system is essentially governed by the minimum density of covalent bonds in the direction of load application across a perpendicular cross section, this mechanically

induced anisotropy indicates that, overall, the bonds are realigning in the load direction, sacrificing entropy to reduce stress. The molecular alignment, or strain induced crystallization, observed in this study is generally associated with thermoplastic and elastomeric polymers (Caruso et al., 2009), but these results demonstrate that this mechanism also occurs in highly crosslinked polymers within localized areas of large strains. This is consistent with several experimental studies that found that even the brittle crack propagation of epoxy polymers involves localized energy dissipative processes such as shear yielding and crazing (Fard et al., 2012; Kinloch, 1985; Rahul & Kitey, 2016; Sue et al., 1993). Although the mechanically induced anisotropy is a localized event that would not be observed at the macroscale, the damage results are relevant at the macroscale because damage reflects the weakest links in a material, not just the averaged behavior.

In the final reloading simulation, the stiffness in all directions decreases; thus, the thermoset experiences the combined effects of bond realignment and damage. In an effort to separate the magnitude of damage from the effects of localized molecular bond alignment, the overall stiffness for each case was averaged over the on-axis and twice the off-axis directions, as represented in Figure 3.4. The results show that for the first three reloading simulations the net stiffness remains nearly constant, decreasing only slightly, until finally it drops considerably in the last reloading simulation. This indicates that the consistent off-axis stiffness loss cannot be initially attributed to damage, but rather is a result of bond alignment in the loading direction. However, because the damage is clearly anisotropic, the net stiffness loss in the last reloading simulation should not simply be converted to a single damage parameter. It is more difficult to directionally decouple

damage from bond alignment, though the differences in variation between the on-axis and off-axis directions suggest that the damage develops primarily in the loading direction, as would be expected. In addition, because the damage for each individual sample initiates at different points, the rate of damage after initiation for a single case is more severe than in the averaged trend, and identifying a damage initiation point is not trivial since it depends so heavily on the stochastic initial molecular topology, as illustrated by the large on-axis variation. Moreover, the localized nature of the strain is difficult to correlate to the macroscale strains due to the time and length scale incompatibilities.

Although damage in thermoset polymers is generally attributed to cracks formed due to bond breakage, Figure 3.4 shows that damage initiation is observed even in the absence of bond breakage with the classical force field. Moreover, the stiffness evolution paths computed for the bond order and classical force fields follow a similar trend. These results demonstrate that molecular systems will tend to exploit bond breakage only as a last resort for stress alleviation. This aligns with the results of a largescale MD study on thermoset fracture, which found that a uniaxial strain tensile simulation only observed 0.2% bond breakage for 100% extension and less than 2% bond breakage for complete material scission (Yang & Qu, 2014). Larger systems with more degrees of freedom would likely require even less bond breakage, so it stands to reason that bond breakage in a macroscopic system is limited. Therefore, although total material failure requires molecular scission, damage initiates with minimal bond breakage through disentanglement mechanisms.

3.3.3. Void Volume Analysis

Though cracks and voids are typically considered to be microscale phenomena, these features must inevitably initiate at the nanoscale, so to correlate stiffness loss in the material to the generation of voids, the void volume was calculated as the strain progressed. The void fractions were calculated according to the Delaunay meshing algorithm implemented using the "construct surface mesh" modification in Ovito (Stukowski, 2010, 2014). A relatively large probe radius of 5 Å was employed to avoid including small elastic cavities in the void volume calculations. The deformation trajectories and void growths for reactive and classical force fields were found to be similar, but because the void formation in classical force fields is more interesting and nonintuitive, the visualizations are shown for one of the classical force field samples after each unloading simulation in Figure 3.5. The results are shown for sample 5 because it exhibits stress-strain behavior closest to the average. Note that because the visualizations are based on the state of the system after each unloading simulation, the systems shown are in zero stress configurations and the voids observed for higher strains are stable.

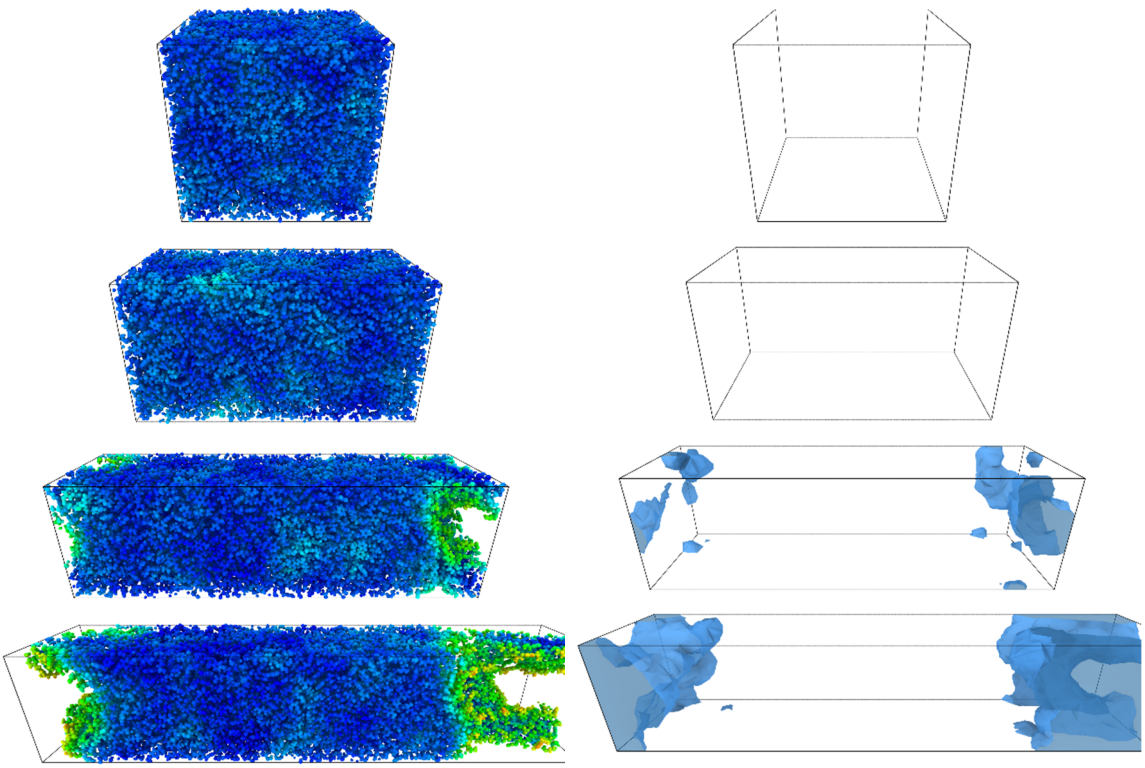

(a) **(b)**

Figure 3.5. Snapshots of (a) the Molecular Structure Colored by Coordination Number and (b) the Void Volume for a Single Case (Sample 5) After Each Unloading Simulation for the Classical Force Field (10, 53, 92, and 125% Strain, Respectively).

Due to the periodic boundary conditions, the scattered voids shown in the third stage of Figure 3.5 are actually just two voids, one large and one small, and in the final image they have coalesced into a single larger void. The configuration of the void is consistent with damage concentrating in the on-axis direction. The deformation in the final stage of Figure 3.5(a) shows the onset of nanoscale crazing, which, considering the size of the system and the rigidity associated with the crosslinks and complete higher-order all-atom bonding descriptions, may be considered an unexpected phenomenon. Nevertheless, other studies corroborate this result, having detected crazing in some crosslinked polymers (Fard

et al., 2012; Henkee & Kramer, 1984; Kinloch, 1985; Lilley & Holloway, 1973; Plummer & Donald, 1991; Rahul & Kitey, 2016; Sue et al., 1993), in contrast to some claims that crazing is limited to thermoplastics (Caruso et al., 2009; Zhang et al., 2009). Studies indicate that the prevalence of crazing depends on the degree of crosslinking (Henkee & Kramer, 1984; Plummer & Donald, 1991), and the relative activation energies of the thermoset constituents would also influence the occurrence of crazing by altering the ratio of crosslink to chain bonds (Schichtel & Chattopadhyay, 2019).

The evolution of the void fraction is shown for each sample in Figure 3.6. These trajectories show a clear initiation point of void formation in each sample and similar rates of void growth between samples and force fields, but the point of void nucleation varies between samples depending on the initial topologies. The voids initiate past 60% true strain, consistent with the increase in variation in the stress-strain diagrams and stiffness evolution plots. The lack of void growth in sample 4 for the classical outlier case explains the high stresses seen in Figure 3.3, and confirms the notion that void growth is a stress alleviation mechanism. With a larger sample, this structure would not be forced to stretch because other weaker regions would release stress alternatively.

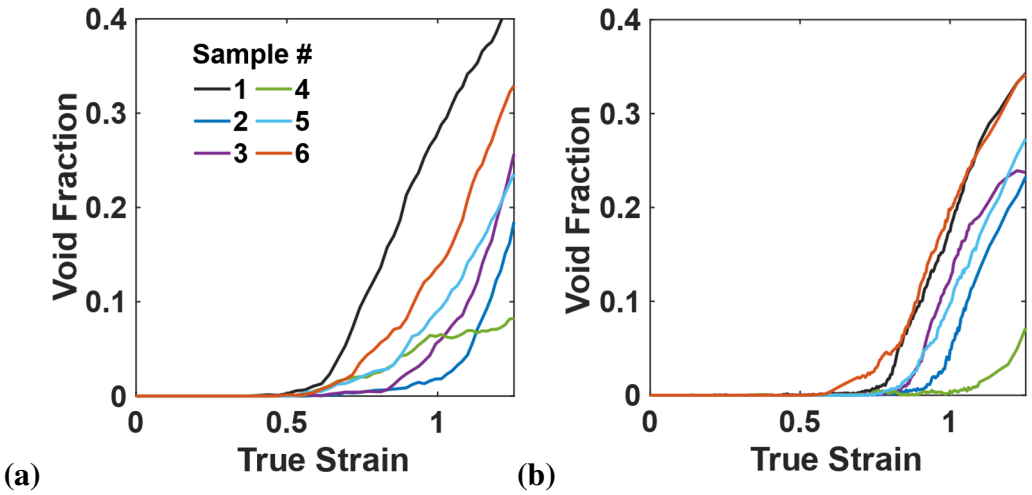

Figure 3.6. Evolution of the Void Fraction for Individual Molecular Dynamics (MD) Loading Simulations Using (a) Reactive and (b) Classical Force Fields.

To compare the evolution of the void fraction to the overall changes in volume or density, plots of the Jacobian determinant are shown in Figure 3.7 for both the bond order and classical force fields. Note that the Jacobian determinant, which can be derived from F, is simply the instantaneous volume/density normalized by the reference volume/density. The resemblance between the density evolution and void growth plots shows that the sudden change in the rate of growth of the Jacobian is a direct result of void nucleation. The averaged results in Figure 3.7(c) and (d) show that the slopes of the Jacobian unloading paths are relatively consistent regardless of the state of deformation. Furthermore, even the unloading paths before void formation do not return to the original values. The results were similar for the potential energy of the system which did not return to the reference value, even prior to large void growth nucleation. This indicates the presence of damage before the large voids and crazes begin to form, consistent with the slight net averaged stiffness degradation observed in Figure 3.4. However, damage cannot be directly determined from the changes in density during loading because they combine elastic density changes with

permanent void growth, and the lengths of the unloading paths depend on the state of deformation. The most accurate measure of damage based solely on the deformation would be derived from the permanent density change at every point along the trajectory, which could be obtained via a substantial number unloading simulations; nevertheless, the void growth trajectory approximates this density change fairly well, without the need for unloading simulations.

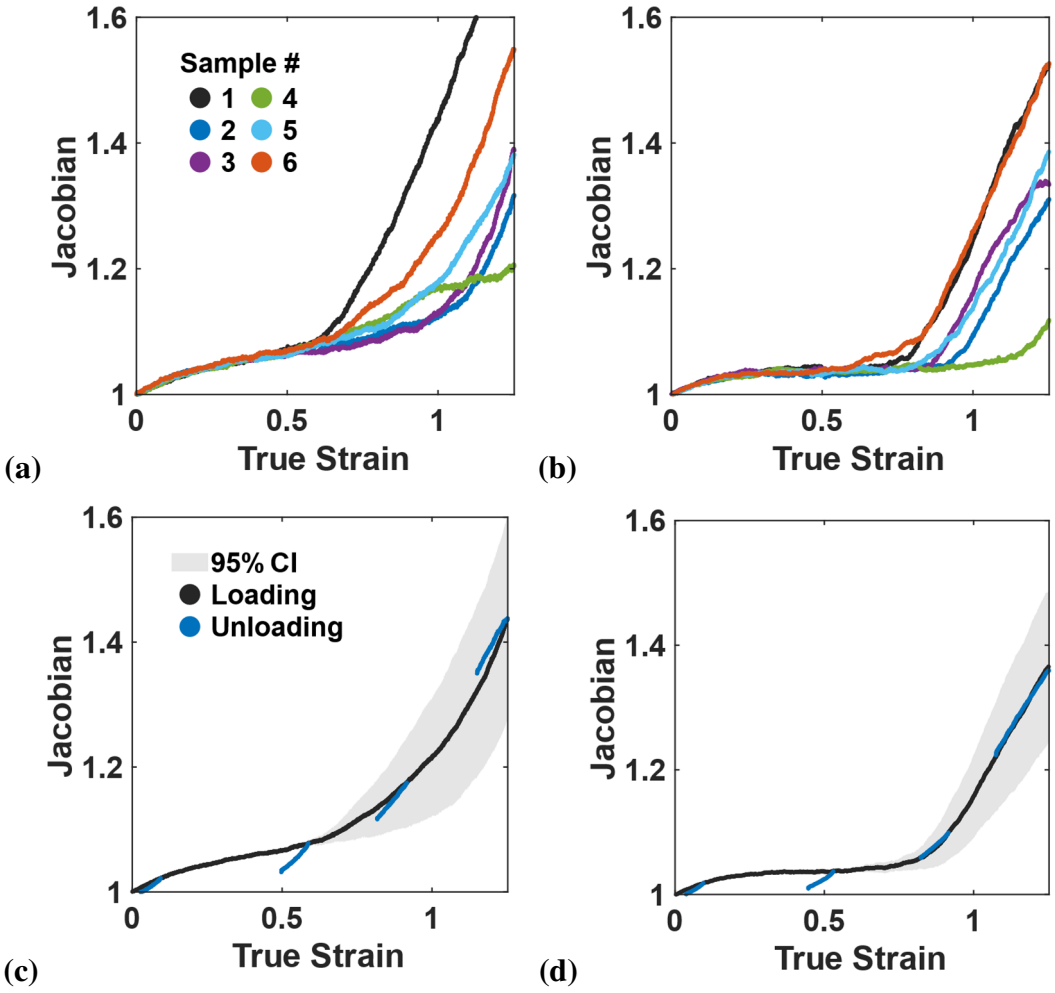

Figure 3.7. Evolution of the Jacobian for Individual Molecular Dynamics (MD) Loading Simulations Using (a) Reactive and (b) Classical Force Fields, and for the Averaged Jacobian During the Loading and Unloading Simulations for (c) Reactive and (d) Classical Force Field.

The variability encountered post-yield in all the above analyses is important to consider in order to understand the relevance to higher length scales. Many MD studies on metals use perfect crystal structures without variation, and many studies on polymers use only a single sample to save computational costs, but to account for topological variation, the simulations in this study were performed on six samples with stochastically unique molecular structures. The elastic and initial plastic response exhibited little deviation

between the samples, but there was large variation between samples for damage initiation as manifested by the inconsistent onset of void nucleation and on-axis stiffness degradation. The initial regimes are governed by bulk properties such as density and crosslinking degree, so they are not highly sensitive to topological variation. In contrast, damage is dictated by outliers, not averages; damage originates locally from the weakest regions of a material, so it is sensitive to subtle topological changes. For this reason, the averaged results of nanoscale systems should not be taken as damage for a bulk material since damage will be governed instead by the weakest atomistic location in the entire macroscopic material. Furthermore, the large strains and the mechanically induced anisotropy are purely local events, making it difficult to relate to the macroscopic material behavior and validate legitimate integration into multiscale models. Therefore, even though these MD simulations are fully capable of capturing damage and complex material response, the high dependence of damage initiation on local topological variation necessitates caution for the use of MD damage studies in multiscale integration frameworks.

3.3.4. Comparison of Differential and Averaged Poisson's Descriptions.

The Poisson's ratio is important to analyze because it is directly related to the rate of density changes, and its evolution provides information on the deformation trajectory. Furthermore, a complete constitutive description of an isotropic material requires the definition of both the Young's modulus and the Poisson's ratio. In this section, the localized evolution of the Poisson's ratio is analyzed and related to the state of deformation.

Determining the Poisson's ratio at any point in the deformation is less complicated than determining the Young's Modulus because it does not require unloading-reloading simulations. The Poisson's ratio is typically calculated by taking the ratio of the total transverse strain to the total axial strain at any given point, but taking the ratio of the differential transverse strain to the differential axial strain at any given instant provides a more accurate representation of the changes in the Poisson's ratio. The bulk modulus of a material undergoing triaxial compression can be treated in a similar manner. In Figure 3.8 Poisson's ratio calculations are compared for both force fields averaged over the six samples.

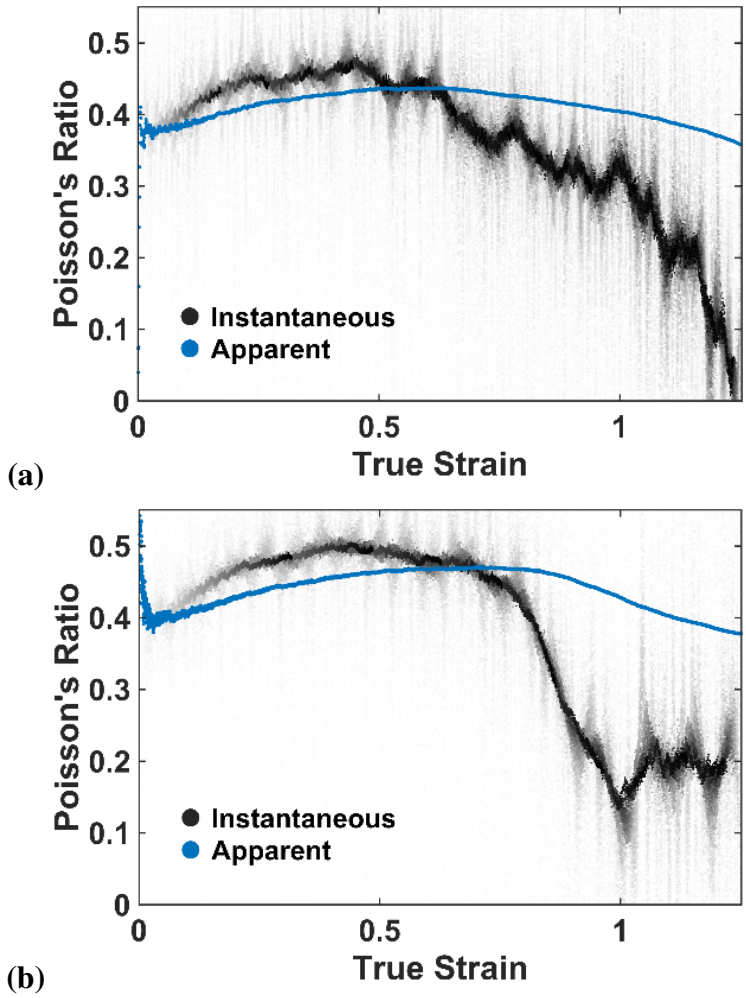

Figure 3.8. Evolution of the Poisson's Ratio Shown Through Both the Differential and the Cumulative Effect Definitions for (a) Reactive and (b) Classical Force Fields.

Due to the high noise intrinsic to the differential Poisson's ratio in MD simulations, the instantaneous results are visualized by averaging locally over a range of intervals, with the darker points corresponding to larger interval averages. These results demonstrate how the instantaneous differential definition of the Poisson's ratio avoids lag and gives more meaningful information on the current state of the material. The results indicate that initially the Poisson's ratio is around 0.4, but with the onset of plasticity, the value rises to 0.5, corresponding to volume conserving deformation. Finally, the Poisson's ratio drops as

damage initiates. Because the damage is averaged over the six samples, the Poisson's ratio drops are much more gradual than for individual cases, and the instantaneous Poisson's ratio appears to decrease more gradually for the reactive force field because the damage nucleation points have greater variance between the six samples. The Poisson's ratio relates to rate of density changes, so the drops in the instantaneous Poisson's ratio mark the void nucleation and damage initiation, corresponding to the abrupt increases in the Jacobian.

3.4. Summary

In this chapter, all-atom MD simulations were used to investigate damage initiation and localized anisotropic mechanical property evolution in thermoset polymers under uniaxial tension through a set of unloading and reloading experiments. The unloading and reloading experiments were performed from various points along the main loading trajectories in both the on-axis and off-axis directions using both classical and reactive force fields. The results of these simulations lead to several interesting conclusions:

- Damage can be effectively captured in MD simulations via the direct stiffness loss calculated from the reloading simulations, but fully Eulerian frames of reference must be employed in order to accurately evaluate changes in material stiffness in high strain MD simulations.
- Thermoset polymers exhibit the combined effects of damage and anisotropic changes in stiffness in regions of localized strain near substantial damage events, corresponding to crazing and general bond alignment.

- Bond breakage plays a minimal role in damage initiation for thermosets despite their brittle macroscopic behavior, due to the highly localized plastic deformation mechanisms.
- The growth of the void fraction revealed sudden initiation points and consistent growth rates, which correlate to sudden changes the Poisson's ratio and the rate of change of density. Unloading simulations demonstrated permanent density loss even before the main void nucleation, resulting in slight stiffness loss, but most stiffness degradation was observed concurrent to the development of relatively large voids, consistent with the conventional concept of damage.
- Although these MD simulations enable the analysis of complex material response, the variability of damage initiation and topological sensitivity necessitates caution for use in multiscale integration.

CHAPTER 4.

ULTRASONIC FATIGUE OF ALUMINUM ALLOY 7075-T6*

4.1. Introduction

Aluminum alloys in aerospace applications often require a fatigue life of over 10^8 to 10^9 cycles, which is well over the number of cycles that can be practically tested using conventional fatigue testing equipment (L. Xu et al., 2018). Achieving these high numbers of cycles requires the utilization ultrasonic fatigue frames, which operate under a completely different set of principles. Therefore, in this chapter, a detailed ultrasonic cycle fatigue study is presented for AA7075-T6 under fully reversed tension-compression loading to investigate the geometric sensitivity, frequency effects, size effects, surface roughness effects, and the corresponding failure mechanisms for ultrasonic fatigue across different fatigue regimes. The dominating sources of life variability are identified using sensitivity studies conducted using FEA-based modal analyses and probability studies for typical ultrasonic fatigue specimens. In contrast to some studies of crack initiation for aluminum alloys under fatigue, subsurface crack initiations were observed for low stress amplitudes. The presence of both surface and subsurface crack initiations is strongly correlated to the surface conditions and loading conditions. Fatigue-fracture behavior is

* This chapter is based on the author's previously published journal article (Schichtel et al., 2022).

evaluated via detailed SEM analysis of fracture surfaces, exhibiting unique features that are not observed under conventional fatigue testing of aluminum alloys.

4.2. Specimen Analysis

The study of fatigue in the ultra-high cycle regime is performed with ultrasonic fatigue testing equipment, which cycles at approximately 20 kHz using a piezo-electric converter with a sonotrode to amplify displacements applied to the specimen. Although numerous ultrasonic fatigue testing systems exist (Ilie et al., 2020), they all operate under the same principles. Unlike traditional fatigue testing machines that use an external loading frequency different from the natural frequency of the specimen, ultrasonic testing equipment utilizes the natural frequency of the specimen to excite the axial tension-compression resonant mode. This allows the machine to produce relatively high strain in the specimen through a standing wave, despite the relatively low displacements applied to the end of the specimen. Because the machine requires the specimen's natural frequency of the tension-compression mode to be approximately 20kHz, the specimen design is critical. The specimen geometry analyzed in this study is well-established by Bathias and Paris, so the design procedure is not covered (Bathias & Paris, 2004).

4.2.1. Specimen Geometry

Standard symmetrical hourglass specimens with circular sections were employed for the ultrasonic fatigue testing, and the dimensions were calculated according to the standard equations (Bathias & Paris, 2004; Lage et al., 2012). The ultrasonic testing machine

automatically halts when the frequency falls below 19.5 kHz, which happens when a large crack forms, effectively reducing the stiffness of the specimen. The first six tests were run with the dimensions given in Figure 4.1(a), but the specimens failed without breaking completely; cracks could be seen along most of the circumference of the gauge sections, but the specimens did not fracture completely. Therefore, in order to properly study the fatigue fracture surface, additional specimens were designed with a smaller gauge section, such that failure would result in complete scission, eliminating the need to force them apart, which would potentially affect the fracture surface. The dimensions for these specimens are shown in Figure 4.1(b).

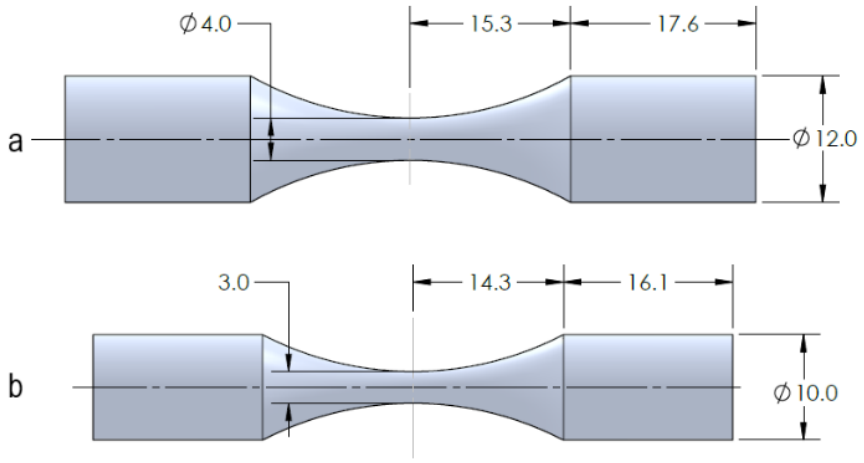

Figure 4.1. Geometry and Dimensions of (a) the Large Specimens and (b) the Baseline/Rough Specimens for Ultrasonic Fatigue Testing.

4.2.2. Finite Element Stress Calculations

A commercial FEA (ANSYS) was used to calibrate stress-displacement relationships and calculate stress concentrations and risk volumes, using a swept quadratic hexahedral mesh. To correctly compute the modal frequencies, all boundaries were left traction-free

(Mayer, 2016). The first five nonrigid, lower energy modes correspond to four flexural and one torsional deformation modes, while the sixth corresponds to the longitudinal tension-compression mode. The simulated natural frequencies and mode shapes are given in Table 4.1, and these calculations validate that the natural frequencies of the specimens are well within the tolerance of the ultrasonic testing machine.

Table 4.1 First Six Non-Rigid Simulated Natural Frequencies and Mode Shapes.

Mode Number	Mode Shapes	ω_n of Baseline Specimens (Hz)	ω_n of Large Specimens (Hz)
1	First Order Bending	2605.6	3063.9
2	First Order Bending	2605.6	3063.9
3	Axial Torsion	4784.3	5232.5
4	Second Order Bending	13474	14746
5	Second Order Bending	13474	14746
6	Axial Tension/Compression	20220	20019
7	Third Order Bending	47517	47171

To determine the maximum stress amplitude, the strain at the gauge section can be measured using aptly placed strain gauges, or it can be indirectly calculated using the displacement amplitudes. For simplicity the displacement amplitude was used to compute the maximum stress. Because the gauge central profile can be closely approximated as a hyperbolic cosine curve, the averaged stress distribution can be analytically solved from the one-dimensional partial differential equations. The derivation and equations are shown by Bathias and Paris (Bathias & Paris, 2004); however, due to the one-dimensional assumption of uniform stress across a cross section, the maximum stress given by these equations is lower than the actual maximum stress, since the stress concentrates toward the surface of the gauge section. To analyze the stress distribution and more accurately

calculate the maximum stress amplitude in the specimen, harmonic analysis was performed at the longitudinal mode natural frequency using the calculated dynamic modulus. The harmonic loading was imposed via a constant amplitude displacement boundary condition on the top surface of the geometry, which represents the contact surface between the sonotrode and the specimen. Constant structural damping does not affect results for simple displacement-controlled harmonic analyses, so it was not added. Note that while the solution for this boundary condition matches the solution for a model with a constant amplitude pressure boundary condition and a corresponding magnitude, the frequency response of these two setups differ. The maximum stress frequency response for the displacement-based harmonic shows a different natural frequency than the modal analysis because the boundary conditions restrict the displacement amplitude at different frequencies; the frequency response corresponds to modal analysis with a fixed boundary condition. Therefore, although the stress results at the natural frequency are accurate with the displacement-based harmonic analysis, the frequency response spectrum could only be correctly calculated using the force-based harmonic analysis boundary conditions. The ultrasonic fatigue testing machine imposes a pressure on the specimen, but the pressure magnitude is displacement controlled.

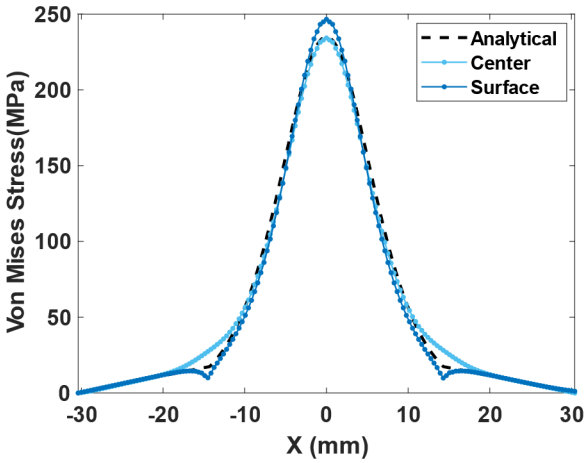

Figure 4.2. Linear Stress Distributions Along the Specimen for the Averaged Analytical Solution and the FEA Model Along the Surface and Through the Center of the Specimen.

In Figure 4.2, the linear stress distributions along the specimen are compared for the averaged analytical solution and the FEA model for the smaller specimen with an applied displacement amplitude of 25 µm at the natural frequency calculated by modal analysis. The FEA distributions are shown both along the surface and through the center of the specimen showing that the analytical solution generally lies between the extremes of the FEA distributions, and the maximum stress amplitude is higher than the stress obtained from the one-dimensional analytical solution as expected due to the effects of the specimen's curvature. Because these simulations are performed within the elastic regime, the relationship between displacement and stress is linear. As a result, the displacement amplitude required to produce a specific stress amplitude can be easily determined from a single simulation. Figure 4.3 shows the stress contours for the surface of the specimen and the stress contour across the minimum gauge cross section. The stress contour of the cross section exhibits stress concentration toward the surface of the specimen with a difference

of over 10 MPa, which likely contributes to the tendency of cracks to initiate at or near the surface of fatigue specimens.

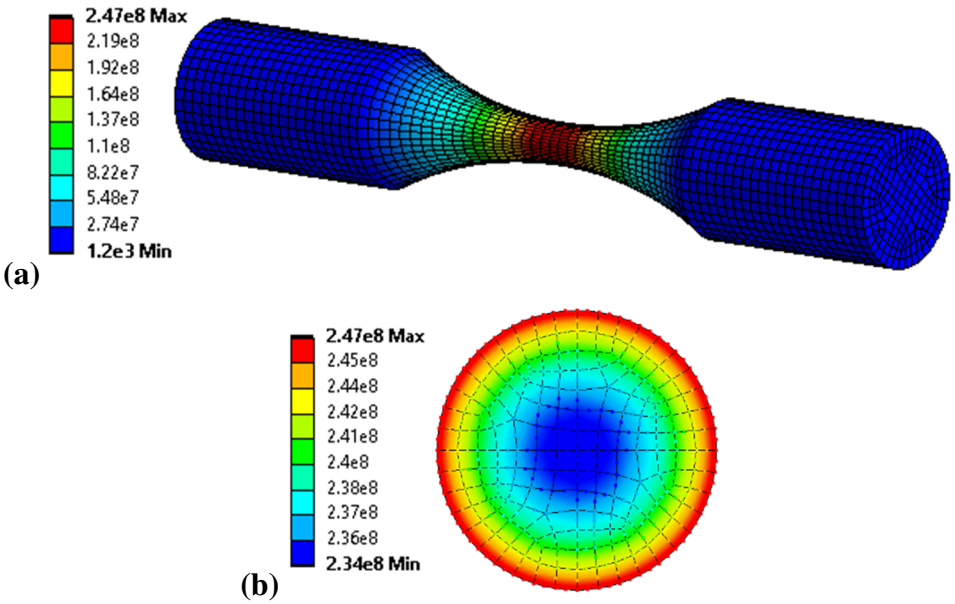

Figure 4.3. The Stress Distribution in Pascals Shown (a) Along the Surface of the Specimen and (b) the Across the Minimum Gauge Cross Section.

To investigate size effects, the stress concentration factors (K_t) and risk volumes were calculated for each specimen geometry as listed in Table 4.2. The stress concentration factors were calculated by dividing the maximum stress amplitude by the average stress in the minimum gauge section in the harmonic analyses. The risk volumes were defined by the volume of specimen that has a stress that is greater than or equal to 90% of the maximum stress in the specimen. The table includes values calculated for the specimen geometry used by Wang et al. for the same material and frequency (Wang et al., 2006, 2010). These specimens have a gauge diameter of 4.0 mm and a continuous gauge radius of 25.0 mm (Wang et al., 2006). The radii of the gauge sections in both the specimen types

used in this study were 31.0 mm; thus, the specimens tested by Wang et al. have the same gauge diameter as the large specimens in this study, but a slightly lower risk-volume, as confirmed in the table.

Table 4.2 Stress Concentration Factors and 90% Risk Volumes for Different Samples.

Specimen Type	K_t	Risk Volume (mm^3)
Baseline/Rough Specimens	1.026	27.6
Large Specimens	1.034	52.5
Wang et al. Specimens (Wang et al., 2006, 2010)	1.043	44.5

4.2.3. Variability Analyses

Because the elastic wave speed depends on the stiffness of the medium, the resonant frequency and stress amplitude of a structure depend on the stiffness of the material in addition to its geometry. The variability of the natural frequency and maximum equivalent stress amplitude with variable geometry, stiffness, and displacement amplitude were analyzed to investigate the most influential factors and support the indirect calculation of stress from the displacement amplitude measurements. Other aspects such as surface roughness and form tolerance could not be included in the study, so the results are not conservative. The six sigma analysis tools in ANSYS were used to perform a design of experiments, generate a response surface model, and determine the output variability. These analyses are exploratory in nature and were not validated experimentally but still provide important insights into the most critical factors for variability. For the input parameters, each of the dimensions shown in Figure 4.1(b) were assigned variation with a standard deviation of 0.00411 mm, which corresponds to the computer numerical control

(CNC) machine's tolerance of 0.0005 in. The dynamic modulus was reasonably assumed to have the same standard deviation as the Young's modulus, so it was assigned a standard deviation of 0.48 GPa from literature (Racha, 2008). The standard deviation of the applied displacement amplitude was calculated to be approximately 0.02 μm according to a typical displacement output of the ultrasonic fatigue machine. The central composite design was used to construct a full 2^{nd} order polynomial response surface using 45 design points. For each design point the natural frequency was first determined using modal analysis and was then used as the frequency input for the displacement-based harmonic analysis. The goodness of fit was satisfactory with a coefficient of determination of 0.99995, an average absolute error of 0.46%, and a relative maximum absolute error of 2.23%.

The PDFs for the resonant frequency and the maximum stress amplitude are shown in Figure 4.4. The distributions exhibit low skewness indicating normal distributions, so the best fit Gaussian distributions are superimposed. These plots show that the natural frequency can vary by approximately 400 Hz depending on the geometry and stiffness, and the maximum stress amplitude corresponding to a selected displacement amplitude of 25 μm can vary by around 10 MPa. These values are not insignificant, so further analysis was performed to examine the most important causes of variation.

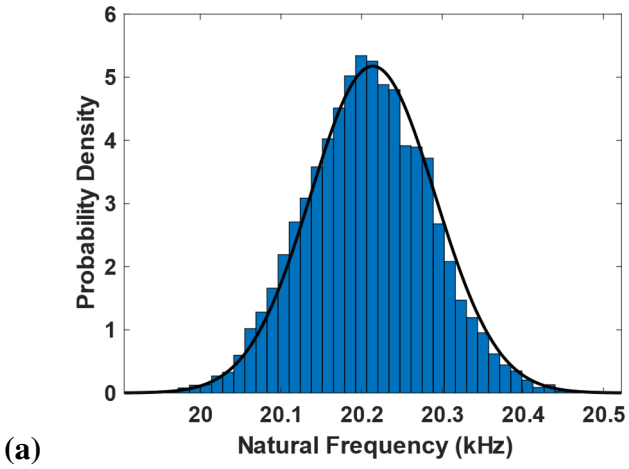

(a)

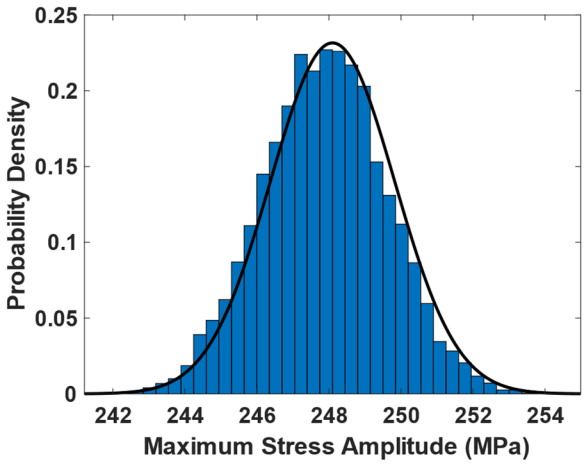

(b)

Figure 4.4. Simulated Probability Distributions With Best Fit Normal Distribution Functions for (a) the Resonant Frequency, and (b) the Maximum Stress Amplitude.

The local sensitivities shown in Figure 4.5 indicate that the variation in the dynamic modulus dominates the output variation of both the natural frequency and the maximum stress. The second largest contributor of variation is the minimum gauge diameter, but even this is far more significant for the resonance frequency than the stress amplitude. The other sources of variation are negligible in comparison. Even the variation in the applied maximum displacement amplitude contributes to less than 10% of the variability. These statistics validate the indirect stress calculation approach using the displacement

measurements because the dynamic modulus would also have to be used to calculate the stress from strain gauge measurements; the variation in stress due to the variability in the dynamic modulus is more significant than the variation in stress that results from the variability of strain caused by geometric and displacement deviations.

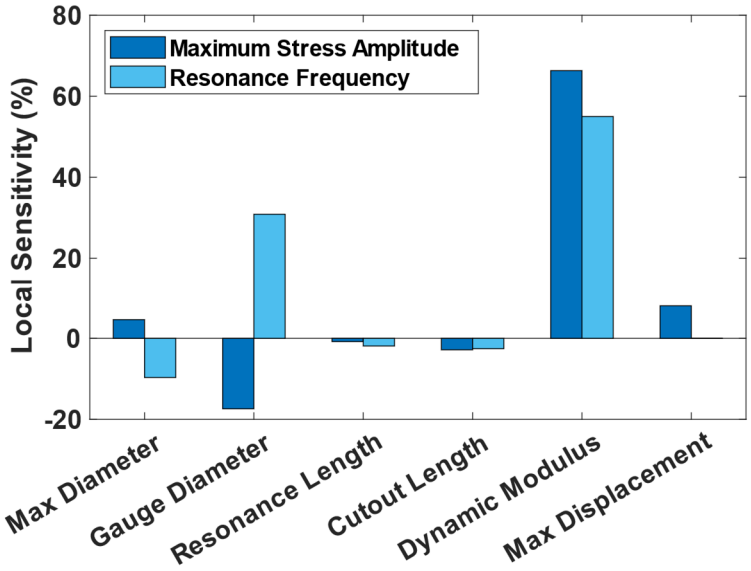

Figure 4.5. The Local Sensitivities of the Maximum Stress Amplitude and the Resonance Frequency to the Geometry, Stiffness, and Displacement Amplitude.

4.3. Experimental Procedure

4.3.1. Material and Specimen Preparation

The material selected for this study was an aerospace grade AA7075-T6 in the form of cold drawn rods. It exhibits a high strength to weight ratio and is typically used in light-weight aerospace applications. The typical chemical composition is shown in Table 4.3. The specimens were machined in line with the axis of the rods such that the grains were elongated in the axial direction of the specimens. The grain size for AA7075-T6 is

approximately 210-250 µm along the axis of the specimen and 70-110 µm in the cross section plane (W. S. Lee & Lin, 2016; Mohan et al., 2016). The baseline specimens were tested as-received (turned on lathe), which has been shown to have similar results to polished specimens (Stanzl-Tschegg et al., 2012), while the roughened specimens were prepared by sanding the gauge section with 80 grit aluminum oxide sandpaper using randomly oriented strokes. The stiffness depends on the rate of deformation; therefore, as summarized in preliminary work (Schichtel et al., 2021), the standard procedure outlined by Bathias and Paris (Bathias & Paris, 2004) was used to precisely determine the averaged dynamic modulus, which was used to design the specimen geometry and calculate the stress. The basic mechanical properties of the material are given in Table 4.4, where E is the Young's Modulus, E_d is the dynamic modulus, ρ is the density, σ_y is the yield strength, UTS is the ultimate tensile strength, δ is the percent elongation, and K_{IC} is the critical fracture toughness.

Table 4.3. Chemical Composition of AA7075-T6 (in wt.%) (*Aluminum 7075-T6; 7075-T651*, 2021).

Zn	Mg	Cu	Cr	Fe	Si	Mn	Ti	Al
5.1-6.1	2.1-2.9	1.2-2	0.18-0.28	≤ 0.5	≤ 0.4	≤ 0.3	≤ 0.2	Balance

Table 4.4. Mechanical Properties of AA7075-T6 (*Aluminum 7075-T6; 7075-T651*, 2021).

E (GPa)	E_d (GPa)	$\rho\left(\frac{\text{kg}}{\text{m}^3}\right)$	σ_y(MPa)	UTS (MPa)	δ (%)	$K_{IC}(\text{MPa}\cdot\text{m}^{\frac{1}{2}})$
71.7	73.0	2810	503	572	11	17.6–29.0

4.3.2. Ultrasonic Fatigue Testing

The ultrasonic fatigue testing was performed on the LASUR Giga Fatigue Machine GF20-K shown in Figure 4.6 at approximately 20 kHz in fully reversed tension-compression ($R = -1$) loading by keeping one end of the specimen completely free. Xu et al. measured the temperature of AA2198-T8 specimens without air cooling using infrared (IR) thermal imaging in real-time and found the temperature evolution was divided into three heating stages: rapid heating (2 to 13 °C increase), slow gradual heading accounting for more than 90% of the fatigue life (2 to 3 °C increase), and a sharp temperature spike (20 to 30 °C increase). By comparing the fatigue lives of uncooled specimens to cooled specimens these temperature increases were determined to have little impact on fatigue life (L. Xu et al., 2018). Nevertheless, in this study a constant stream of cooling air was applied to the specimen and transducer to prevent overheating of the machine and limit thermal effects in the specimen. In addition, the contact surface between the sonotrode and the specimens was carefully lubricated to reduce unwanted contact forces and prevent overheating. More detailed information about the basic setup of the ultrasonic testing machine and standard procedure are given by Bathias and Paris (Bathias & Paris, 2004).

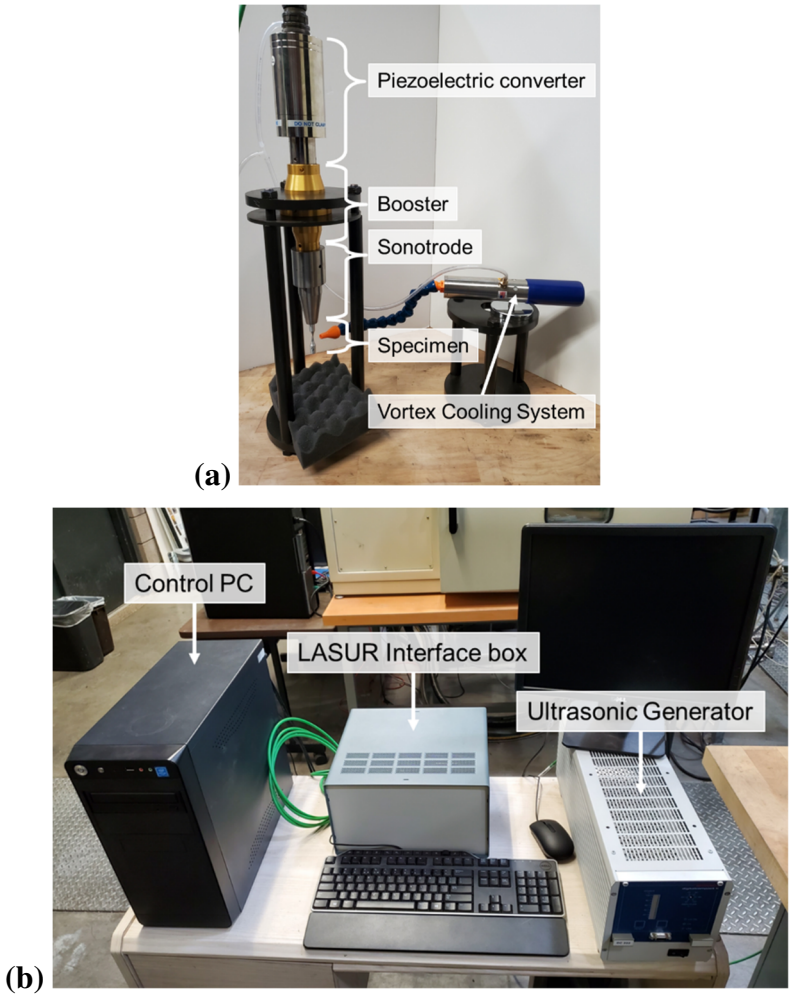

Figure 4.6 (a) Ultrasonic Fatigue Frame and (b) the Corresponding Control Station.

The FEA simulation stress results were used to find a simple linear relationship to calculate the displacement amplitudes required to produce a specific maximum equivalent stress amplitude, and the corresponding nominal stress amplitudes and stress concentration-adjusted nominal stress amplitudes were similarly calculated. Tests were performed on baseline, large, and rough specimens with adjusted nominal stress amplitudes between 171 and 294 MPa by inputting displacement amplitudes ranging from 18.1 to 31.2

μm. The S-N curves were obtained for the specimens tested at different amplitudes, and fractography was performed on a range of failed specimens using SEM.

Some representative frequency and displacement time series are shown in Figure 4.7. An exemplar is shown in Figure 4.7(a), which illustrates the typical frequency settling at the beginning of the ultrasonic experiments, as well as the slight frequency drop that occurs prior to failure that suggests crack initiation or propagation. This aligns with a study that reports crack initiation consumes most of the fatigue life (over 90% when fatigue life exceeds 10^6 cycles and over 99% when fatigue life is above 10^8 cycles) (L. Xu et al., 2018). Moreover, most of the runs did not experience this frequency drop suggesting that perhaps the cracks did not initiate until the final 20k cycles, which would point to crack initiation for these samples expending an even higher percentage of the overall fatigue life. Figure 4.7(b) illustrates the results from an experiment that was restarted multiple times, corresponding to the frequency spikes. A decrease in the natural frequency typically suggests a decrease in stiffness due to damage; however, Figure 4.7(b) demonstrates that the frequency drop at the beginning of ultrasonic experiments is not indicative of damage but rather corresponds to the settling time of the dynamical system and the controller. To reduce the unknown effects of these settling times on the response, no other experiments were performed with restarts. Still, in order to populate a full S-N plot, many tests were performed at higher amplitudes and failed within the settling regime, with a typical response shown in Figure 4.7(c).

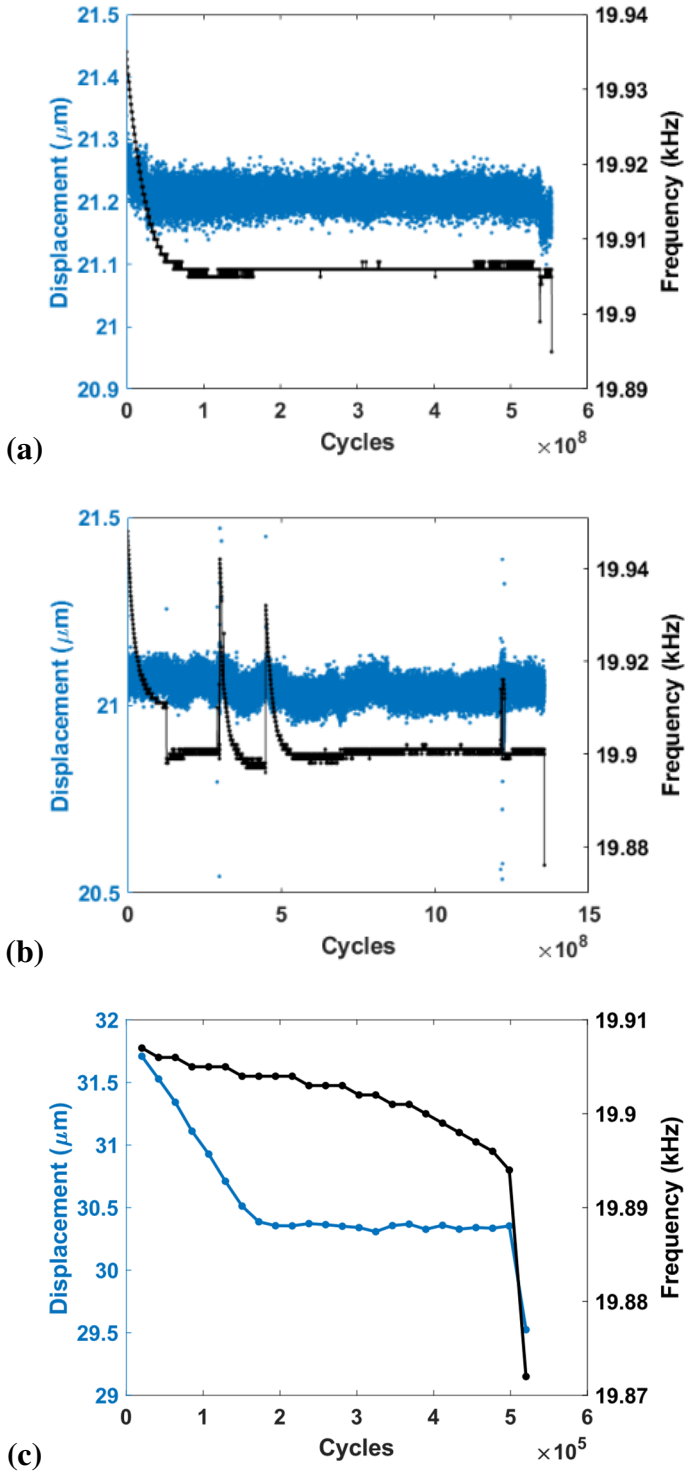

Figure 4.7. The Displacement and Frequency Response Plotted Against the Number of Cycles for (a) an Exemplar Ultrahigh Cycle Test, (b) a Test With Multiple Restarts, and (c) an Ultrasonic Test Performed Under High Displacement.

4.3.3. Characterization of Internal Cracks

Micro-CT has been used in a previous study to detect ceramic particle reinforcements within metal matrix composites tested under ultrasonic fatigue (Wolf et al., 2014), but this is the first study to use micro-CT for ultrasonic specimens to analyze internal cracks. Four of the small specimens failed without fracturing completely, in a manner similar to that of the large specimens. Three of these specimens were scanned using SkyScan 1272 Micro-CT to a resolution of approximately 15 μm. Image reconstruction and segmentation techniques were used to identify the crack and create 3D models of the fracture surface. The specimens were subsequently reinstalled on the ultrasonic fatigue frame and cycled for an additional split-second to make the specimen break completely. The fracture surfaces of the now broken specimens were analyzed using SEM to definitively identify the final rupture region. Note that it is possible that the topology of the final rupture region is affected by the restart and the fact that the specimen could no longer vibrate at its resonant frequency.

4.3.4. Optical Profilometry

The roughened specimens were prepared by sanding the gauge section with 80 grit aluminum oxide sandpaper using randomly oriented strokes. An optical profilometer was used to characterize the roughness of each type of specimen. The sample specimens were prepared by cutting out the center sections of an untested baseline specimens and an untested rough specimen. The linear roughness was measured in the axial direction to reduce the impact of specimen curvature. The optical profilometry results for the typical

gauge surface of a baseline specimen and a rough specimen are shown in Figure 4.8. The linear arithmetic average roughness (Ra) of the baseline sample calculated from the profile in Figure 4.8(a) is 0.74 µm, while the Ra for the rough sample as calculated from the profile in Figure 4.8(b) is 1.29 µm. For reference the Ra for an electropolished specimen was 0.35 µm, while the Ra for a specimen treated with 3mm steel ball SMAT was 1.77 µm (Gao et al., 2020).

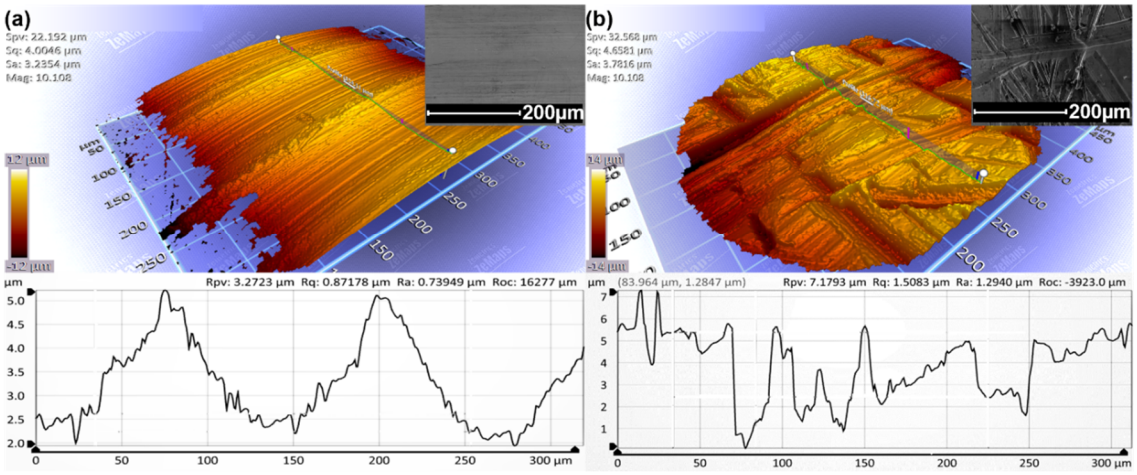

Figure 4.8. Optical Profilometry Results for the Typical Gauge Surface of (a) a Baseline Specimen and (b) a Rough Specimen. The Roughness Profiles Corresponding to the Pinned Lines are Shown Below the Maps, and SEM Micrographs at 350x Magnification are Shown in the Upper Right Corners for Different Specimens.

4.4. Results and Discussion

4.4.1. Stress-Life Data

The stress-life (S-N) plots for the AA7075-T6 specimens are presented in Figure 4.9 including some additional points for reference from Wang et al. for the same material and frequency (Wang et al., 2006, 2010). To separate out the effects of stress concentration in

the S-N plots, the stress amplitudes are K_t-corrected nominal stresses calculated by dividing the average stress in the minimum gauge section by K_t, as identified in Table 4.2. Thus, the size effects and surface roughness effects are effectively isolated; the baseline and large specimen results should differ essentially only by risk volume, while the baseline and rough specimen results should differ essentially only by surface conditions.

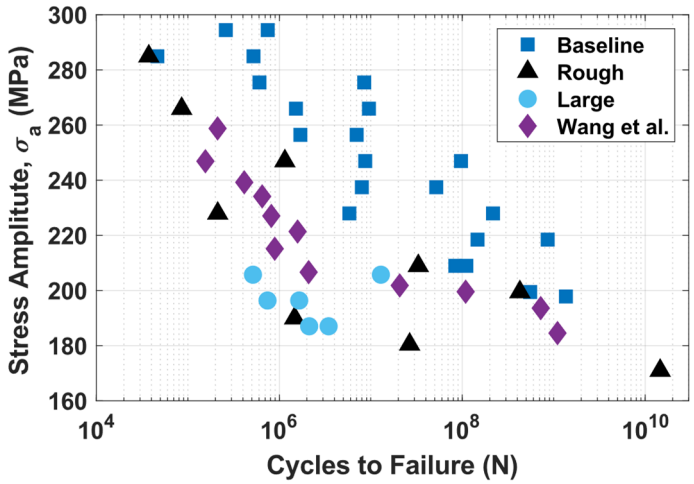

Figure 4.9. The K_t-Corrected Nominal Stress Life (S-N) Curve for AA7075-T6 Specimens With Different Dimensions and Surface Conditions, as Well as Some Additional Points From Literature (Wang et al., 2006, 2010).

Figure 4.9 reveals a significant difference in fatigue strengths between the baseline and large specimens, clearly exhibiting the presence of size-effects in this material. Specimens with a smaller risk-volume have a lower probability of containing inclusions or defects that induce failure leading to the higher strengths exhibited by the small specimens in the S-N curve. Furthermore, the specimens from Wang et al. have a risk volume between that of the baseline and large specimens as given in Table 4.2, and their results lie between the baseline and large specimen results. Thus, size effects may also play a role for the fatigue life of their specimens. Alternative specimen geometries designed to have a larger risk-

volume would abate size effects and reduce variation (Paolino et al., 2014). Guennec et al. demonstrates that the frequency effect extends beyond just the strain rate effects (Guennec et al., 2014), and we suggest that size effects may also play a minor role in the appearance of those frequency effects, since even in their study the risk volume was approximately three times larger for the servo-hydraulic tests compared to the ultrasonic tests despite having identical gauge diameters.

The next key observation is the reduced fatigue life associated with the rougher specimens. If the probability of subsurface failures increases with decreasing load, one might expect that difference in life between baseline and rough specimens would be less prominent at lower loads; however, the results in Figure 4.9 shows that the difference exists across the entire loading spectrum. This is because the surface roughness promotes surface failures in the very high cycle regime when they would otherwise be unlikely, as is further deliberated in Section 4.4.4. In fact, the specimen that failed at 199 MPa and $4.3 \cdot 10^8$ cycles was the only rough specimen observed to have subsurface crack initiation, and accordingly its position on the S-N plot approximately aligns with the data from the baseline specimens. Another takeaway from Figure 4.9 is the absence of an endurance limit within the tested regime. The results from this study do not indicate the existence of a fatigue limit within the test regime, and there were no run-out specimens. In addition, the results show large variability in stress response, as expected. Microstructure plays a key role in fatigue life, which is a key factor leading to the high amount of variability (Castelluccio et al., 2016). To investigate potential variation in failure mechanisms over a

range of loadings, fracture surfaces were analyzed using SEM, as detailed in the following section.

4.4.2. General Fractography

SEM micrographs of the overall fracture surfaces of several specimens across a range of maximum stress amplitudes are shown in Figure 4.10. The arrows indicate crack initiation sites, and the bounded zones highlight regions with distinctive bright and reflective, cleavage-like, crystallographic, faceted topologies that radiate outward from the initiation sites. This region will be herein referred to as the bright, crystallographic region (BCR) because the facets are highly reflective under an optical microscope. For aluminum alloys, these fracture features seem to be unique to ultrasonic fatigue, with only a few recent studies exhibiting similar patterns (Gao et al., 2020; Wang et al., 2010; L. Xu et al., 2018); although, not all AA7075-T6 ultrasonic fatigue tests exhibit these patterns (Arcari et al., 2012, 2015; Stanzl-Tschegg et al., 2016). Nevertheless, the multiplicity of micrographs in Figure 4.10 stress the consistency of these fracture features with the BCR existing in specimens with fatigue lives in the range of 10^5 to 10^{10} cycles. Even the size of the region seems to lack proportionality to the loading and life. Other metals, such as steel, studied in the ultrasonic regime show no evidence of a BCR (Guennec et al., 2014; Mayer, 2016; Sakai et al., 2001). Fractographs for specimens cycled under traditional, low frequency fatigue have completely different characteristics, even for the identical material; the initiation regions lack the characteristic dark zone, and the next propagation region exhibited “river and range” features as well as the presence of fatigue striations, rather than

a BCR (Mohan et al., 2016; Y. Xue et al., 2007). These traditional fatigue tests have been conducted up to 10^6 cycles while the tests in this study have failed down to $3 \cdot 10^4$ cycles, and despite this overlap in testing regime, the features remain unique. This suggests that the observed fracture features are frequency-dependent rather than life-dependent. The fracture surface outside of the BCR exhibits regions with ductile dimples and regions with brittle cleavage facets, which are both indicative of final rupture.

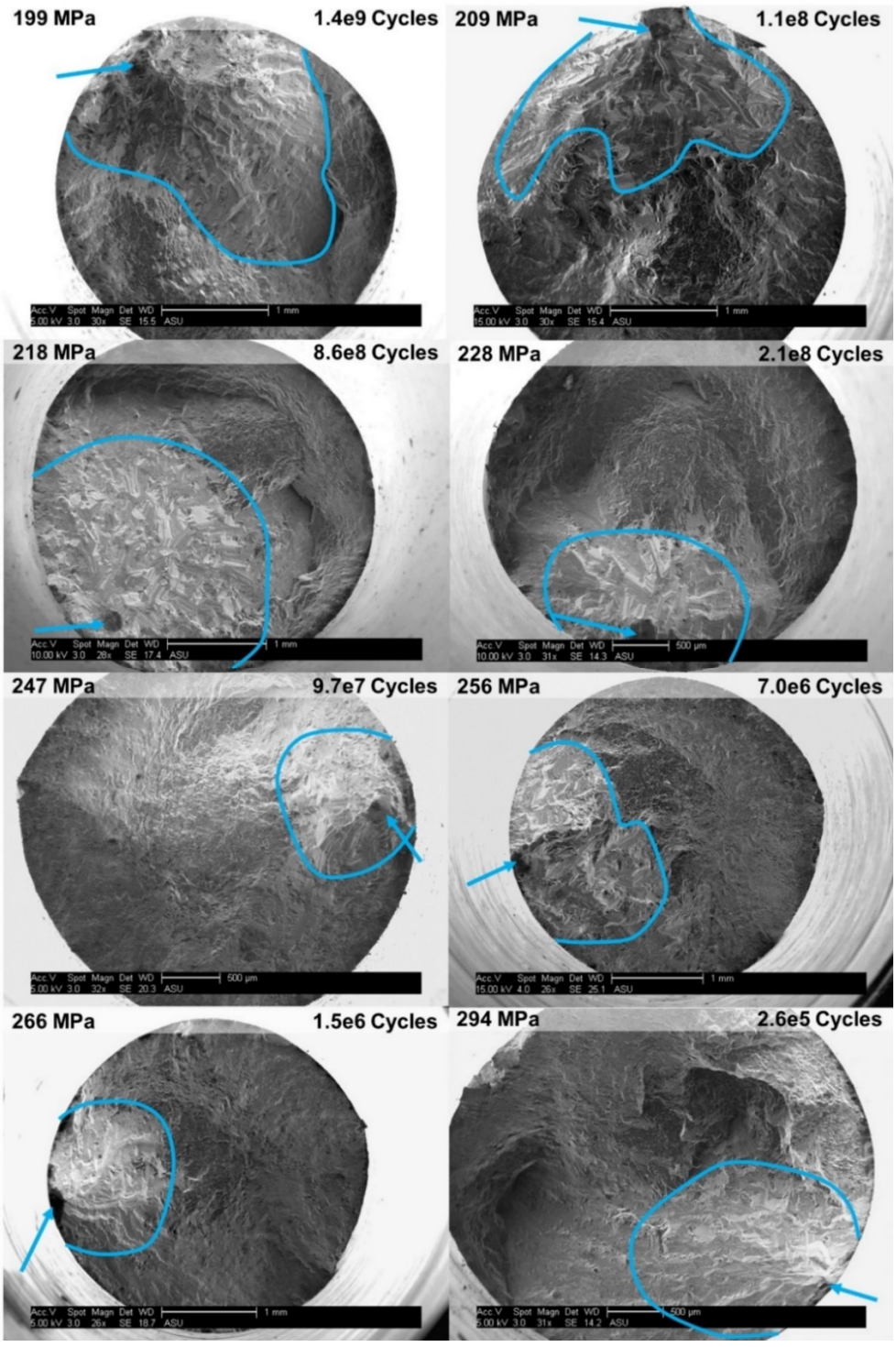

Figure 4.10. Micrographs of the Overall Fracture Surfaces of Specimens Across a Range of Stress Amplitudes. The Arrows Indicate Crack Initiation Sites. The Characteristic Bright, Crystallographic Regions (BCRs) are Encircled.

The crack-initiation sites indicated by the arrows in Figure 4.10 are shown under higher magnification in Figure 4.11. All these sites are located at or near the edges of the specimens, consistent with the FEA analysis in Section 4.2.2, and except for the 256 and 266 MPa specimens, all of these samples show subsurface initiation; even the sample with the highest load appears to have subsurface crack initiation, which is typically observed only for fatigue tests in the ultra-high cycle regime. These results contradict the common presumption that cracks in aluminum alloys under fatigue almost always initiate at the surface, even in the ultra-high cycle regime. Interior crack-initiation sites are commonly referred to as “fish-eyes”, although sometimes the term refers to subsurface crack regions that initiate specifically from an inclusion (Sakai et al., 2010). These dark quasi-circles (semi-ellipses for surface initiations) are said to correspond to the initial slow, stable crack propagation, while the surrounding regions correspond to rapid unstable propagation (Gao et al., 2020; L. Xu et al., 2018). No striations are observed, so it is uncertain as to how long it takes for these regions to develop. The darker color of these regions is likely a concomitant of oxidation induced by the rapid friction heating of crack surfaces after initiation occurs.

The crack initiation sites shown in Figure 4.11 are especially dark when contrasted with the surrounding BCR, but this is not to be confused with the optically dark area (ODA) coined for the region directly adjacent to a fish-eye inclusion (Y. Murakami et al., 2002), just as the BCR is not to be confused for the granular bright facet (GBF), which refers to the brighter region at the center of a fish-eye that is typically observed in the absence of an inclusion (Lu & Shiozawa, 2006). In fact, different authors have assigned different terms

to what is essentially the same region including ODA,GBF, rough surface area (RSA), fine granular area (FGA), and white rough area (WRA), which may lead to some confusion (S. X. Li, 2012; Lu & Shiozawa, 2006; Y. Murakami et al., 2002; Sakai et al., 2001; L. Xu et al., 2018). Regardless of the terminology, this WRA is observed in most of the fish-eyes in Figure 4.11. Only the 228 MPa specimen appears to have initiated at a large inclusion. Similar to the BCR, no relationship is found between the size of the initiation region and the loading and life of the specimen, unlike some other studies that correlate increasing life to the increasing size of the ODA (S. X. Li, 2012; Y. Murakami et al., 2002). The diameters of these regions are consistently around 200 μm across, with the highest loaded sample being the only exception with a span of 30 to 80 μm. Thus, they are generally larger than the size of a single grain (70-110 μm) in the cross section plane (W. S. Lee & Lin, 2016; Mohan et al., 2016). Based on the equation for the stress intensity factor (K_I) at the tip of a penny-shaped crack with radius a, the stress intensity factor ranges between approximately 1.5 and 3.5 MPa $\cdot$ m$^{\frac{1}{2}}$ when the crack transitions from the dark initiation region to the BCR.

$$K_I = \frac{2}{\pi}\sigma\sqrt{\pi a} \tag{4.1}$$

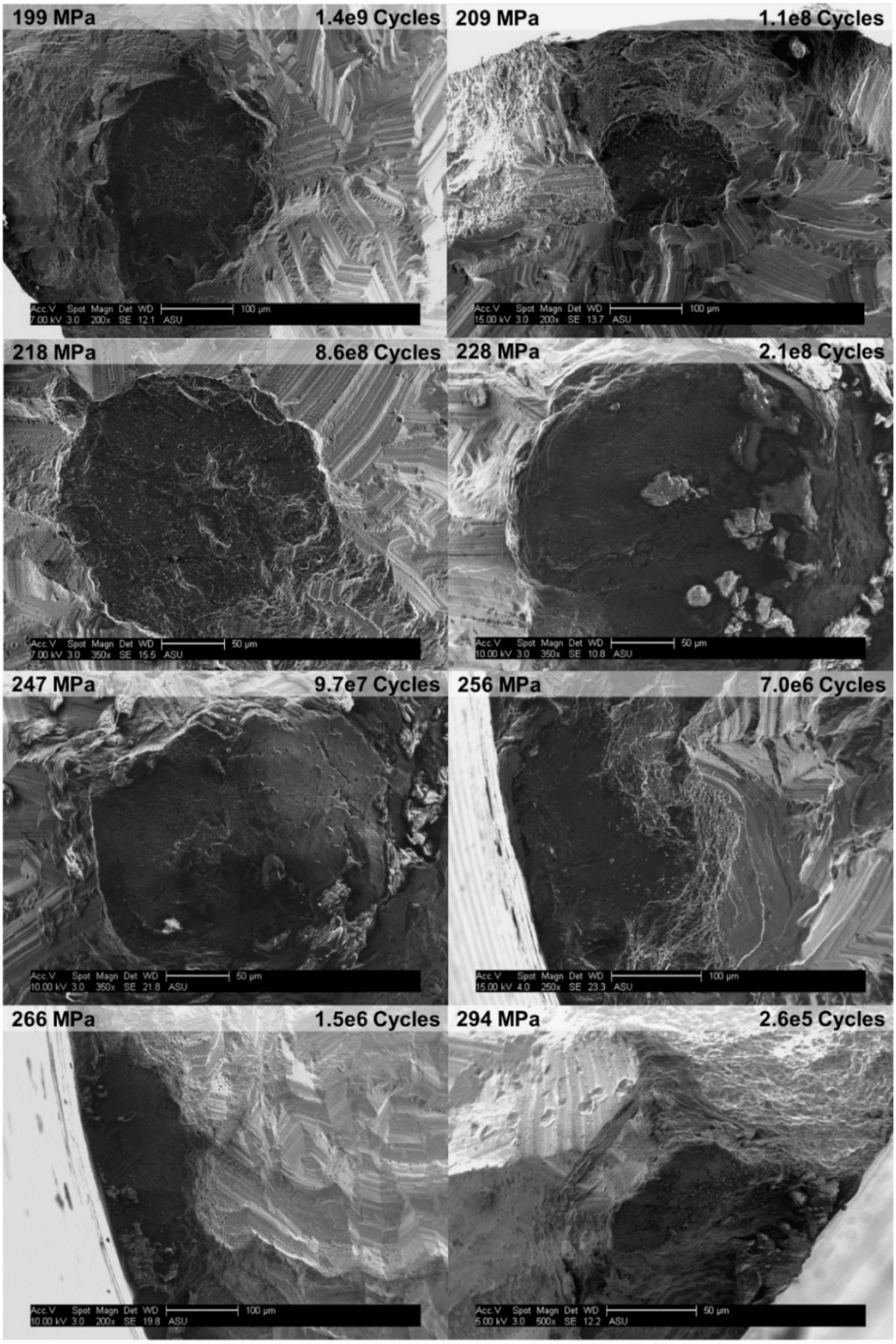

Figure 4.11. Crack Initiation and Initial Propagation Regions Shown for Specimens Across a Range of Stress Amplitudes.

Successively higher magnification views of a typical BCR are shown in Figure 4.12 with a specimen tested at 294 MPa that failed at $2.6 \cdot 10^5$ cycles. Figure 4.12(b) shows the typical parallel line features of the BCR that are in each collection of facets in the general direction of crack growth. Due to the steep incline angle of the BCR, this is easier to notice in Figure 4.14, which shows the side profile views in detail. Results that are reminiscent of the BCR shown in this study have been reported for titanium alloys under fatigue (Brandes et al., 2010; Pilchak et al., 2009; Shi et al., 2019), and, as with these materials, the orderliness of the structure suggests that it is indicative of cleavage-like fracture along preferred slip planes. Although it is common to describe these facets as "quasi-cleavage" and "cleavage-like" for titanium alloys, it has been suggested that the term "cleavage" should not be associated with these features because these features take thousands of cycles to develop, unlike true-cleavage facets which develop within a single cycle (Pilchak et al., 2009). These features may correspond to tortuous initial propagation of stage I fatigue crack growth (Adams, 1987), which would suggest that the darker initiation does not actually correspond to stable propagation and the size of the specimens prevents stage II crack growth. The grain size for AA7075-T6 is approximately 70-110 μm in the cross section plane (W. S. Lee & Lin, 2016; Mohan et al., 2016), so each individual collection of parallel facets is likely the cleaved fracture surface of a single grain. Figure 4.12(c) shows both the structure of the parallel ridges under high magnification and an indent in the BCR. Some of the fracture surfaces have trails of these depressions which seem to be along the crack growth direction, but it is uncertain how these dimples are produced and why the voids seem to develop in paths. Successively higher magnification views near the

far edge of a typical BCR are shown in Figure 4.13 for the same specimen that failed at $2.6 \cdot 10^5$ cycles. These views show the BCR fracture surface as it transitions into the final rupture region. The facets still exhibit the characteristic parallel line features of the BCR that are in the general direction of crack growth.

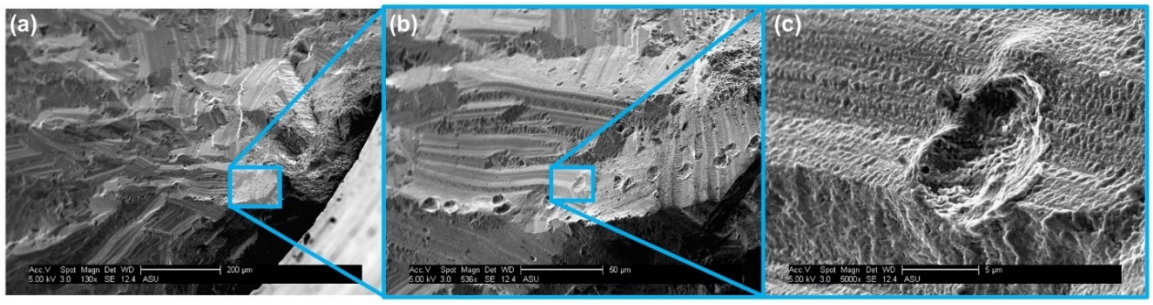

Figure 4.12. High Magnification Views of a Typical BCR for a Specimen Tested at 294 MPa With $2.6 \cdot 10^5$ Cycles of Life at Length Scales of (a) 200 µm, (b) 50 µm, and (c) 5 µm.

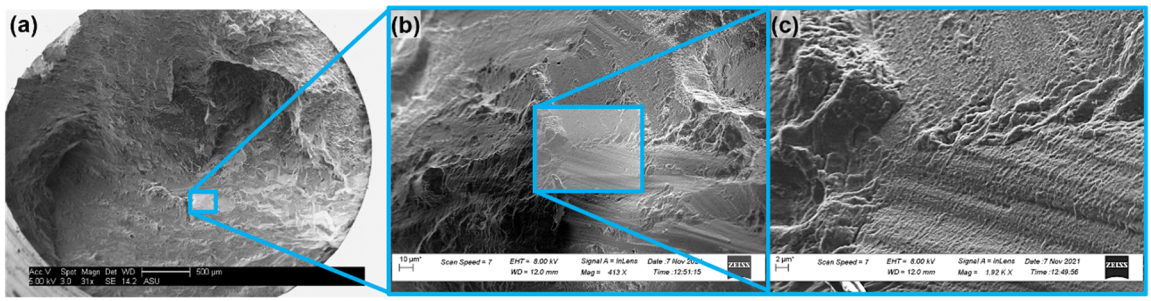

Figure 4.13 High Magnification Views of the Far End of a Typical BCR for a Specimen Tested at 294 MPa With $2.6 \cdot 10^5$ Cycles of Life at Length Scales of (a) 500 µm, (b) 10 µm, and (c) 2 µm.

Side views of the fracture surfaces for a range of specimens are shown in Figure 4.14, including high magnification views of regions near the crack initiation. These micrographs demonstrate the general profile of the different fracture features. The BCR is consistently steeply inclined at an angle slightly greater than 45 degrees, suggesting that BCR

propagation is driven by shear, while true cleavage is instead typically associated with fracture perpendicular to the applied stress. Shear lips are evident in the final rupture regions opposite the BCR. The high magnification views also give a more insightful view of the BCR's microstructure and highlight the elongated grain shape that results from the cold drawn manufacturing process based on the facet shapes in the BCR.

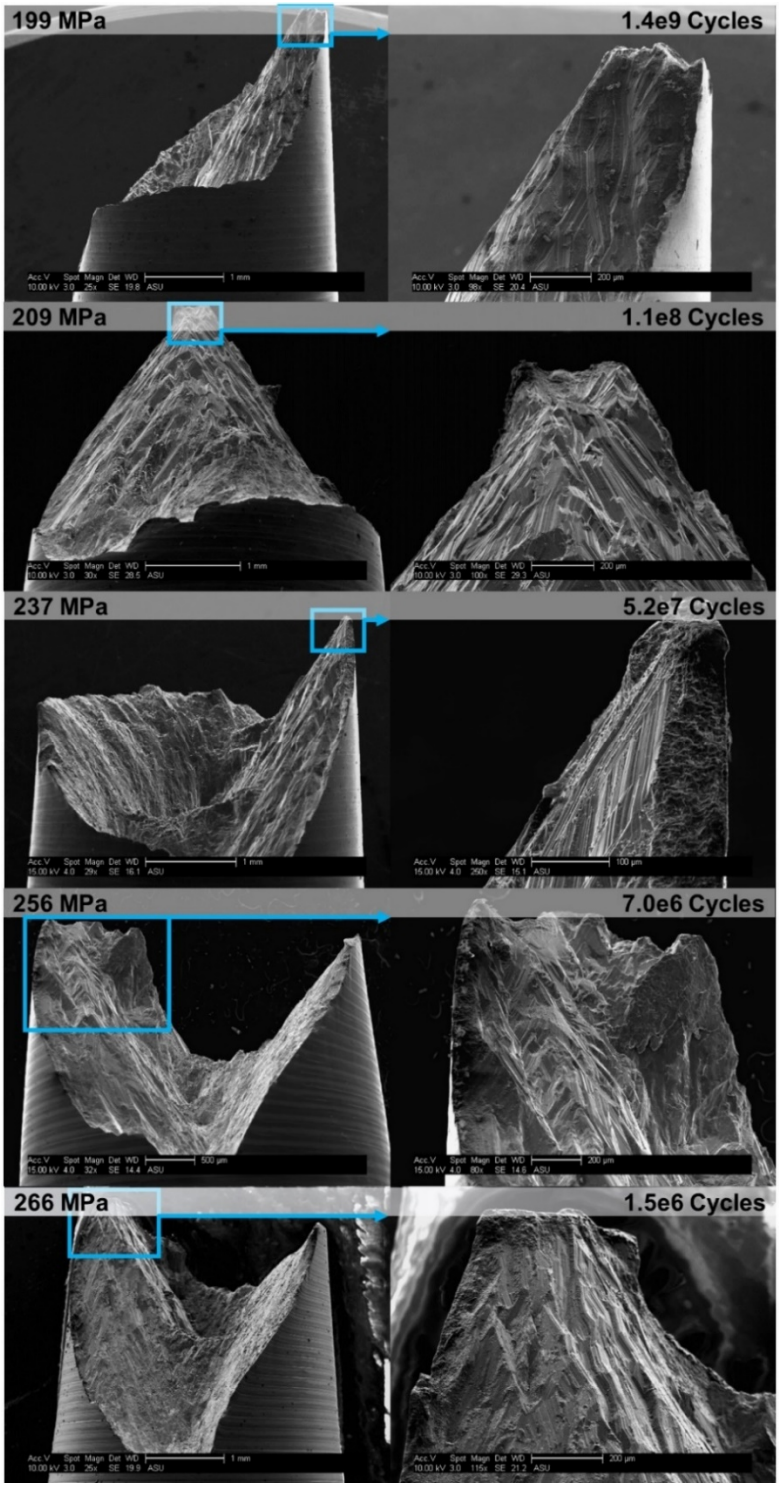

Figure 4.14. Full Profile Views of the Fracture Surface (Left) With Corresponding High Magnification Views of the Regions Near Crack Initiation (Right), Shown for Specimens Across a Range of Stress Amplitudes.

4.4.3. Micro-CT and Final Rupture Characteristics

Three-dimensional 3D models obtained via micro-CT scans of the internal crack geometry prior to complete failure and corresponding SEM micrographs of the overall fracture surface after complete failure are shown in Figure 4.15 for three different specimens with different loadings. Though it is not particularly obvious from these standard views, the micro-CT models emphasize how strictly horizontal the crack-initiation regions are. The top-down SEM views shown in Figure 4.15(a) match up with the top-down micro-CT crack surfaces shown in Figure 4.15(b). The regions absent from the micro-CT scan are highlighted in the SEM scans to mark areas that were last to fracture. The BCRs are not a part of any of these highlighted regions, confirming that although the cleavage-like features that define BCRs are similar to cleavage features that indicate sudden fracture, they are not last to fail.

Similarly, the side SEM views shown in Figure 4.15(c) are coordinated with the side-views of micro-CT crack models in Figure 4.15(d). In this case the final rupture region is behind the BRC for the 247 MPa specimen, and a shear lip is prominently shown on the right side for this sample. This indicates that in this case the shear lip was not the very last region to fracture, though it likely occurred right before the ultrasonic machine halted. Note that the crack initiation regions are out of view for the 199 and 237 MPa specimens in these images, and barely in view for the 247 MPa specimen. Finally, in Figure 4.15(e) SEM micrographs are presented from the final rupture regions, showing steep cliffs that are present in each sample and likely indicate the final split where the cracks on different planes connect.

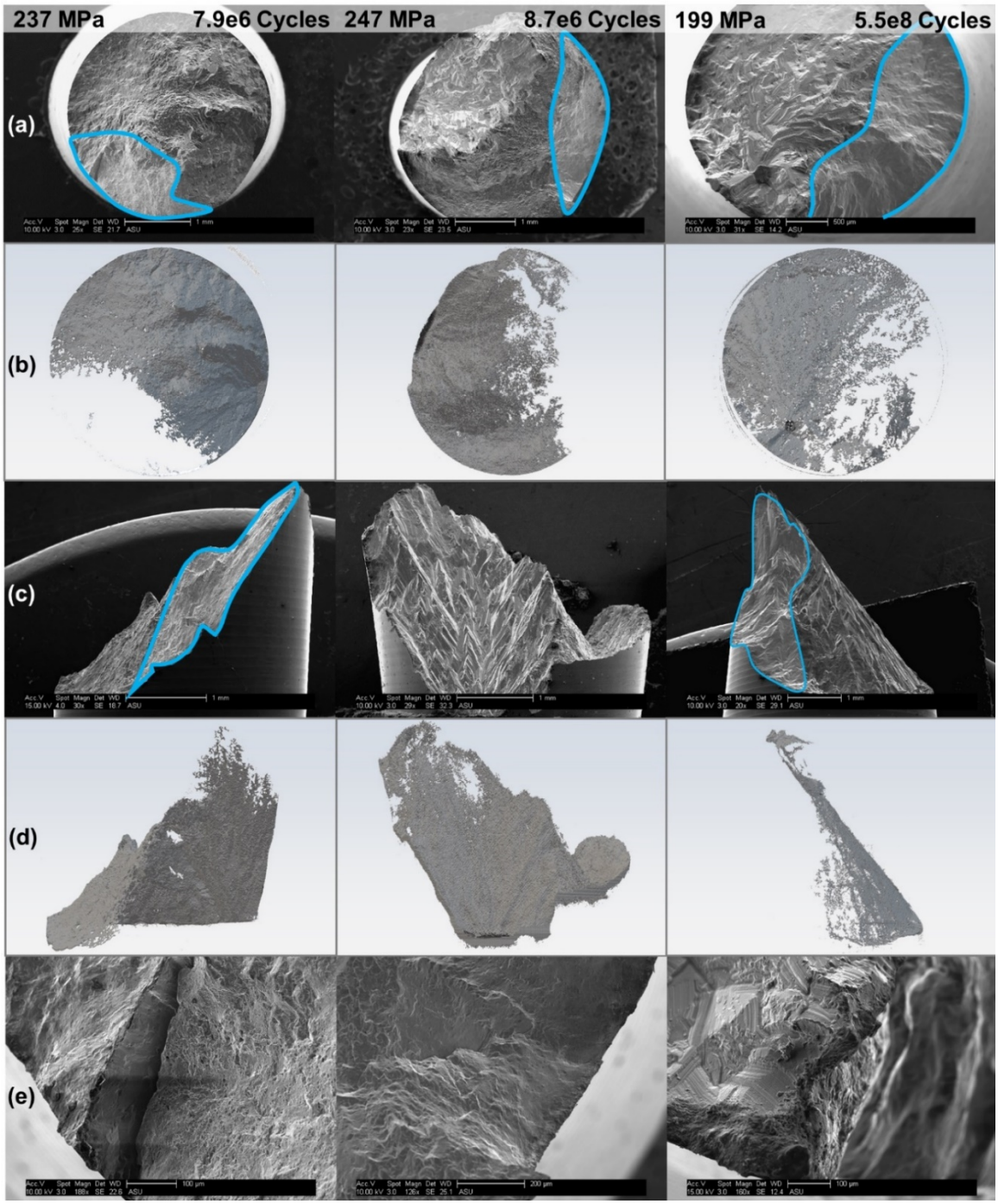

Figure 4.15. Three-Dimensional Models (a/c) Obtained by Micro-CT scans of the Internal Crack Structure Prior to Complete Failure Compared to Corresponding SEM Micrographs (c/d) of the Overall Fracture Surface After Complete Failure for three Different Specimens. The Highlighted Regions Mark Areas That Were Last to Fracture, and Characteristic Ridges Within These Regions are Shown in (e).

4.4.4. Surface Roughness

SEM micrographs of the fracture surfaces of five rough specimens over a range of loadings are shown in Figure 4.16. These images are noticebly different from micrographs of the baseline specimens in each of the views shown in Figure 4.10, Figure 4.11, and Figure 4.14. Literature for steel suggests that the likelihood of fractures initiating at the surface of a specimen decreases substantially after around 10^6 cycles, and the crack initiation for the baseline specimens in this study occur primarily subsurface for higher cycles counts, but these experiments prove that specimens can experience surface-initiated failures even after 10^{10} cycles as demonstrated by the 171 MPa specimen with the surface initiation region shown in Figure 4.16(c). The only rough specimen that underwent subsurface failure was the specimen loaded at 199 MPa, and this specimen had life nearly identical to that of the baseline specimen loaded at 199 MPa. Therefore, specimens with a rougher surface generally have a lower life because the roughness preempts crack initiation by increasing the probability of a crack initiating at the surface.

Unlike any of the baseline specimens, the rough specimen loaded to 285 MPa had two distinct surface initiation points – only one of them is shown in Figure 4.16(c). Furthermore, fracture surface of the 190 MPa specimen is highly tortuous and irregular, with no obvious initiation regions. BCRs seem to be interwoven with other features all throughout the surface shown in Figure 4.16(b) with an example higher magnification region in Figure 4.16(c). This unique topology is reflected in the profile of Figure 4.16(a), which flaunts a chaotic scatter of peaks and valleys. This suggests that the 190 MPa sample had many initiation points, which would help explain why it had the greatest difference in

life compared to the baseline specimens. Even in the samples that have only a single crack-initiation point, the propagation path seems to be heavily influenced by the surface roughness as shown by the jagged perimeters in the profile views, and the unusual appendage seen in the 209 MPa specimen in Figure 4.16(a). Therefore the surface condition has significant effects in not only crack initiation and life, but also crack propagation along the surface of the specimen.

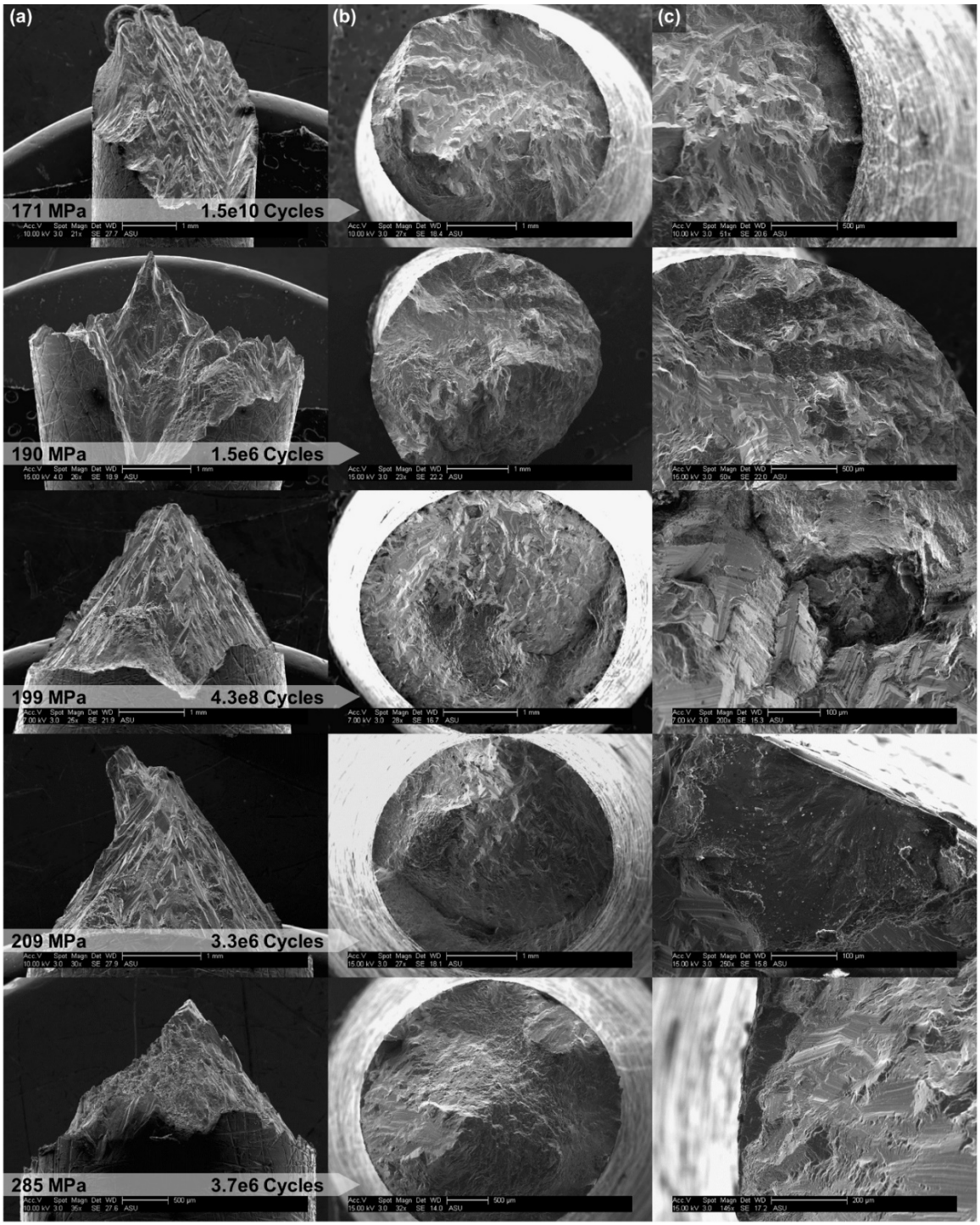

Figure 4.16. Micrographs of Five Rough Specimens Over a Range of Loadings With (a) Profile Views, (b) Low Magnification Top-Down Views, and (c) High Magnification Views of One of the Initiation Regions.

4.5. Summary

This chapter has presented a detailed ultrasonic fatigue study emphasizing variability and comprehensive SEM fractography has been presented for AA7075-T6 in fully reversed tension-compression ($R = -1$) loading using specimens with two different sizes and surface roughness conditions. Modal and harmonic probability-based analyses determined that the dominate source of variability in the resonant frequency and maximum stress amplitude is the variability of the dynamic modulus. The S-N curves stressed the prominence of size effects present in ultrasonic testing as well as the significant life-disparity between baseline and rough surface conditions. In contrast to some studies of crack initiation for aluminum alloys under fatigue, subsurface crack initiations were observed for specimens tested under low stress amplitudes. Nevertheless, tests on specimens with rough surface conditions showed increased tendency for surface-initiated cracks corresponding to degraded life, and it was demonstrated that cracks can initiate at the surface, even past 10^{10} cycles. SEM microscopy of fracture surfaces showed noteworthy fracture features, including bright, crystallographic regions (BCRs) even in the high cycle regime that seem to be unique to aluminum alloys studied under ultrasonic fatigue, indicating that the high frequency cycling influences the failure mechanisms.

CHAPTER 5.

MULTIPHYSICS OXIDATION OF CERAMIC MATRIX COMPOSITES[*]

5.1. Introduction

In this chapter, a multiphysics methodology and a corresponding numerical scheme is proposed for modeling the complex interactions between oxygen diffusion, matrix cracking, oxidation, and the state of stress in C/SiC CMCs at the microstructural scale. Various theoretical models have been proposed to model the oxidation of CMCs in service environments. Sullivan developed a model for the oxidation of C/SiC CMCs treating the composite specimens as a single-phase solid porous media and simulating the flow of ideal gases based on macroscopic mass conservation equations (Sullivan, 2005). The model successfully simulated the weight loss in time for thermogravimetric analysis (TGA) specimens for a range of specimens. However, because the model involves the homogenization of the entire material, it does not account for the complex variability in the inherent microstructure and the tortuous path of oxygen diffusion. In addition, the model does not involve any coupling to stress and is thus limited to pure oxidation experiments in its current state. Furthermore, the formulation does not capture the initial slow rate of carbon of carbon oxidation, which is likely associated with the initial development of porosity on the surface of the fibers (Ismail, 1991; Mall & Engesser, 2006). Other models account for stress effects or micromechanical features but still have limited

[*] This chapter is based on the author's submitted manuscript (Schichtel & Chattopadhyay, 2022).

connection to complex microstructural variations (Deng et al., 2021; Lamouroux et al., 1994; Mei et al., 2007; Parthasarathy et al., 2018; Sundararaghavan & Lee, 2010; Y. Xu et al., 2015; Y. Xu & Zhang, 2011). Zhao et al. modeled oxidation-damage coupling with oxygen diffusion through micro- and mesoscale architectures using conducted FEA simulations. However, the formulation is limited to the diffusion-controlled regime and lacks key considerations for heterogeneous diffusion, and the studies were limited to idealized geometries (Zhao et al., 2019).

In this work, these gaps in literature are addressed, and a multiphysics modeling methodology for the oxidation of C/SiC CMCs is presented that explicitly models oxygen diffusion through heterogeneous microstructures containing fibers and voids. The governing equations for equilibrium and conservation of mass are linked through reaction terms, oxygen diffusivities and solubilities, and matrix damage to address the complex two-way coupling between temperature, oxidation, diffusion, and the state of stress in CMCs. The developed model is implemented and tested using FEA simulations of various stressed and unstressed oxidation tests of stochastic heterogeneous representative microstructures to investigate the creep-like strain acceleration of stressed oxidation experiments and analyze the fundamental differences between the reaction-limited and diffusion-limited temperature regimes.

5.2. Multiphysics Oxidation Model

5.2.1. Notation

Boldface symbols and letters are used to signify vectors and matrices. Parenthetical subscripts denote that the value corresponds to a particular reductant or oxidant concentration, while parenthetical superscripts denote that the quantity corresponds to the value in a specified material type (e.g., $D_{(O_2)}^{(C)}$ is the diffusivity of the oxygen in carbon fibers). The stress, strain and stiffness tensors are reduced to matrix form such that stress and strain are vectorized and stiffness is a 6x6 matrix. Regarding the finite element method (FEM) implementation, superscript e's denote a vector containing all the nodal values for a particular finite element (e.g., $\boldsymbol{u}^e$ is a vector containing all the nodal displacements for an arbitrary element e).

5.2.2. Theoretical Formulation

The overall methodology for modeling the coupling of matrix cracking, oxygen diffusion, oxidation, and the state of stress in C/SiC CMCs starts from the basic governing equations for force equilibrium and conservation of mass for the oxygen and carbon. The load application and deformation are assumed to be slow, so inertial effects are ignored, and the equation for quasistatic equilibrium is the divergence of stress set to zero:

$$\boldsymbol{\nabla} \cdot \boldsymbol{\sigma} = \mathbf{0}. \tag{5.1}$$

Distinct constitutive laws are used for the SiC matrix, C fibers, and voids, which are each explicitly modeled. The initiation and propagation of microcracks in the matrix is

represented through damage, while the oxidation of the matrix material is ignored, which is reasonable for temperatures below 800°C (Zhao et al., 2019). In contrast, the fibers degrade through oxidation based on the remaining proportion of carbon. The constitutive behavior of the voids is an arbitrary low stiffness, and thus does not evolve. These mechanical constitutive equations are given as follows:

$$\boldsymbol{\sigma}^{(\mathrm{SiC})} = (1-d)\boldsymbol{C}_0^{(\mathrm{SiC})}\boldsymbol{\varepsilon} \tag{5.2a}$$

$$\boldsymbol{\sigma}^{(\mathrm{C})} = \phi_{(\mathrm{C})}\boldsymbol{C}_0^{(\mathrm{C})}\boldsymbol{\varepsilon} \tag{5.2b}$$

$$\boldsymbol{\sigma}^{(\mathrm{void})} = \boldsymbol{C}_0^{(\mathrm{void})}\boldsymbol{\varepsilon}, \tag{5.2c}$$

where d is a scalar damage variable, $\boldsymbol{C}_0$ are the initial elastic stiffness tensors, $\boldsymbol{\varepsilon}$ is the mechanical strain, and $\phi_{(\mathrm{C})}$ is the normalized concentration of carbon. Infinitesimal strain theory is assumed due to the high stiffness of the constituents. The normalized concentration is defined as $\phi = c/s$, where $c\left[\frac{\mathrm{mol}}{\mathrm{m}^3}\right]$ is the molar concentration and $s\left[\frac{\mathrm{mol}}{\mathrm{m}^3}\right]$ is the solubility or capacity in a given material with a given state, which for carbon is simply the starting concentration of carbon in a fiber and remains constant ($s_{(\mathrm{C})} = c_{0_{(\mathrm{C})}}$). Thus, for a pristine carbon fiber, the normalized concentration of carbon will be one, and the stiffness will just be the elastic stiffness tensor. Equation 5.2b postulates that as the carbon fiber oxidizes, the concentration of carbon within the fiber will decrease, corresponding to a proportionally decreased effective stiffness. The damage model could be any material appropriate model, but in this work, it is modeled using a simple exponential softening law with an equivalent strain based on the damage energy release rate. The equations can be found in (Patzák & Jirásek, 2001) and are not critical to the

methodology, so they are not included here. For ease of implementation the local version was used, but the nonlocal form would decrease size dependence and improve convergence for more complex systems.

In order to track the evolution of oxidants and reductants, the conservation of mass equations are employed:

$$\frac{dc_{(O_2)}}{dt} + \boldsymbol{\nabla} \cdot \boldsymbol{j}_{(O_2)} - \xi_{(O_2)} = 0 \tag{5.3a}$$

$$\frac{dc_{(C)}}{dt} - \xi_{(C)} = 0, \tag{5.3b}$$

where $\boldsymbol{j}\left[\frac{\text{mol}}{\text{m}^2\cdot\text{s}}\right]$ is the molar flux and $\xi\left[\frac{\text{mol}}{\text{m}^3\cdot\text{s}}\right]$ are the reaction rates. Note that the conservation of mass equation for carbon does not contain a flux term, so only oxygen is diffusive. The diffusion flux is defined using normalized-modified Fick's law:

$$\boldsymbol{j}_{(O_2)} = -s_{(O_2)} D_{(O_2)} \boldsymbol{\nabla} \phi_{(O_2)}, \tag{5.4}$$

where $D_{(O_2)}\left[\frac{\text{m}^2}{\text{s}}\right]$ is the effective oxygen diffusivity. In general, the diffusivity is a second-order tensor, but the diffusivity is taken to be isotropic, so only a scalar value is used for $D_{(O_2)}$. Although the diffusivity in individual elements is defined to be isotropic, the overall diffusivity of the system ends up being highly anisotropic due to the stochastic heterogeneity and evolving material properties. The oxygen solubility $s_{(O_2)}$ is the maximum amount of oxygen that can be stored in any given material at a certain time. Unlike for carbon, the capacity of oxygen in a particular material changes in time and space depending on the state of the material, so it cannot be factored out of the gradient of normalized concentration in Equation 5.4.

In general cases, the diffusive flux term of the conservation of mass equations is defined using the gradient of concentration rather than the gradient of normalized concentration; however, the physical driving force for diffusion is the gradient of chemical potential rather the gradient of concentration. In common diffusion problems, the gradient of the chemical potential happens to correspond to the gradient of concentration, but for the heterogeneous systems explored in this study this is not the case. For example, consider a system consisting of a block of metal in a room full of air. If the driving force of oxygen diffusion is defined merely as the gradient of concentration, then the oxygen in the system would reach equilibrium when the concentration of oxygen in the metal block is the same as the concentration of oxygen in the air. This is of course intuitively inaccurate because one would expect relatively little oxygen to be stored in the block of metal. Therefore, in this study we use the gradient of concentration relative to the total possible concentration, which is the normalized concentration, to approximate the gradient of the chemical potential as used in Equation 5.4. Thus, the system works to even out the normalized concentration across every material rather than evening out the actual concentration.

The conservation of mass equations are written in terms of absolute concentration since normalized concentration is not necessarily conserved, while the driving force for diffusion is taken as the gradient in normalized concentration rather than the gradient of absolute concentration. Hence the flux term in Equation 5.4 contains the additional solubility coefficient, which reconciles the units and causes the flux to reduce to the standard Fick's law for homogenous systems.

The reaction considered in this work is the oxidation of the carbon fiber, and although there are multiple possible reaction mechanisms, we will assume the following reaction for demonstrating the model:

$$\mathrm{C(s)} + \mathrm{O_2(g)} \rightarrow \mathrm{CO_2(g)}. \tag{5.5}$$

The effects of carbon dioxide production are ignored in this study, because pressure gradient-driven Darcy flow was determined to have little effect on CMC oxidation (Sullivan, 2005); however, it would be straightforward to consider these effects by adding an additional degree of freedom for normalized $\mathrm{CO_2}$ gas concentration. Because the reaction is a gas-solid reaction, the reaction rates in Equation 5.3 are only dependent on the concentration of the gas as expressed in the following equations:

$$\xi_{(\mathrm{O_2})} = -\frac{\lambda_{(\mathrm{O_2})}}{\lambda_{(\mathrm{C})}} R_{(\mathrm{C})} c_{(\mathrm{O_2})}^{n} \delta_{(\mathrm{C})} \tag{5.6a}$$

$$\xi_{(\mathrm{C})} = -R_{(\mathrm{C})} c_{(\mathrm{O_2})}^{n} \delta_{(\mathrm{C})}, \tag{5.6b}$$

where $\lambda_{(\mathrm{O_2})}\ \left[\mathrm{mol}_{(\mathrm{O_2})}\right]$ and $\lambda_{(\mathrm{C})}\ \left[\mathrm{mol}_{(\mathrm{O_2})}\right]$ are the stochiometric coefficients of oxygen and carbon in the chemical reaction equation, respectively, $R_{(\mathrm{C})}\ \left[\frac{\mathrm{mol}_{(\mathrm{C})} \cdot \mathrm{m}^{3(n-1)}}{\mathrm{mol}_{(\mathrm{O_2})}^{n} \cdot \mathrm{s}}\right]$ is the reaction rate coefficient for the oxidation of carbon, n is the order of the reaction, and $\delta_{(\mathrm{C})}$ is a Boolean that is one if carbon is present and zero otherwise. The stochiometric coefficients in this reaction are both equal to one, and based on literature TGA tests, the order of the reaction was determined to be one (Sullivan, 2005).

The local oxygen capacity and diffusivity are directly coupled to the state of damage in the matrix and the state of oxidation in the fibers. Following the basic principles of

porous media theory, oxygen gas is assumed to only be present in the pores and cracks of the matrix and the oxidized regions of the fibers, rather than within the physical solid matrix and fiber material. Thus, the solubility effectively relates to the local density of pores, cracks, and oxidation in the region, such that the capacity of oxygen in carbon fiber is a function of carbon concentration and the capacity of oxygen in the matrix is a function of damage. In this work, these relationships are assumed to be linear, ranging from a minimum value to a temperature-dependent maximum value:

$$s_{(O_2)}^{(C)} = -\left(s_{max_{(O_2)}} - s_{min_{(O_2)}}^{(C)}\right)\phi_{(C)} + s_{max_{(O_2)}} \tag{5.7a}$$

$$s_{(O_2)}^{(SiC)} = \left(s_{max_{(O_2)}} - s_{min_{(O_2)}}^{(SiC)}\right)d + s_{min_{(O_2)}}^{(SiC)} \tag{5.7b}$$

$$s_{(O_2)}^{(void)} = s_{max_{(O_2)}}, \tag{5.7c}$$

where $s_{min_{(O_2)}}$ are the minimum capacities of oxygen in the respective materials, and $s_{max_{(O_2)}}$ is the maximum oxygen solubility. The maximum solubility is the concentration of oxygen in air at the simulated temperature, while the minimum solubility is capacity of oxygen in the material in its original as-produced state at the simulated temperature due to manufacturing-induced microscopic flaws and defects. Ideally this baseline oxygen capacity could be determined experimentally and is likely temperature-dependent, but due to limited available data, the minimum values are assumed to be some percentage α of the maximum value:

$$s_{min_{(O_2)}}^{(C)} = \alpha_1 s_{max_{(O_2)}} \tag{5.8a}$$

$$s_{min_{(O_2)}}^{(SiC)} = \alpha_2 s_{max_{(O_2)}}. \tag{5.8b}$$

Equation 5.7a imposes the constraint that the amount of oxygen that can be stored in carbon fiber material elements in FEM implementation (discussed in Section 5.2.3) increases as the concentration of carbon decreases. Physically this represents oxygen being stored in the empty space left behind by oxidized carbon. Similarly, Equation 5.7b asserts that the amount of oxygen that can be stored in the matrix increases as damage in the matrix increases, which represents oxygen being stored in the cracks and voids of the damaged matrix. Equation 5.7c denotes that the capacity of oxygen in explicit voids is constant at the maximum value, since the voids are just empty space where gas can be readily stored.

The local oxygen diffusivities are comparably defined:

$$D_{(O_2)}^{(C)} = -\left(D_{max}{}_{(O_2)}^{(C)} - D_{min}{}_{(O_2)}^{(C)}\right)\phi_{(C)} + D_{max}{}_{(O_2)}^{(C)} \tag{5.9a}$$

$$D_{(O_2)}^{(SiC)} = \left(D_{max}{}_{(O_2)}^{(SiC)} - D_{min}{}_{(O_2)}^{(SiC)}\right)d + D_{min}{}_{(O_2)}^{(SiC)} \tag{5.9b}$$

$$D_{(O_2)}^{(void)} = D_{max}{}_{(O_2)}^{(void)}, \tag{5.9c}$$

where $D_{min_{(O_2)}}$ are the minimum diffusivities oxygen in the respective materials, and $D_{max_{(O_2)}}$ is the maximum oxygen diffusivity. Analogous to the reasoning for the oxygen solubilities, the local diffusivities increase in the material as the damage in the matrix increases and the fibers oxidize, since the cracks and empty spaces diminish barriers to the flow of oxygen. In porous media theory, the effective diffusivity is equal to the diffusion coefficient in a gas reduced by some function of the porosity, constrictivity, and tortuosity. There is very limited information in literature about these types of parameters whose values change with the state of the material, so the effects of these parameters are considered to

be effectively accounted for through the damage parameter or the state of oxidation based on Equation 5.9.

The temperature dependence of this model is incorporated through the temperature dependence of the oxidation reaction rate, oxygen capacity, and oxygen diffusivity. For each simulation the temperature is assumed to be constant throughout, and the exothermic heating of the reaction is not included so the effects of temperature gradients are not considered. In addition, the mismatch in thermal properties between the different constituents inherently causes residual stresses that effect oxidation rates through the opening and closure of cracks, but these effects are not included.

The temperature-dependence of the reaction rate coefficient $R_{(\mathrm{C})}$ is defined using the Arrhenius equation

$$R_{(\mathrm{C})} = \left(\frac{c_{0_{(\mathrm{C})}}}{s_{max_{(\mathrm{O}_2)}}}\right) k_0 \exp\left(-\frac{E_a}{R_g T}\right), \tag{5.10}$$

where k_0 $[\mathrm{s}^{-1}]$ is the preexponential coefficient, E_a $\left[\frac{\mathrm{J}}{\mathrm{mol}}\right]$ is the activation energy of the oxidation reaction, R_g $\left[\frac{\mathrm{J}}{\mathrm{K{\cdot}mol}}\right]$ is the universal gas constant, and T [K] is the absolute temperature. The maximum oxygen solubility $s_{max_{(\mathrm{O}_2)}}$, which is defined as the concentration of oxygen in air at temperature T, is calculated using the ideal gas law as follows:

$$s_{max_{(\mathrm{O}_2)}} = x_{(\mathrm{O}_2)} \frac{P}{R_g T} \tag{5.11}$$

where $x_{(O_2)}$ is the molar fraction of oxygen in air and P [Pa] is the ambient pressure. The concentration solubility quotient in Equation 5.10 serves to relate the TGA experiment used to calculate k_0 and E_a to the simulated oxygen conditions and carbon concentration.

The diffusivity of oxygen through air is calculated using the equation for the coefficient of diffusion in a binary mixture derived from the kinetic theory of gases (Hirschfelder, 1954; McAllister, 2014):

$$D_{12} = \frac{0.001858}{P\sigma_{12}^2\Omega_D}\sqrt{T^3\left(\frac{M_1 + M_2}{M_1 M_2}\right)}, \tag{5.12}$$

where D_{12} $\left[\frac{\text{cm}^2}{\text{s}}\right]$ is the diffusion coefficient of species 1 through species 2, P [atm] is the ambient pressure, σ_{12} [Å] is the average collision diameter, Ω_D is the collision integral, and M_1 and M_2 $\left[\frac{\text{g}}{\text{mol}}\right]$ are the molar masses of species 1 and species 2, respectively. Note the units given are the conventional units for this equation, so the diffusion coefficient is multiplied by 10^{-4} to convert the units to $\left[\frac{\text{m}^2}{\text{s}}\right]$ for use in other equations. The collision diameter can be calculated from the effective diameter of each species $\sigma_{12} = \frac{1}{2}(\sigma_1 + \sigma_2)$, and the collision integral is a function of $T\frac{k}{\epsilon_{12}}$, where k $\left[\frac{\text{J}}{\text{K}}\right]$ is the Boltzmann constant, and $\epsilon_{12} = \sqrt{\epsilon_1\epsilon_2}$ [J] is the force constant corresponding to the well depth potential energy. Thus, the collision integral depends on the temperature, so the values for Ω_D are interpolated from the corresponding tabulated values (Hirschfelder, 1954) for each simulation temperature. The cracks and pores are assumed to be large enough to ignore the effects of Knudsen diffusion, which would otherwise decrease the effective diffusivity.

In general, the maximum diffusivity of oxygen in the material is set to be equal to the diffusivity of oxygen through air since that would correspond to a completely oxidized or damaged material. However, because the oxidation of the fiber is a surface phenomenon and the model is based on volumetric domains, the maximum diffusivity of oxygen in the fiber is limited depending on the reaction rate to limit the flow of oxygen to the center of the fiber:

$$D_{max}{}^{(\mathrm{C})}_{(\mathrm{O_2})} = \begin{cases} \alpha_3 R_{(\mathrm{C})} & if\ \phi_{(\mathrm{C})} \geq \alpha_4 \\ D_{12} & if\ \phi_{(\mathrm{C})} < \alpha_4 \end{cases} \tag{5.13a}$$

$$D_{max}{}^{(\mathrm{SiC})}_{(\mathrm{O_2})} = D_{12}. \tag{5.13b}$$

This asserts that the diffusivity of oxygen through the carbon fibers is set as a percentage α_3 of the reaction rate unless the normalized concentration falls below some percentage α_4. This condition is included as an indirect way to prevent the centers of the fibers from oxidizing before the outsides have been completely oxidized in the reaction-limited oxidation regimes. Thus, the purpose of this condition is to mimic the surface-nature of the reaction despite the reaction being defined the basis of volumes. The parameters α_3 and α_4 influence the relative thickness of the oxidation front, which is difficult to define because the surface of the oxidizing fiber is not completely smooth (Lamouroux et al., 1993), and they could be functions of the characteristic length to limit size dependence.

The diffusivity of oxygen in air ranges from approximately $1.8 \cdot 10^{-5}$ to $3.1 \cdot 10^{-4}$ $\left[\frac{\mathrm{m}^2}{\mathrm{s}}\right]$ in the temperature range from 0°C to 1200°C, while the diffusivity of oxygen through pristine silica matrix maxes out at around $2.8 \cdot 10^{-12}$ $\left[\frac{\mathrm{m}^2}{\mathrm{s}}\right]$ (Deal & Grove, 1965).

Hence, even with only a small amount of damage in the material, the diffusion of oxygen through the pristine bulk matrix is likely negligible in comparison to the diffusion through the cracks. The manufacturing methods for CMCs inherently produce significant damage in the matrix, so the minimum diffusivity is set to some percentage of the maximum diffusivity, similar to what was done in Equation 5.8 for the solubility:

$$D_{min}{}^{(\mathrm{C})}_{(\mathrm{O_2})} = \alpha_1 D_{max}{}^{(\mathrm{C})}_{(\mathrm{O_2})} \tag{5.14a}$$

$$D_{min}{}^{(\mathrm{SiC})}_{(\mathrm{O_2})} = \alpha_2 D_{max}{}^{(\mathrm{SiC})}_{(\mathrm{O_2})}. \tag{5.14b}$$

This effectively acknowledges the existence of some initial damage in the material, and in accordance with the theory for effective diffusivity in porous media, the diffusivity is defined using theory for diffusion through gases rather than diffusion through solids because the bulk of the oxygen diffusion is assumed to occur through the cracks and pores in the material rather than directly through the pristine bulk material.

Overall, the model can be used to solve for the primary unknowns, which are displacements and normalized concentrations, based on the governing equations given in Equation 5.1 and Equation 5.3. Using the normalized concentration as the primary degrees of freedom rather than the absolute concentration is beneficial because the normalized concentration can be continuous across heterogeneous media while the concentration is discontinuous. This has a similar effect to the approach for mass diffusion through porous media taken by Sullivan et al., which uses the partial pressures within pore volume as the continuous solution variable, while the porosity is discontinuous (Sullivan, 2005), except in this case the solubilities are variable. The approach taken in this work for diffusion is

consistent with the formulation for mass diffusion in Abaqus, a commercial FEA software (Smith, 2009).

5.2.3. Numerical Implementation

The methodology is implemented numerically using the FEM via Abaqus. Because the model solves for multiple concentration-related degrees of freedom in addition to the displacements, standard built-in elements cannot be used, since they are limited to only a single pore pressure or normalized concentration degree of freedom. Therefore, the implementation of this model in Abaqus requires the usage of a user-defined element (UEL) subroutine, which is a custom finite element. Every node is defined to have a total of five degrees of freedom consisting of three displacement components $\boldsymbol{u}$, the normalized concentration of the oxidant oxygen $\phi_{(\mathrm{O}_2)}$, and the normalized concentration of the reactant carbon $\phi_{(\mathrm{C})}$. Note that the normalized concentration is defined consistently with Abaqus documentation for mass diffusion, but within the documentation it is also often confusingly interchanged with chemical activity, which in the context of chemistry actually refers to a different quantity. The Galerkin method of weight residuals was used to derive the weak forms of Equations 5.1 and 5.3 with natural boundary conditions, which were then discretized and reduced to the elemental finite element form:

$$\boldsymbol{F}_{\boldsymbol{u}}^{e} = \int_{\Omega^e} (\boldsymbol{B}^{\mathrm{T}} \boldsymbol{\sigma}^{e}) d\Omega^{e} - \int_{\Gamma^e} (\mathbb{N}^{\mathrm{T}} \bar{\boldsymbol{t}})\, d\Gamma^{e} \tag{5.15a}$$

$$\boldsymbol{F}^{e}_{\phi_{(\mathrm{O}_2)}} = \int_{\Omega^e} \begin{pmatrix} \boldsymbol{N}^{\mathrm{T}}\boldsymbol{N}\boldsymbol{\phi}^{e}_{(\mathrm{O}_2)} \dfrac{ds_{(\mathrm{O}_2)}}{dt} \\ +\boldsymbol{N}^{\mathrm{T}}\boldsymbol{N}s_{(\mathrm{O}_2)} \dfrac{d\boldsymbol{\phi}^{e}_{(\mathrm{O}_2)}}{dt} \\ +(\boldsymbol{\nabla N})^{\mathrm{T}}(\boldsymbol{\nabla N})\boldsymbol{\phi}^{e}_{(\mathrm{O}_2)} s_{(\mathrm{O}_2)} D_{(\mathrm{O}_2)} \\ +\boldsymbol{N}^{\mathrm{T}}\left(\dfrac{\lambda_{(\mathrm{O}_2)}}{\lambda_{(\mathrm{C})}} R_{(\mathrm{C})} s_{(\mathrm{O}_2)} \boldsymbol{N}\boldsymbol{\phi}^{e}_{(\mathrm{O}_2)} \delta_{(\mathrm{C})}\right) \end{pmatrix} d\Omega^e + \int_{\Gamma^e} \boldsymbol{N}^{\mathrm{T}} \bar{J}_{(\mathrm{O}_2)} \, d\Gamma^e \qquad (5.15\mathrm{b})$$

$$\boldsymbol{F}^{e}_{\phi_{(\mathrm{C})}} = \int_{\Omega^e} \left(\boldsymbol{N}^{\mathrm{T}}\boldsymbol{N}s_{(\mathrm{C})} \frac{d\boldsymbol{\phi}^{e}_{(\mathrm{C})}}{dt} + \boldsymbol{N}^{\mathrm{T}} R_{(\mathrm{C})} s_{(\mathrm{O}_2)} \boldsymbol{N}\boldsymbol{\phi}^{e}_{(\mathrm{O}_2)} \delta_{(\mathrm{C})} \right) d\Omega^e \, . \qquad (5.15\mathrm{c})$$

where $\boldsymbol{F_u}$ is the residual force corresponding to the equilibrium equations, $\boldsymbol{F}_{\phi_{(\mathrm{O}_2)}}$ is the residual force corresponding to the conservation of mass equation for oxygen, $\boldsymbol{F}_{\phi_{(\mathrm{C})}}$ is the residual force corresponding to the conservation of mass equation for carbon, Ω designates the domain volume, Γ is the natural boundary of the domain volume, $\boldsymbol{B}$ is the symmetric discrete gradient matrix, $\boldsymbol{N}$ is the set of shape functions for isoparametric elements, ℕ is the shape function matrix scattered for three displacement degrees of freedom, $\bar{\boldsymbol{t}}$ are the prescribed tractions on the natural boundary, and $\bar{\boldsymbol{J}}_{(\mathrm{O}_2)}$ are the prescribed oxygen fluxes on the natural boundary. Note that the second term in the volume integral of Equation 5.15b results from substituting the normalized concentration in Equation 5.3a and applying the product rule for the time derivative considering that $s_{(\mathrm{O}_2)}$ can change in time. This term is required for mass to be conserved, but a comparable term is not needed in Equation 5.15c because $s_{(\mathrm{C})}$ is constant. The derivation of these equations is shown in Appendix A. The integration over the element domain is achieved numerically through Gaussian quadrature for fully integrated linear elements.

Implicit time integration is achieved in Abaqus/Standard, which uses the Newton-Raphson method to obtain solutions for nonlinear problems combining incremental and iterative procedures. The non-linear differential equations are linearized within each timestep such that quantities such as diffusivity and solubility are considered constant within a timestep but updated with every iteration. For each iteration, Abaqus solves for the nodal unknowns from the overall stiffness matrix and force vector which are scattered from the user-defined elemental stiffness matrices and force vectors calculated based on the values of the solution and state variables from the previous timestep. Therefore, the local elemental governing equations in Equation 5.15 are converted to the following matrix form:

$$\begin{bmatrix} \boldsymbol{F}_{\boldsymbol{u}}^{e} \\ \boldsymbol{F}_{\phi_{(\mathrm{O}_2)}}^{e} \\ \boldsymbol{F}_{\phi_{(\mathrm{C})}}^{e} \end{bmatrix} = -\begin{bmatrix} \boldsymbol{K}_{\boldsymbol{uu}}^{e} & \boldsymbol{K}_{\boldsymbol{u}\phi_{(\mathrm{O}_2)}}^{e} & \boldsymbol{K}_{\boldsymbol{u}\phi_{(\mathrm{C})}}^{e} \\ \boldsymbol{K}_{\phi_{(\mathrm{O}_2)}\boldsymbol{u}}^{e} & \boldsymbol{K}_{\phi_{(\mathrm{O}_2)}\phi_{(\mathrm{O}_2)}}^{e} & \boldsymbol{K}_{\phi_{(\mathrm{O}_2)}\phi_{(\mathrm{C})}}^{e} \\ \boldsymbol{K}_{\phi_{(\mathrm{C})}\boldsymbol{u}}^{e} & \boldsymbol{K}_{\phi_{(\mathrm{C})}\phi_{(\mathrm{O}_2)}}^{e} & \boldsymbol{K}_{\phi_{(\mathrm{C})}\phi_{(\mathrm{C})}}^{e} \end{bmatrix} \begin{bmatrix} d\boldsymbol{u}^{e} \\ d\boldsymbol{\phi}_{(\mathrm{O}_2)}^{e} \\ d\boldsymbol{\phi}_{(\mathrm{C})}^{e} \end{bmatrix}, \tag{5.16}$$

where the $\boldsymbol{K}^{e}$ matrices are the element contributions to the Jacobian matrix as defined below:

$$\boldsymbol{K}_{\boldsymbol{NM}}^{e} = -\frac{d\boldsymbol{F}_{\boldsymbol{N}}^{e}}{d\boldsymbol{u}_{\boldsymbol{M}}^{e}}, \tag{5.17}$$

where $\boldsymbol{F}_{\boldsymbol{N}}^{e}$ are the nodal residuals at degree freedom $\boldsymbol{N}$, and $\boldsymbol{u}_{\boldsymbol{M}}^{e}$ are the nodal solution-dependent variables for degree of freedom $\boldsymbol{M}$. Abaqus uses the backward-Euler scheme for time integration scheme and automatic convergence checks are applied to the residuals. Because the solution is time dependent, the Jacobian matrix includes contributions from the element tangent stiffness and capacitance matrices such that

$$\boldsymbol{K}_{\boldsymbol{NM}}^{\boldsymbol{e}} = \boldsymbol{A}_{\boldsymbol{KN}}^{\boldsymbol{e}} + \boldsymbol{C}_{\boldsymbol{NM}}^{\boldsymbol{e}} \frac{1}{\Delta t}, \tag{5.18}$$

where $\boldsymbol{A}_{\boldsymbol{KN}}^{\boldsymbol{e}}$ is the elemental stiffness matrix and $\boldsymbol{C}_{\boldsymbol{NM}}^{\boldsymbol{e}}$ is the elemental capacitance matrix, which is diagonalized for linear elements to reduce spurious oscillations that occur for low diffusivities and Péclet numbers. Furthermore, because the Jacobian is a total derivative, it includes both the direct and indirect dependencies of $\boldsymbol{u}_{\boldsymbol{M}}^{\boldsymbol{e}}$ on $\boldsymbol{F}_{\boldsymbol{N}}^{\boldsymbol{e}}$. Therefore, state variables such as damage, diffusivity, and solubility that generally depend on the solution-dependent variables are included in the definition of the Jacobian:

$$\frac{d\boldsymbol{F}_{\boldsymbol{N}}^{\boldsymbol{e}}}{d\boldsymbol{u}_{\boldsymbol{M}}^{\boldsymbol{e}}} = \frac{\partial \boldsymbol{F}_{\boldsymbol{N}}^{\boldsymbol{e}}}{\partial \boldsymbol{u}_{\boldsymbol{M}}^{\boldsymbol{e}}} + \frac{\partial \boldsymbol{F}_{\boldsymbol{N}}^{\boldsymbol{e}}}{\partial \boldsymbol{H}_{\boldsymbol{Q}}^{\boldsymbol{e}}} \frac{d\boldsymbol{H}_{\boldsymbol{Q}}^{\boldsymbol{e}}}{d\boldsymbol{u}_{\boldsymbol{M}}^{\boldsymbol{e}}}, \tag{5.19}$$

where $\boldsymbol{H}_{\boldsymbol{Q}}^{\boldsymbol{e}}$ is the set of solution-dependent state variables. The complete definition of the Jacobian with these additional terms is not strictly necessary for the accuracy of the solution because the Jacobian aides the rate of convergence while the residual dictates accuracy. However, the model is highly coupled and nonlinear, so these terms have been computed to improve convergence.

5.3. Simulation Setup

5.3.1. Stochastic Representative Microstructures

A recently developed three-dimensional stochastic representative volume element (SRVE) generation algorithm was utilized to test the model on realistic microstructures (Khafagy, Datta, et al., 2021). The model accounts for the variability of various architectural parameters including fiber size and distribution, as well voids, which tend to

develop around fibers as shown in Figure 5.1(a). The SRVEs consist of three types of material elements: carbon fiber, voids, and SiC matrix, and the simulations in this study utilize an 80x80x20 element SRVE with 12 randomly distributed fibers with a mean fiber radius of 2.5 μm and standard deviation of 0.15 μm, and a 49% volume fraction and 3% intratow porosity based on characterization studies (Khafagy, Datta, et al., 2021). The fiber and void distributions are shown in Figure 5.1(b).

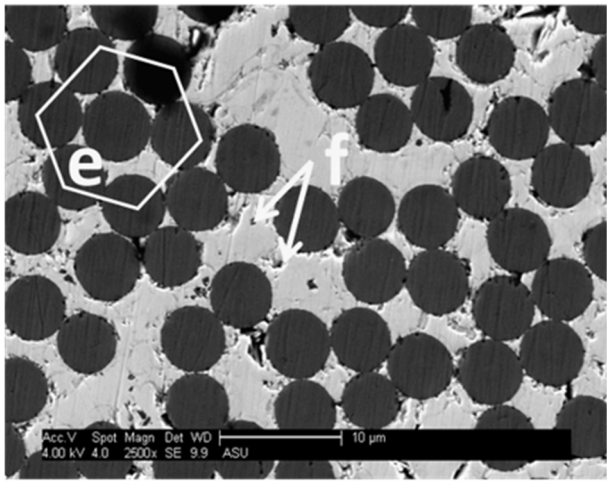

(a)

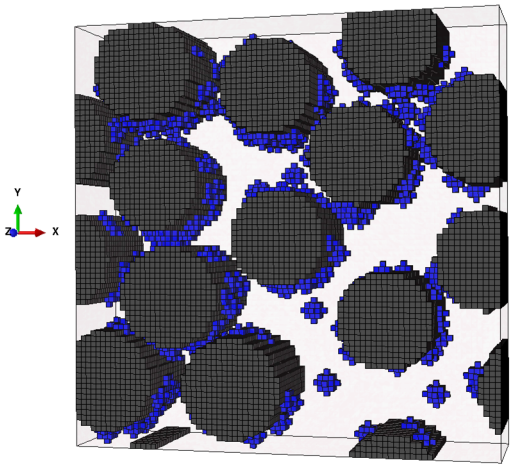

(b)

Figure 5.1. (a) Micrographs of a C/SiNC CMC Sample Cross Section Showing the Distribution of Fibers and Voids (Khafagy, Datta, et al., 2021), and (b) Representative Microstructure With Uniform Structural Mesh Showing Carbon Fiber Elements in Black and Void Elements in Blue.

The representative microstructure shown in Figure 5.1(b) utilizes a uniform structural mesh with linear, fully integrated hexahedral elements. The uniform structural mesh is employed because nonstructural mesh would increase the number of elements required to accurately represent voids and it simplifies the implementation of periodic boundary conditions. The local damage model and structural mesh cause size dependence; future

studies could include a nonlocal damage model with nonstructural mesh, but this is not the focus of this study.

The carbon fibers start with an initial normalized carbon concentration of unity, while the voids and SiC matrix are set to a normalized carbon concentration of zero. The material parameters for transversely orthotropic T-300 carbon fiber used to define the initial elastic stiffness tensor are taken from literature as shown in Table 5.1 where E_1 is the longitudinal Young's modulus, E_2 is the transverse modulus, G_{12} is the axial shear modulus, G_{23} is the transverse shear modulus, ν_{12} is the major Poisson's ratio, and ρ_0 is the initial carbon fiber density from which the initial molar carbon concentration $c_{0_{(C)}}$ is computed. The isotropic mechanical properties for the CVI SiC are given in Table 5.2, where E is the Young's modulus, ν is the Poisson's ratio, and σ_d is the damage strength. The void elements were assigned negligible stiffness because they should not carry any load.

Table 5.1. T-300 Carbon Fiber Properties (Daniel & Ishai, 2006).

E_1 (GPa)	E_2 (GPa)	G_{12} (GPa)	G_{23} (GPa)	ν_{12}	$\rho_0 \left(\frac{\text{kg}}{\text{m}^3}\right)$	$c_0 \left(\frac{\text{mol}}{\text{m}^3}\right)$
230	15	27	7	0.2	1760	$1.47 \cdot 10^5$

Table 5.2. SiC Matrix (CVI) Properties (K. Liu et al., 2011).

E (GPa)	ν	σ_d(MPa)
420	0.2	180

The diffusion parameters used to compute D_{12} in Equation 5.12 are provided in Table 5.3 where subscript 1 corresponds to O_2 and subscript 2 corresponds to air. The collision integral depends on the temperature, so the values for Ω_D are linearly interpolated from the

corresponding tabulated values for depending on the simulation temperature (Hirschfelder, 1954). The oxidation parameters for the temperature-dependent reaction rates and first order reaction coefficients are given in Table 5.4.

Table 5.3. Diffusion Parameters for Oxygen in Air (*Engineering Toolbox*, 2009; Hirschfelder, 1954).

σ_1 (Å)	σ_2 (Å)	$M_1 \left(\frac{\mathrm{g}}{\mathrm{mol}}\right)$	$M_2 \left(\frac{\mathrm{g}}{\mathrm{mol}}\right)$	ϵ_1/k (K)	ϵ_2/k(K)
3.46	3.62	31.99	28.96	118	102

Table 5.4. Oxidation Reaction Parameters (Sullivan, 2005).

$R_g \left(\frac{\mathrm{J}}{\mathrm{mol}\cdot\mathrm{K}}\right)$	$\lambda_{(\mathrm{O}_2)}$	$\lambda_{(\mathrm{C})}$	n	k_0 (s^{-1})	$\mathrm{E_a}\left(\frac{\mathrm{kJ}}{\mathrm{mol}}\right)$
8.314	1	1	1	6452.35	118.3

The alpha parameters from Equations 5.8, 5.14, and 5.13 are shown in Table 5.5. The values for α_1 and α_2 were set at 1e-2 corresponding to an initial continuum defect volume fraction of 1%, and the values for α_3 and α_4 were chosen such that the reactions occur near the surface of the fibers rather than throughout the entire fiber in the reaction-limited regime. Lower values decrease the width of the fiber oxidation front, but also slow fiber recession.

Table 5.5. Alpha Parameters.

α_1	α_2	α_3	α_4
1e-2	1e-2	1e-4	5e-2

Bidirectional periodic boundary conditions were implemented using a formulation adapted from the strategy described by Bednarcyk et al. for three-dimension periodic boundary conditions to two directions (Bednarcyk et al., 2014). Periodicity in the y and z-directions were included to reduce boundary effects in the system while periodicity in the x-direction was not included so that oxygen would be allowed to diffuse along the x-direction. Equation constraints were imposed on the degrees of freedom for each node at the face, edge, and corners to match them to their corresponding opposing faces, edges and corners and a single reference node for both the y and z-directions. The node at the origin was fixed to eliminate rigid body motion of the SRVE. The reference nodes were set up to allow the average stress to be controlled on both of the periodic boundaries and enable Poisson's strain.

5.3.2. Stressed Oxidation Simulations

In order to analyze the effects of coupled effects of stress and oxidation, stressed oxidation test simulations are conducted on the SRVEs. Similar to the stressed oxidation experiments of C/SiC coupons in air performed by Halbig et al. (Halbig et al., 2008), the stress in the SRVEs were ramped to 80 MPa in the axial direction over a period of 10 seconds and then held constant. The stress values were chosen such that a small amount of damage initiates in the matrix after the initial loading. Over the course of the simulation, the oxidation of the fibers causes the strain in the overall specimen to evolve as the stress redistributes from the oxidizable fibers to the matrix. In each individual simulation the temperature is kept constant, and the pressure is set to atmospheric pressure. A boundary

condition is set to enforce the normalized concentration of oxygen to be unity on the x-positive nonperiodic face of the SRVE or on a 3x3 element void region added adjacent to a fiber. The boundary condition of oxygen on the entire x-positive face emulates a condition where that surface is exposed to air, while the boundary condition of a small region on the surface represents a condition where there is an exposed crack in an EBC that is approximately 0.8 µm wide (Opila & Serra, 2007). These boundary and load conditions are shown in Figure 5.2.

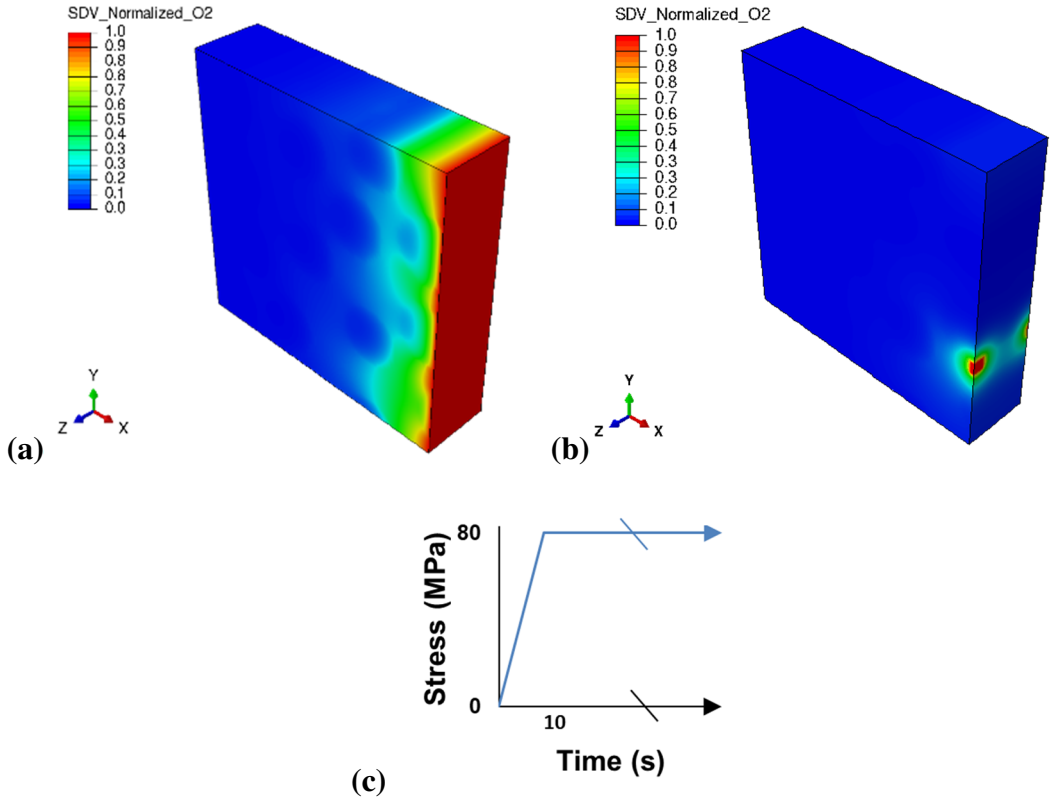

Figure 5.2. Boundary Conditions for Normalized Concentration of Oxygen on (a) the X-Positive Face or (b) a Simulated Exposed Crack, and (b) the Load Conditions for the Stressed Oxidation Tests.

5.4. Results and Discussion

Quantitative validation for CMC stressed oxidation models is challenging due to the limited availability of data in literature caused by the high expense of the material, and the proprietary protection for public and academic release, so the model was first validated against TGA experiments without applying load. Oxidation simulations were performed on the same SRVE geometry in an unstressed condition, and the resulting mass loss curves are compared to the TGA experiments conducted by Halbig et al. in Figure 5.3. The model is shown to accurately capture the trends in weight loss curves at lower temperatures, including the initial slow rate of oxidation due to pore formation in the fiber surface due to the evolving solubility. It is important to note that this behavior is not captured in most oxidation models but is captured directly through the physics in this model, and although it is difficult to see in the plots, this behavior is also present at high temperatures.

The model predicts faster oxidation than the experiments due to the difference in scales of the simulation and the TGA experiments, but this difference has an increasingly reduced impact at lower temperatures because the oxidation is primarily reaction-controlled in that regime. The decreasing rate of oxidation that happens over 700°C is not captured because the model does not account for the formation of silica in the material that acts as a barrier to oxygen ingress, but in the absence of passive matrix oxidation, the rate of fiber consumption would indeed continue to increase with increasing temperature as shown in TGA experiments of carbon fiber strands (Halbig et al., 2008). At temperatures strictly in the reaction-controlled regime below temperatures with matrix oxidation, the model captures the trends better than Sullivan's model even without calibration.

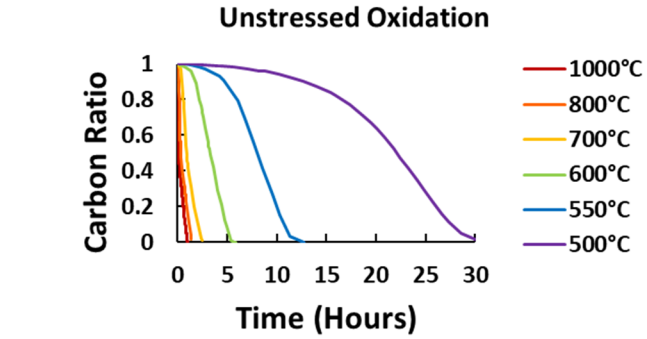

(a)

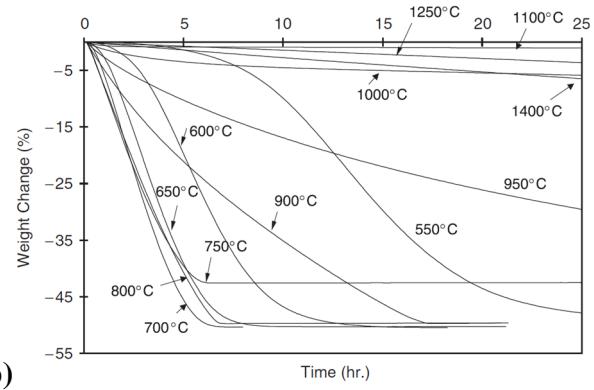

(b)

Figure 5.3. Carbon Mass Loss for (a) Unstressed Oxidation Simulations, and (b) TGA Experiments Performed on Unstressed C/SiC Composite Weave Samples, Reproduced With Permission From the Author (Halbig et al., 2008).

The SRVE was then tested across a range of temperatures with the stress applied in the axial direction. The resultant strain evolution curves are shown in Figure 5.4(a), and stressed oxidation experiments performed by Halbig et al. are shown in Figure 5.4(b). Note that quantitative comparison of the simulation results with experiments is not possible because those tests were performed on macroscale C/SiC composite weaves architectures, while the simulations were performed on a microscale portion of a unidirectional tow. Nevertheless, the model successfully captures the creep-like strain evolution curves by accounting for the physics of evolving diffusivities and solubilities, and the time to failure

is consistently shorter for higher temperatures. The strain evolutions for lower temperatures follows a similar trend to those at higher temperatures, but they take significantly more time, so the plots were truncated at 70 minutes. It should be noted that the silica formation has a less drastic impact on the oxidation during stressed oxidation tests because the tensile stress opens cracks that would otherwise be blocked by the silica barrier. The discrepancy of time from the experimental values can be largely attributed to the scale discrepancy and surface area to volume ratio differences, and the strain disparity can be largely attributed to the architectural differences of plain weave vs. uniaxial intratow.

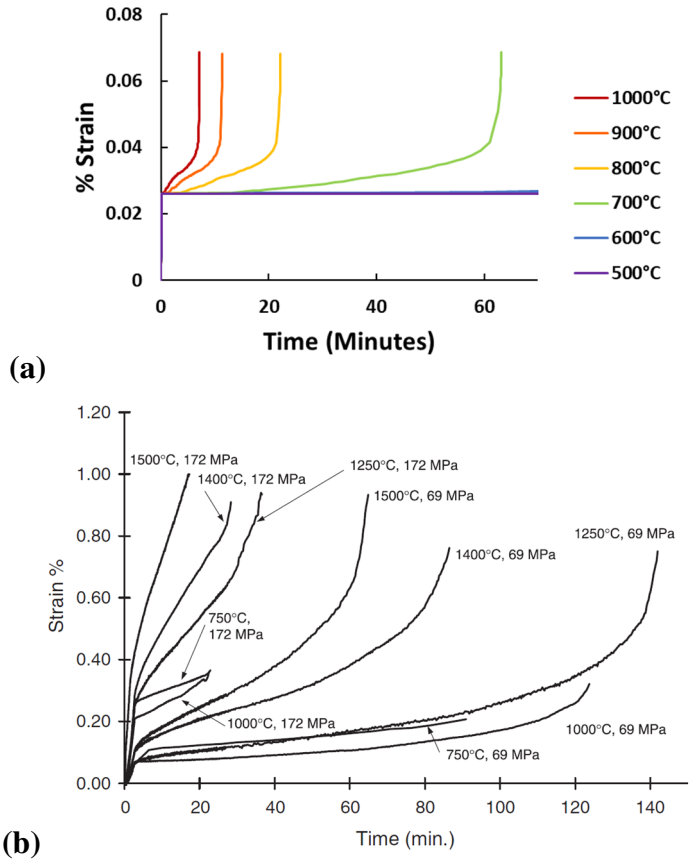

Figure 5.4. (a) Strain Evolution Curves For Stressed Oxidation Tests in Fiber Direction, and (b) Strain Evolution Curves From C/SiC Plain Weave Composite Experiments, Reproduced With Permission From the Author (Halbig et al., 2008).

The carbon mass loss curves for stressed and unstressed conditions are compared for select temperatures in Figure 5.5. The carbon weight loss during a stressed oxidation cannot be easily measured experimentally, but the simulation trends from the model provide important insights into the distinctions between stressed and unstressed oxidation. The unstressed systems took approximately 1.5 times longer to fully oxidize at 500°C, whereas they took almost seven times longer at 1000°C, demonstrating that the stress affects the rate of oxidation more strongly at higher temperatures. Stressed conditions increase the amount and opening of microcracks in the matrix which thereby increases the diffusivity. Thus, the oxidation in the diffusion-limited regime is more greatly impacted by stress than those in the reaction-limited regime. This effect would be even more prominent in the presence of passive matrix oxidation. Furthermore, the comparison at 800°C and 1000°C shows how the carbon loss accelerates in time due to the damage coupling for stressed oxidation tests, while the unstressed samples settle into a constant rate of oxidation.

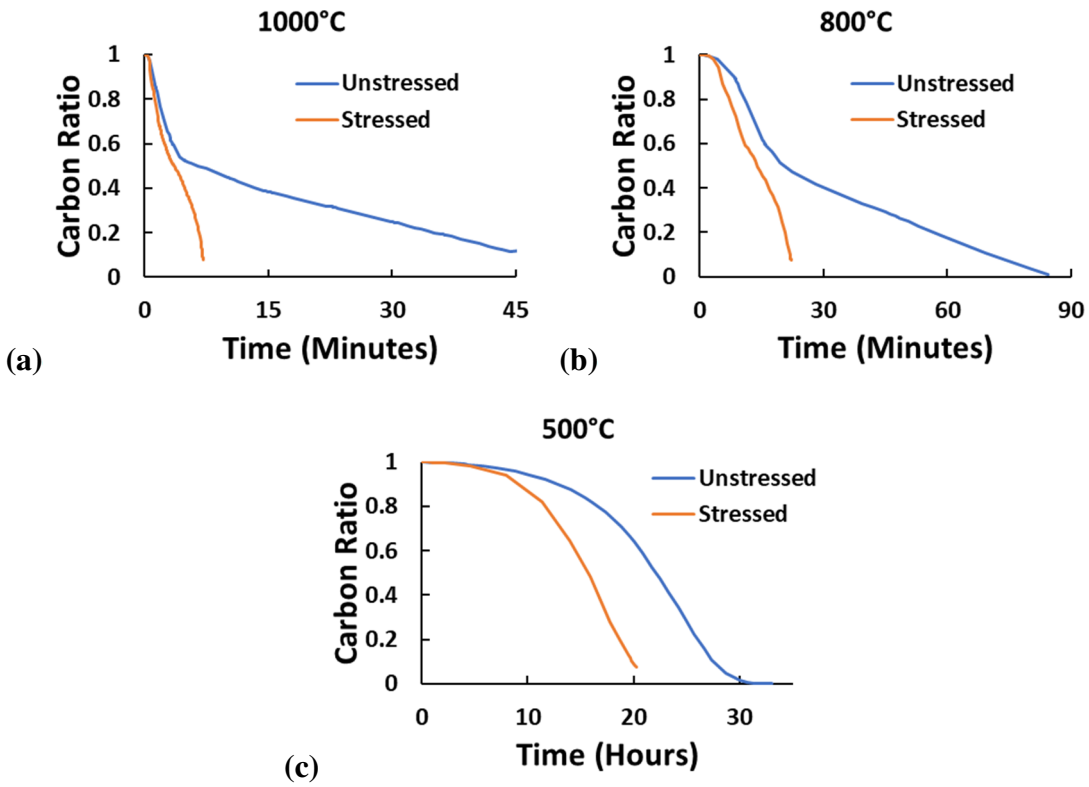

Figure 5.5. Carbon Mass Loss Curves for Stressed and Unstressed Conditions at Select Temperatures.

The differences between the reaction rate-limited and diffusion-limited regimes are demonstrated visually in Figure 5.6 by showing various state variables from simulations conducted at different temperatures. The snapshots for the 500°C simulations were taken after 14 hours and the snapshots for the 1000°C simulations were taken after 3 minutes in order to compare the differing oxidation behaviors at similar states of material degradation. The normalized carbon concentration contours show that the oxidation of the fibers in the lower temperature regime occurs around the circumference of most of the fibers simultaneously resulting in the shrinking core phenomena, whereas the oxidation of the fibers in the higher temperature regime occurs sequentially as the oxygen finds diffusive

paths through matrix cracks and oxidized fiber regions. The normalized oxygen concentration isosurfaces show a more complex distribution for the 1000°C, while for 500°C most of the SRVE contains most of the oxygen it can hold as the oxygen follows a less arduous path. The oxygen concentration plots show that oxygen is present throughout the material for the reaction-limited regime, while for the diffusion-limited regime some areas of the SRVE contain almost no oxygen at all since the system has not yet found a favorable diffusion path. Because the oxygen solubility at any location is essentially the maximum concentration of oxygen that it can contain, comparing Figure 5.6(c) to Figure 5.6(d) highlights how the SRVE at 500°C contains almost all of the oxygen that it can contain while, the SRVE at 1000°C has pockets of space that could contain oxygen due to the voids and microcracks but oxygen has not yet reached them. The axial stress contours in Figure 5.6(e) reflect the carbon concentration since areas of oxidized fibers no longer carry load. The stress evolves differently in each regime since the fibers oxidize simultaneously at the lower temperature and sequentially at the higher temperature.

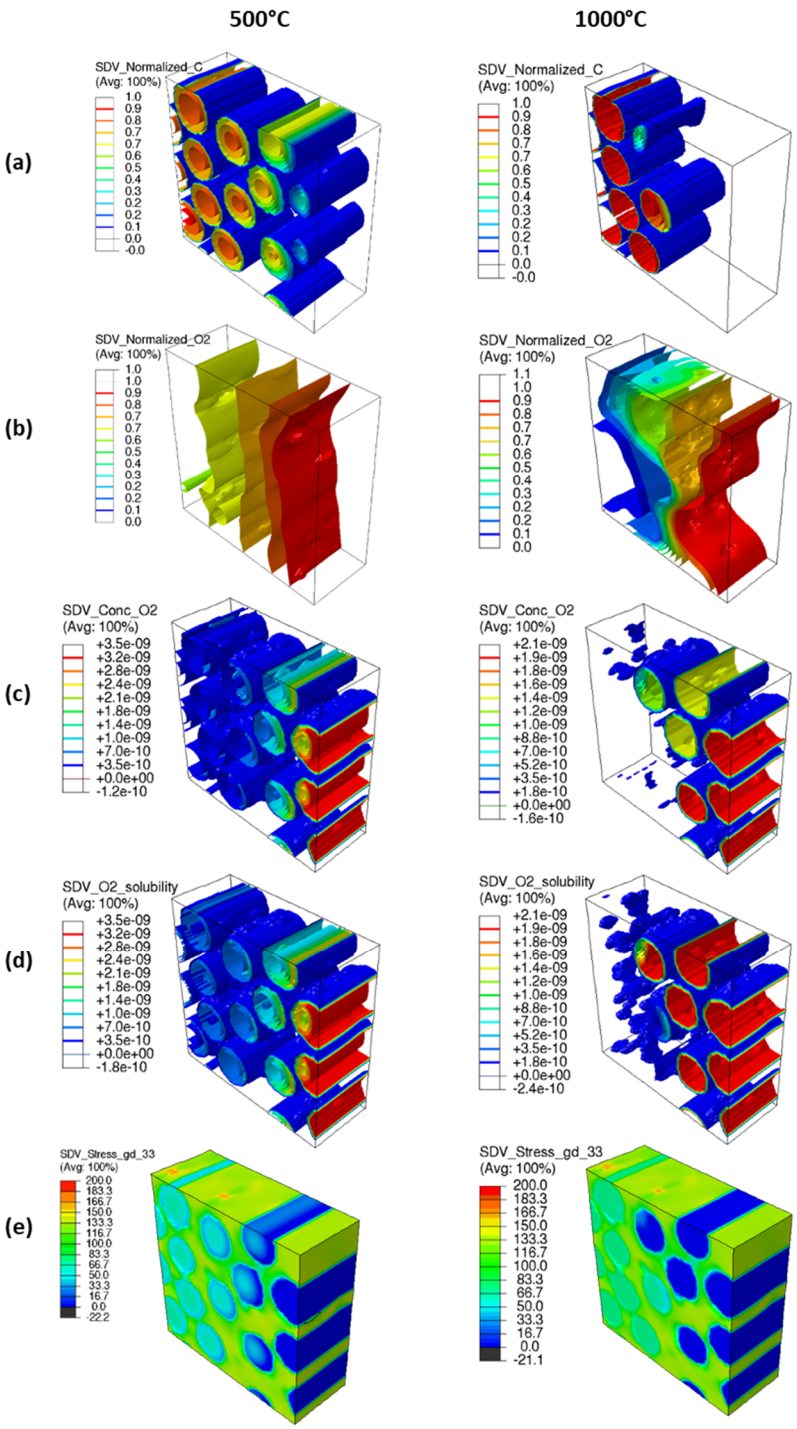

Figure 5.6. Visualization of (a) Normalized Carbon Concentration, (b) Normalized Oxygen Concentration, (c) Absolute Oxygen Concentration $\left[\frac{\text{mol}}{\text{mm}^3}\right]$, (d) Oxygen Solubility $\left[\frac{\text{mol}}{\text{mm}^3}\right]$, and (e) Stress [MPa] in the Axial Direction After 14 Hours at 500°C and After 3 Minutes at 1000°C in Si-mm Units.

To emulate the presence of an EBC, simulations were conducted using the oxygen boundary condition shown in Figure 5.2(b), which represents a surface condition where there is an exposed 0.8 μm wide crack in the coating. The strain evolution curves for stressed oxidation simulations representing a surface without an EBC and a surface with a cracked EBC are compared for select temperatures in Figure 5.7. The plots show that the strain evolution trends are similar, but there is an offset between the two types of oxygen boundary conditions. Similar to the results for stressed and unstressed conditions, the oxygen boundary conditions are more critical at higher temperatures because higher temperatures are diffusion-controlled rather than reaction-controlled. This highlights the importance of EBCs especially at the higher temperatures because even a cracked EBC significantly enhances the life of the material.

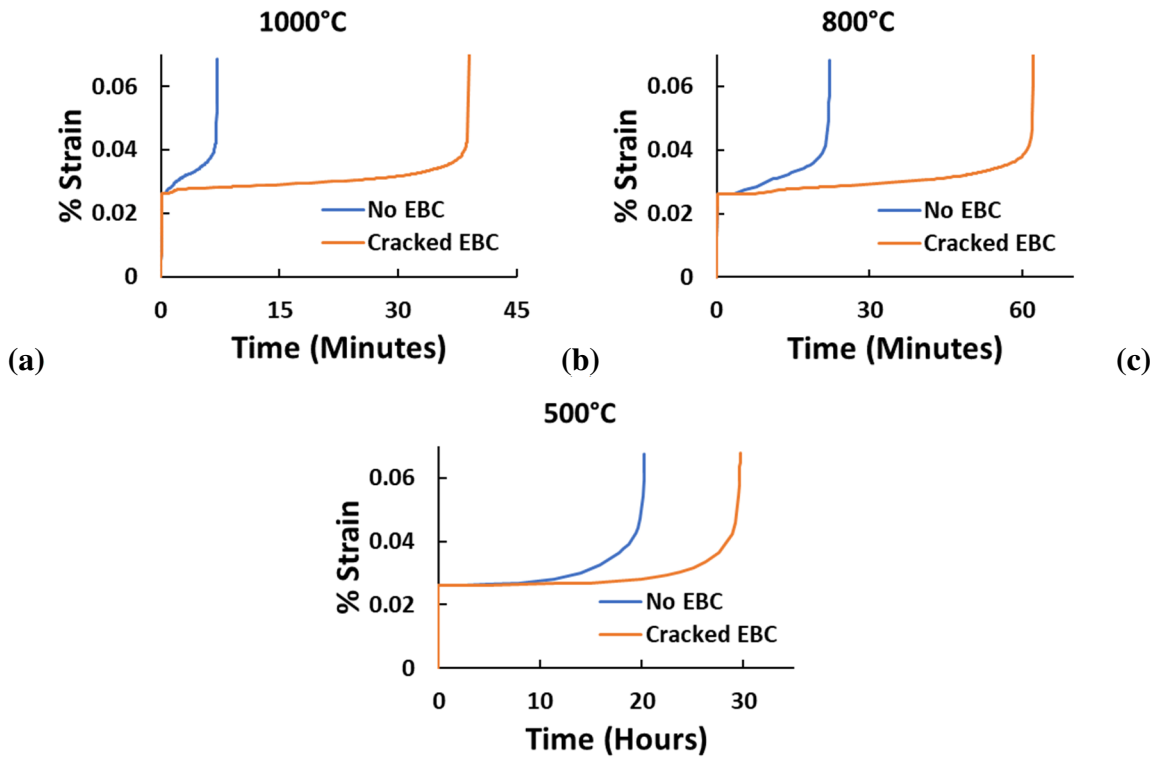

Figure 5.7. Strain Evolution Curves for Stressed Oxidation Simulations Emulating Specimens Without an Environmental Barrier Coating (EBC) and With a Cracked EBC.

The interaction between the various aspects of the model is demonstrated visually in Figure 5.8 by showing the state variables for the simulation plotted in Figure 5.7(b) that emulates the stressed oxidation of system with a cracked EBC at 800°C. The results are shown after the initial loading (10 seconds), right before the damage begins to accelerate (55 minutes), and then at the last timestep (62 minutes) to show their evolution. At the beginning of the simulation all of the fibers are intact, and there is little damage in the matrix. Consequently, the voids are the only locations where oxygen can be stored and diffused significantly. The oxygen has not yet been able to diffuse to the voids, so oxygen is only present near the initial oxygen boundary condition. After much time elapsed the oxygen successively oxidized many of the fibers, and the damage in the matrix has spread,

particularly around the fibers and preexisting voids. The solubility and diffusivity have both increased in damage regions and regions where the fibers have been oxidized. Because some of the fibers have been oxidized, the load has begun to redistribute to the matrix, increasing the stress in the matrix. As a result, the damage in the matrix spreads more rapidly, which greatly increases the diffusion of oxygen to the remaining fibers. This accelerates the degradation of the fibers, which in turn accelerates the damage in the matrix due to the associated stress transfer to the matrix. The coupled physics of this process thus captures the tertiary creep-like strain acceleration that occurs for these stressed oxidation tests.

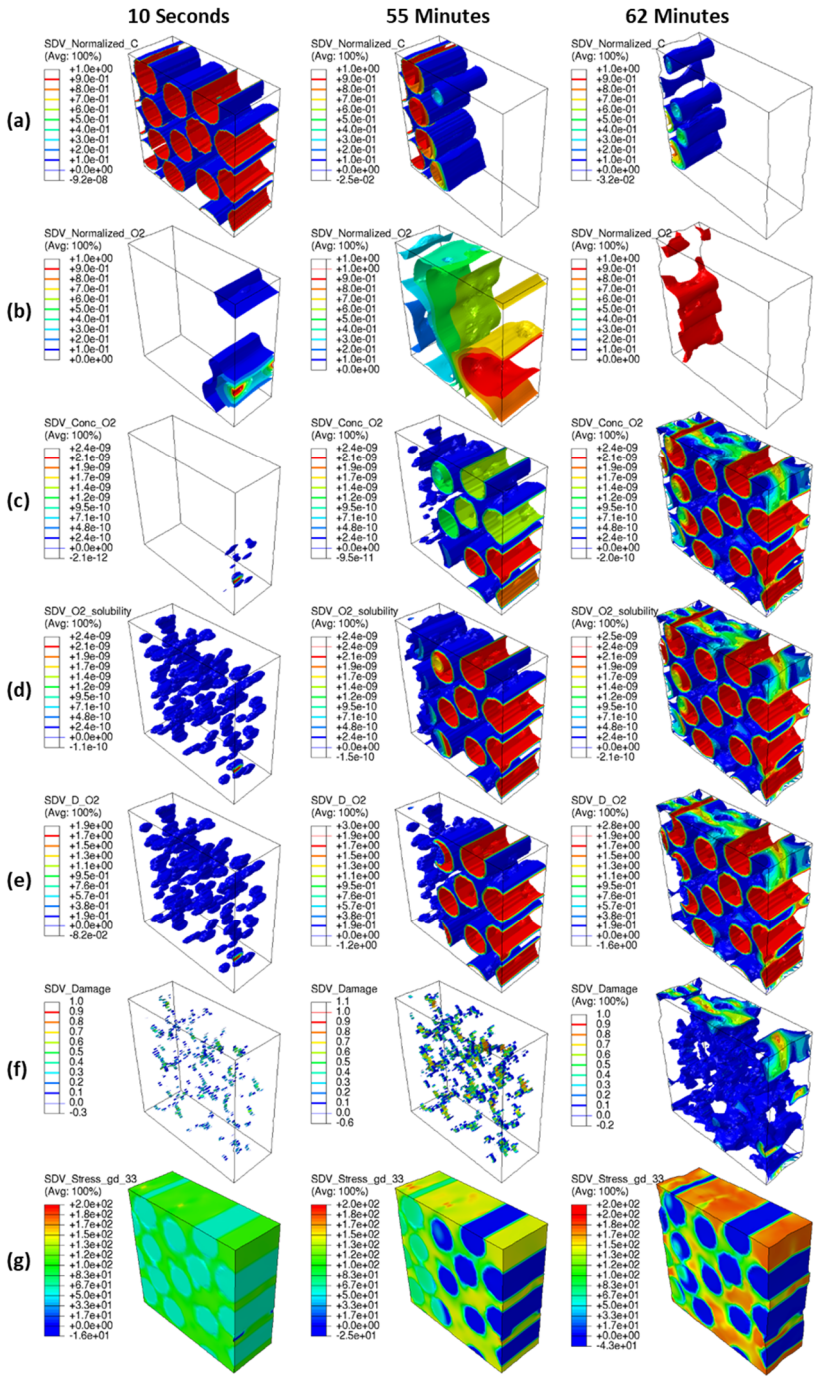

Figure 5.8. The State Variables for the System Emulating a Cracked EBC at 800°C at Three Stages of the Simulation Showing (a) the Normalized Carbon Concentration, (b) the Normalized Oxygen, (c) the Absolute Oxygen Concentration, (d) the Oxygen Solubility, (e) the Oxygen Diffusivity, (f) the Damage, and (g) the Axial Stress.

5.5. Summary

In this chapter, a multiphysics modeling methodology for the oxidation of C/SiC CMCs was presented that explicitly models oxygen diffusion through heterogeneous microstructures containing fibers and voids. The governing equations for equilibrium and conservation of mass were linked through reaction terms, oxygen diffusivities and solubilities, and matrix damage to address the complex two-way coupling between temperature, oxidation, diffusion, and the state of stress in CMCs. The developed model is implemented and tested using FEA simulations of various stressed and unstressed oxidation tests of stochastic representative microstructures. The model successfully captures TGA trends including the initial slow rate of oxidation caused by the initial formation of porosity on the fiber surfaces, purely through the physics introduced by the model, even without calibration. In addition, the model successfully captures the strain acceleration behavior of stressed oxidation experiments and explains the distinct behavior based on the complex coupling between stress, diffusion, and oxidation. The differences between the reaction-limited and diffusion-limited regimes are fundamentally demonstrated, and the effects of a compromised EBC layer are explored.

CHAPTER 6.

CONTRIBUTIONS AND FUTURE WORK

6.1. Contributions

The research presented in this dissertation was motivated by the need for an improved understanding of the thermomechanical response of advanced materials under service conditions in order to enable more intelligent, damage tolerant designs. The specific materials of interest in this dissertation are thermoset polymers, a common matrix material for fiber-reinforced composites and nanocomposites; aluminum alloy 7075-T6 (AA7075-T6), a high-performance aerospace material; and ceramic matrix composites (CMCs), an extreme-temperature material. Fundamental investigations into the properties and performance of each of these advanced materials were conducted, advancing the state of the art in several areas of research. The following are major contributions of this work:

- A novel physics-based molecular dynamics (MD) curing methodology was developed for thermoset polymers that greatly improves upon the previous conventional approaches.
- The novel curing methodology was used to study property evolution in thermoset polymers at the atomistic scale via loading and unloading simulations. Anisotropic damage mechanisms were observed and connected to void nucleation and chain alignment. The efficacy of incorporating MD damage data into multiscale models was evaluated.

- Bond breakage was shown to play a minimal role in damage initiation of thermoset polymers due to the highly localized plastic deformation mechanisms.
- Prominent size effects and surface roughness effects were isolated in AA7075-T6 under ultrasonic fatigue loading. Unique fracture features were observed under ultrasonic fatigue testing that are not observed under conventional fatigue testing of aluminum alloys.
- A multiphysics methodology was developed for modeling the complex two-way coupling stress, oxygen diffusion, and oxidation in heterogeneous CMC microstructures.
- The strain acceleration behavior of stressed oxidation experiments was demonstrated at the fundamental scale based on the complex coupling between stress, diffusion, and oxidation.

6.2. Future Work

Much of the work presented in this dissertation has the potential to continue to be explored and extended. The MD framework for modeling thermoset polymers established in Chapter 2 and explored in Chapter 3 can be applied to a variety of more complex systems with nanoinclusions to study interactions and interface mechanisms of the polymer network with various constituents in nanocomposites such as carbon nanotubes and graphene oxide. The methodology can be extended to coarse-grained MD modeling techniques to enable the modeling of thermoset polymers at larger time and length scales. Furthermore, as

computational capabilities and the accuracy and versatility of MD forcefields continue to improve, MD will likely prove to become increasingly valuable for material development and characterization; the curing and deformation study methodologies introduced in this dissertation will aid in the understanding of fundamental material behaviors without physical synthesis and testing.

The study of AA7075-T6 under ultrasonic fatigue in Chapter 4 suggested frequential dependence of fracture and failure mechanisms, but more work must be done to characterize and elucidate the distinctions between fatigue testing conducted at ultrasonic and conventional frequencies. Therefore, future work for investigating the ultrasonic fatigue of aluminum alloys investigated should include tests with direct comparability between hydraulic and ultrasonic testing, requiring similar specimens and loads tested at frequencies up to 10^7 cycles. Temperature profiles and environmental and oxidation are essential factors to consider. Similar testing should also be performed on other materials to study the material dependence of frequency dependence. Ideally, certain experimental conditions could be identified to enable direct comparability of ultrasonic fatigue testing to ultra-high cycle fatigue life at service frequencies.

Finally, the oxidation methodology presented in Chapter 5 has great potential to be extended to focus on additional mechanisms such as crack closure, creep-oxidation differentiation, anisotropic damage and diffusivity, interface degradation, residual manufacturing stress effects, water vapor diffusion and reaction, matrix oxidation, and radially nonuniform carbon fiber reaction constants. Much larger systems can be studied by reducing the element dimensionality to two-dimensions and using nonuniform mesh.

Furthermore, after determining homogenized properties for tows, the model can be applied to high-fidelity mesoscale geometries to study oxidation at higher length scales.

REFERENCES

Adams, R. C. (1987). *ASM Fractography Handbook* (Vol. 12). http://books.google.com.hk/books?id=eC-Zt1J4oCgC

Alian, A. R., Kundalwal, S. I., & Meguid, S. A. (2015). Multiscale modeling of carbon nanotube epoxy composites. *Polymer*, *70*, 149–160. https://doi.org/10.1016/j.polymer.2015.06.004

Almaraz, G. M. D., Martínez, A. G., Sánchez, R. H., Gómez, E. C., Tapia, M. G., & Juárez, J. C. V. (2017). Ultrasonic Fatigue Testing on the Polymeric Material PMMA, Used in Odontology Applications. *Procedia Structural Integrity*, *3*, 562–570. https://doi.org/10.1016/j.prostr.2017.04.039

Aluminum 7075-T6; 7075-T651. (2021). MatWeb Material Property Data. http://www.matweb.com/search/DataSheet.aspx?MatGUID=4f19a42be94546b686bbf43f79c51b7d&ckck=1

An, Q., Chen, J., Ming, W., & Chen, M. (2021). Machining of SiC ceramic matrix composites: A review. *Chinese Journal of Aeronautics*, *34*(4), 540–567. https://doi.org/10.1016/j.cja.2020.08.001

Arai, Y., Inoue, R., Goto, K., & Kogo, Y. (2019). Carbon fiber reinforced ultra-high temperature ceramic matrix composites: A review. *Ceramics International*, *45*(12), 14481–14489. https://doi.org/10.1016/j.ceramint.2019.05.065

Arcari, A., Apetre, N., Dowling, N., Meischel, M., Stanzl-Tschegg, S., Iyyer, N., & Phan, N. (2015). Variable Amplitude Fatigue Life in VHCF and Probabilistic Life Predictions. *Procedia Engineering*, *114*, 574–582. https://doi.org/10.1016/j.proeng.2015.08.107

Arcari, A., Apetre, N., Sarkar, S., Iyyer, N., Dowling, N. E., Stanzl-Tschegg, S., Vasudevan, A. K., Phan, N., & Kang, P. (2012). Influence of superimposed VHCF loadings in cyclic fatigue of 7075-T6 aluminum alloy. *Collection of Technical Papers - AIAA/ASME/ASCE/AHS/ASC Structures, Structural Dynamics and Materials Conference*, *April*, 23–26. https://doi.org/10.2514/6.2012-1732

Bale, H. A., Haboub, A., Macdowell, A. A., Nasiatka, J. R., Parkinson, D. Y., Cox, B. N., Marshall, D. B., & Ritchie, R. O. (2013). Real-time quantitative imaging of failure events in materials under load at temperatures above 1,600°C. *Nature Materials*, *12*(1), 40–46. https://doi.org/10.1038/nmat3497

Bandyopadhyay, A., Valavala, P. K., Clancy, T. C., Wise, K. E., & Odegard, G. M. (2011).

Molecular modeling of crosslinked epoxy polymers: The effect of crosslink density on thermomechanical properties. *Polymer*, *52*(11), 2445–2452. https://doi.org/10.1016/j.polymer.2011.03.052

Bathias, C., Drouillac, L., & Le François, P. (2001). How and why the fatigue S-N curve does not approach a horizontal asymptote. *International Journal of Fatigue*, *23*(SUPPL. 1), 143–151. https://doi.org/10.1016/s0142-1123(01)00123-2

Bathias, C., & Paris, P. C. (2004). Gigacycle Fatigue in Mechanical Practice. *Gigacycle Fatigue in Mechanical Practice*. https://doi.org/10.1201/9780203020609

BAXTER, D. J., & FORDHAM, R. J. (2000). The Oxidation and Corrosion Behavior of Nonoxide Ceramic Matrix Composites. In *Comprehensive Composite Materials* (pp. 221–264). https://doi.org/10.1016/b0-08-042993-9/00096-6

Bednarcyk, B. A., Stier, B., Simon, J. W., Reese, S., Pineda, E. J., & Arnold, S. M. (2014). Damage analysis of composites using a threedimensional damage model: Micro-scale architectural effects. *Proceedings of the American Society for Composites - 29th Technical Conference, ASC 2014; 16th US-Japan Conference on Composite Materials; ASTM-D30 Meeting*, *September 2015*.

Bhaumik, S. K., Sujata, M., & Venkataswamy, M. A. (2008). Fatigue failure of aircraft components. *Engineering Failure Analysis*, *15*(6), 675–694. https://doi.org/10.1016/j.engfailanal.2007.10.001

Bonora, N. (1997). A nonlinear CDM model for ductile failure. *Engineering Fracture Mechanics*, *58*(1–2), 11–28. https://doi.org/10.1016/S0013-7944(97)00074-X

Borkowski, L., & Chattopadhyay, A. (2015). Multiscale model of woven ceramic matrix composites considering manufacturing induced damage. *Composite Structures*, *126*, 62–71. https://doi.org/10.1016/j.compstruct.2015.02.015

Brandes, M. C., Mills, M. J., & Williams, J. C. (2010). The influence of slip character on the creep and fatigue fracture of an α Ti-Al alloy. *Metallurgical and Materials Transactions A: Physical Metallurgy and Materials Science*, *41*(13), 3463–3472. https://doi.org/10.1007/s11661-010-0407-z

Branicio, P. S., Kalia, R. K., Nakano, A., Vashishta, P., Shimojo, F., & Rino, J. P. (2008). Atomistic damage mechanisms during hypervelocity projectile impact on AlN: A large-scale parallel molecular dynamics simulation study. *Journal of the Mechanics and Physics of Solids*, *56*(5), 1955–1988. https://doi.org/10.1016/j.jmps.2007.11.004

Cao, A., & Wei, Y. (2007). Atomistic simulations of crack nucleation and intergranular fracture in bulk nanocrystalline nickel. *Physical Review B - Condensed Matter and Materials Physics*, *76*(2), 1–5. https://doi.org/10.1103/PhysRevB.76.024113

Caruso, M. M., Davis, D. A., Shen, Q., Odom, S. A., Sottos, N. R., White, S. R., & Moore, J. S. (2009). Mechanically-induced chemical changes in polymeric materials. *Chemical Reviews*, *109*(11), 5755–5798. https://doi.org/10.1021/cr9001353

Castelluccio, G. M., Musinski, W. D., & McDowell, D. L. (2016). Computational micromechanics of fatigue of microstructures in the HCF–VHCF regimes. *International Journal of Fatigue*, *93*, 387–396. https://doi.org/10.1016/j.ijfatigue.2016.05.019

Caton, M. J., Jones, J. W., Mayer, H., Stanzl-Tschegg, S., & Allison, J. E. (2003). Demonstration of an endurance limit in cast 319 aluminum. *Metallurgical and Materials Transactions A: Physical Metallurgy and Materials Science*, *34*(1), 33–41. https://doi.org/10.1007/s11661-003-0206-x

Chaboche, J. L. (1988a). Continuum damage mechanics: Part I-general concepts. *Journal of Applied Mechanics, Transactions ASME*, *55*(1), 59–64. https://doi.org/10.1115/1.3173661

Chaboche, J. L. (1988b). Continuum damage mechanics: Part II-damage growth, crack initiation and crack growth. *Journal of Applied Mechanics, Transactions ASME*, *55*(1), 65–72. https://doi.org/10.1115/1.3173662

Chang, W. J. (2002). Molecular-dynamics study of mechanical properties of nanoscale copper with vacancies under static and cyclic loading. *Microelectronic Engineering*, *65*(1–2), 239–246. https://doi.org/10.1016/S0167-9317(02)00887-0

Chiao, L. (1990). Mechanistic Reaction Kinetics of 4,4′-Diaminodiphenyl Sulfone Cured Tetraglycidym4,4′-diaminodiphenylmethane Epoxy Resins. *Macromolecules*, *23*(5), 1286–1290. https://doi.org/10.1021/ma00207a010

Coleman, B. D., & Gurtin, M. E. (1967). Thermodynamics with internal state variables. *The Journal of Chemical Physics*, *47*(2), 597–613. https://doi.org/10.1063/1.1711937

Crawford, E. D. ;, & Lesser, A. J. (1999). *Brittle to ductile: Fracture toughness mapping on controlled epoxy networks*. https://search-proquest-com.ezproxy1.lib.asu.edu/docview/218575659/fulltextPDF/1155D47A8B9347E4PQ/1?accountid=4485

Daniel, I. M., & Ishai, O. (2006). *Engineering Mechanics of Composite Materials 2nd Edition*. Oxford University Press. https://en.wikipedia.org/wiki/Stress_relaxation

Deal, B. E., & Grove, A. S. (1965). General relationship for the thermal oxidation of silicon. *Journal of Applied Physics*, *36*(12), 3770–3778. https://doi.org/10.1063/1.1713945

Demir, B., & Walsh, T. R. (2016). A robust and reproducible procedure for cross-linking thermoset polymers using molecular simulation. *Soft Matter*, *12*(8), 2453–2464. https://doi.org/10.1039/c5sm02788h

Deng, Y., Li, W., Ma, J., & Li, Y. (2021). Thermal-mechanical-oxidation coupled first matrix cracking stress model for fiber reinforced ceramic-matrix composites. *Journal of the European Ceramic Society*, *41*(7), 4016–4024. https://doi.org/10.1016/j.jeurceramsoc.2021.02.033

Devanathan, R., Weber, W. J., & Gale, J. D. (2010). Radiation tolerance of ceramics - Insights from atomistic simulation of damage accumulation in pyrochlores. *Energy and Environmental Science*, *3*(10), 1551–1559. https://doi.org/10.1039/c0ee00066c

Domun, N., Hadavinia, H., Zhang, T., Sainsbury, T., Liaghat, G. H., & Vahid, S. (2015). Improving the fracture toughness and the strength of epoxy using nanomaterials-a review of the current status. *Nanoscale*, *7*(23), 10294–10329. https://doi.org/10.1039/c5nr01354b

Elliott, J. A. (2011). Novel approaches to multiscale modelling in materials science. *International Materials Reviews*, *56*(4), 207–225. https://doi.org/10.1179/1743280410Y.0000000002

Engineering Toolbox. (2009). Air - Molecular Weight and Compisition. https://www.engineeringtoolbox.com/molecular-mass-air-d_679.html

Fard, M. Y., Liu, Y., & Chattopadhyay, A. (2012). *Characterization of Epoxy Resin Including Strain Rate Effects Using Digital Image Correlation System*. https://doi.org/10.1061/(ASCE)AS.1943-5525.0000127

Fu, Y., Michopoulos, J. G., & Song, J. H. (2017). On Investigating the Thermomechanical Properties of Cross-linked Epoxy Via Molecular Dynamics Analysis. *Nanoscale and Microscale Thermophysical Engineering*, *21*(1), 8–25. https://doi.org/10.1080/15567265.2016.1263696

Furuya, Y. (2011). Notable size effects on very high cycle fatigue properties of high-strength steel. *Materials Science and Engineering A*, *528*(15), 5234–5240. https://doi.org/10.1016/j.msea.2011.03.082

Gao, T., Sun, Z., Xue, H., & Retraint, D. (2020). Effect of surface mechanical attrition treatment on high cycle and very high cycle fatigue of a 7075-T6 aluminium alloy. *International Journal of Fatigue*, *139*(January), 105798. https://doi.org/10.1016/j.ijfatigue.2020.105798

Gissinger, J. R., Jensen, B. D., & Wise, K. E. (2017). Modeling chemical reactions in classical molecular dynamics simulations. *Polymer*, *128*, 211–217.

https://doi.org/10.1016/j.polymer.2017.09.038

Goldberg, R. K. (2012). Utilization of the Generalized Method of Cells to Analyze the Deformation Response of Laminated Ceramic Matrix Composites. *27th Technical Conference*. http://www.sti.nasa.gov

Goldsmith, M. B., Sankar, B. V., Haftka, R. T., & Goldberg, R. K. (2015). Effects of microstructural variability on thermo-mechanical properties of a woven ceramic matrix composite. *Journal of Composite Materials*, *49*(3), 335–350. https://doi.org/10.1177/0021998313519151

Goldsmith, M. B., Sankar, B. V, Haftka, R. T., & Goldberg, R. K. (2013). *Quantifying Effects of Voids in Woven Ceramic Matrix Composites*. *June*. https://doi.org/10.2514/6.2013-1619

Guennec, B., Ueno, A., Sakai, T., Takanashi, M., & Itabashi, Y. (2014). Effect of the loading frequency on fatigue properties of JIS S15C low carbon steel and some discussions based on micro-plasticity behavior. *International Journal of Fatigue*, *66*, 29–38. https://doi.org/10.1016/j.ijfatigue.2014.03.005

Halbig, M. C. (2008). *The influence of temperature, stress and environment on the oxidation and life of C/SiC composites*. https://doi.org/10.1002/9780470294741.ch49

Halbig, M. C., & Cawley, J. D. (2008). *Modeling the Environmental Effects on Carbon Fibers in a Ceramic Matrix at Oxidizing Conditions*. *July*, 219–226. https://doi.org/10.1002/9780470294628.ch25

Halbig, M. C., McGuffin-Cawley, J. D., Eckel, A. J., & Brewer, D. N. (2008). Oxidation kinetics and stress effects for the oxidation of continuous carbon fibers within a microcracked C/SiC ceramic matrix composite. *Journal of the American Ceramic Society*, *91*(2), 519–526. https://doi.org/10.1111/j.1551-2916.2007.02170.x

He, C., Liu, Y., Dong, J., Wang, Q., Wagner, D., & Bathias, C. (2015). Fatigue crack initiation behaviors throughout friction stir welded joints in AA7075-T6 in ultrasonic fatigue. *International Journal of Fatigue*, *81*, 171–178. https://doi.org/10.1016/j.ijfatigue.2015.07.012

Henkee, C. S., & Kramer, E. J. (1984). Crazing and Shear Deformation in Crosslinked Polystyrene. *Journal of Polymer Science. Part A-2, Polymer Physics*, *22*(4), 721–737. https://doi.org/10.1002/polb.1996.951

Henkelman, G., Uberuaga, B. P., & Jónsson, H. (2000). Climbing image nudged elastic band method for finding saddle points and minimum energy paths. *Journal of Chemical Physics*, *113*(22), 9901–9904. https://doi.org/10.1063/1.1329672

Hirschfelder, J. O. (1954). *Molecular theory of gases and liquids*. Wiley.

Holper, B., Mayer, H., Vasudevan, A. K., & Stanzl-Tschegg, S. E. (2003). Near threshold fatigue crack growth in aluminium alloys at low and ultrasonic frequency: Influences of specimen thickness, strain rate, slip behaviour and air humidity. *International Journal of Fatigue*, *25*(5), 397–411. https://doi.org/10.1016/S0142-1123(02)00163-9

Ilie, P., Lesperance, X., & Ince, A. (2020). Development of an ultrasonic fatigue testing system for gigacycle fatigue. *Material Design & Processing Communications*, *2*(6), 1–9. https://doi.org/10.1002/mdp2.120

Ismail, I. M. K. (1991). On the reactivity, structure, and porosity of carbon fibers and fabrics. *Carbon*, *29*(6), 777–792. https://doi.org/10.1016/0008-6223(91)90017-D

Jacobson, N. S., Opila, E. J., & Lee, K. N. (2001). Oxidation and corrosion of ceramics and ceramic matrix composites. *Current Opinion in Solid State and Materials Science*, *5*(4), 301–309. https://doi.org/10.1016/S1359-0286(01)00009-2

Jain, A., Ong, S. P., Hautier, G., Chen, W., Richards, W. D., Dacek, S., Cholia, S., Gunter, D., Skinner, D., Ceder, G., & Persson, K. A. (2013). Commentary: The materials project: A materials genome approach to accelerating materials innovation. In *APL Materials* (Vol. 1, Issue 1, p. 011002). American Institute of Physics. https://doi.org/10.1063/1.4812323

Jin, F.-L., Li, X., & Park, S.-J. (2015). Synthesis and application of epoxy resins: A review. *Journal of Industrial and Engineering Chemistry*, *29*, 1–11. https://doi.org/10.1016/J.JIEC.2015.03.026

Kachanov, L. M. (1986). *Introduction to Continuum Damage Mechanics*. Springer.

Karimi, A., Razaghi, R., Navidbakhsh, M., & Abdi, M. (2015). Experimental Measurement and Constitutive Modeling to Assess the Mechanical Properties of Polyvinyl Alcohol Sponge Under Uniaxial Loading. *International Journal of Advanced Biological Science and Engineering*, *2*(2), 60–77.

Khafagy, K. H., Datta, S., & Chattopadhyay, A. (2021). Multiscale characterization and representation of variability in ceramic matrix composites. *Journal of Composite Materials*, *55*(18), 2431–2441. https://doi.org/10.1177/0021998320978445

Khafagy, K. H., Sorini, C., Skinner, T., & Chattopadhyay, A. (2021). Modeling creep behavior in ceramic matrix composites. *Ceramics International*, *January*. https://doi.org/10.1016/j.ceramint.2021.01.125

Kim, Y., Sheehy, S., & Lenhardt, D. (2006). *A Survey of Aircraft Structural-Life Management Programs in the U.S. Navy, the Canadian Forces, and the U.S. Air*

Force. RAND Corporation.

Kinloch, A. J. (1985). *Mechanics and mechanisms of fracture of thermosetting epoxy polymers*. 45–67. https://doi.org/10.1007/3-540-15546-5_2

Kirkham, M. J., & Liaw, P. K. (2002). Advances in ultra-high cycle fatigue. *Proceedings of the TMS Fall Meeting*, 263–268.

Komanduri, R., Chandrasekaran, N., & Raff, L. M. (2001). Molecular Dynamics (MD) simulation of uniaxial tension of some single-crystal cubic metals at nanolevel. *International Journal of Mechanical Sciences*, *43*(10), 2237–2260. https://doi.org/10.1016/S0020-7403(01)00043-1

Koo, B., Liu, Y., Zou, J., Chattopadhyay, A., & Dai, L. L. (2014). Study of glass transition temperature (Tg) of novel stress-sensitive composites using molecular dynamic simulation. *Modelling and Simulation in Materials Science and Engineering*, *22*(6). https://doi.org/10.1088/0965-0393/22/6/065018

Koo, B., Subramanian, N., & Chattopadhyay, A. (2016). Molecular dynamics study of brittle fracture in epoxy-based thermoset polymer. *Composites Part B: Engineering*, *95*, 433–439. https://doi.org/10.1016/j.compositesb.2016.04.012

Lage, Y., de Freitas, M., Montalvão, D., Ribeiro, A. M. R., & Reis, L. (2012). Ultrasonic Fatigue Analysis on Steel Specimen With Temperature Control: Evaluation of Variable Temperature Effect. *XIII Portuguese Conference on Fracture*, 1–6.

Lamouroux, F., Bourrat, X., Nasalain, R., & Sevely, J. (1993). Structure/oxidation behavior relationship in the carbonaceous constituents of 2D-C/PyC/SiC composites. *Carbon*, *31*(8), 1273–1288. https://doi.org/10.1016/0008-6223(93)90086-P

Lamouroux, F., Naslain, R., & Jouin, J. -M. (1994). Kinetics and Mechanisms of Oxidation of 2D Woven C/SiC Composites: II, Theoretical Approach. *Journal of the American Ceramic Society*, *77*(8), 2058–2068. https://doi.org/10.1111/j.1151-2916.1994.tb07097.x

Lee, K. N., Zhu, D., & Lima, R. S. (2021). Perspectives on Environmental Barrier Coatings (EBCs) Manufactured via Air Plasma Spray (APS) on Ceramic Matrix Composites (CMCs): A Tutorial Paper. *Journal of Thermal Spray Technology*, *30*(1–2), 40–58. https://doi.org/10.1007/s11666-021-01168-0

Lee, W. S., & Lin, C. R. (2016). Deformation behavior and microstructural evolution of 7075-T6 aluminum alloy at cryogenic temperatures. *Cryogenics*, *79*, 26–34. https://doi.org/10.1016/j.cryogenics.2016.07.007

Lemaitre, J. (1996). *A Course on Damage Mechanics*. Springer.

Lesperance, X., Ilie, P., & Ince, A. (2021). Very high cycle fatigue characterization of additively manufactured AlSi10Mg and AlSi7Mg aluminium alloys based on ultrasonic fatigue testing. *Fatigue and Fracture of Engineering Materials and Structures*, *44*(3), 876–884. https://doi.org/10.1111/ffe.13406

LEWIS, M. H. (2000). Interfaces in Ceramic Matrix Composites. In *Comprehensive Composite Materials* (pp. 289–322). https://doi.org/10.1016/b0-08-042993-9/00097-8

Li, C., Jaramillo, E., & Strachan, A. (2012). Molecular dynamics simulations on cyclic deformation of an epoxy thermoset. *Polymer*, *54*(2), 881–890. https://doi.org/10.1016/j.polymer.2012.12.007

Li, C., Medvedev, G. A., Lee, E.-W., Kim, J., Caruthers, J. M., & Strachan, A. (2012). Molecular dynamics simulations and experimental studies of the thermomechanical response of an epoxy thermoset polymer. *Polymer*, *53*(19), 4222–4230. https://www-sciencedirect-com.ezproxy1.lib.asu.edu/science/article/pii/S0032386112006076#bib3

Li, C., & Strachan, A. (2010). Molecular simulations of crosslinking process of thermosetting polymers. *Polymer*, *51*(25), 6058–6070. https://doi.org/10.1016/j.polymer.2010.10.033

Li, C., & Strachan, A. (2011). Molecular dynamics predictions of thermal and mechanical properties of thermoset polymer EPON862/DETDA. *Polymer*, *52*(13), 2920–2928. https://doi.org/10.1016/j.polymer.2011.04.041

Li, C., & Strachan, A. (2015). Molecular scale simulations on thermoset polymers: A review. In *Journal of Polymer Science, Part B: Polymer Physics* (Vol. 53, Issue 2, pp. 103–122). John Wiley & Sons, Ltd. https://doi.org/10.1002/polb.23489

Li, S. X. (2012). Effects of inclusions on very high cycle fatigue properties of high strength steels. *International Materials Reviews*, *57*(2), 92–114. https://doi.org/10.1179/1743280411Y.0000000008

Liao, N., Zhang, G. Q., Pavel, D., Sluis, O. Van Der, Jansen, K. M. B., & Ernst, L. J. (2009). Investigation on thermal properties of crosslinked epoxy resin by MD simulation. *2009 10th International Conference on Thermal, Mechanical and Multi-Physics Simulation and Experiments in Microelectronics and Microsystems, EuroSimE 2009*. https://doi.org/10.1109/ESIME.2009.4938470

Lilley, J., & Holloway, D. G. (1973). Crazing in epoxy resins. *Philosophical Magazine*, *28*(1), 215–220. https://doi.org/10.1080/14786437308217443

Liu, K., Chattopadhyay, A., & Arnold, S. M. (2011). *Impact of Material and Architecture*

Model Parameters on the Failure of Woven CMCS via the Multiscale Generalized Method of Cells. *November 2011*, 175–192. https://doi.org/10.1002/9781118095393.ch17

Liu, Y., Zhao, T., Ju, W., Shi, S., Shi, S., & Shi, S. (2017). Materials discovery and design using machine learning. In *Journal of Materiomics* (Vol. 3, Issue 3, pp. 159–177). Elsevier. https://doi.org/10.1016/j.jmat.2017.08.002

Longbiao, L. (2015). Fatigue hysteresis behavior of unidirectional C/SiC ceramic-matrix composite at room and elevated temperatures. *Materials Science and Engineering A*, *625*, 1–18. https://doi.org/10.1016/j.msea.2014.11.086

Lu, L., & Shiozawa, K. (2006). S-N curve characteristics and subsurface crack initiation behaviour in ultra-long life fatigue of a high-speed tool steel. *Jixie Gongcheng Xuebao/Chinese Journal of Mechanical Engineering*, *42*(12), 89–94. https://doi.org/10.3901/JME.2006.12.089

Mall, S., & Engesser, J. M. (2006). Effects of frequency on fatigue behavior of CVI C/SiC at elevated temperature. *Composites Science and Technology*, *66*(7–8), 863–874. https://doi.org/10.1016/j.compscitech.2005.06.020

Martínez, L., Andrade, R., Birgin, E. G., & Martínez, J. M. (2009). PACKMOL: A package for building initial configurations for molecular dynamics simulations. *Journal of Computational Chemistry*, *30*(13), 2157–2164. https://doi.org/10.1002/jcc.21224

Matzenmiller, A., Lubliner, J., & Taylor, R. L. (1995). A constitutive model for anisotropic damage in fiber-composites. *Mechanics of Materials*, *20*(2), 125–152. https://doi.org/10.1016/0167-6636(94)00053-0

Mayer, H. (2006). Ultrasonic torsion and tension-compression fatigue testing: Measuring principles and investigations on 2024-T351 aluminium alloy. *International Journal of Fatigue*, *28*(11), 1446–1455. https://doi.org/10.1016/j.ijfatigue.2005.05.020

Mayer, H. (2016). Recent developments in ultrasonic fatigue. *Fatigue and Fracture of Engineering Materials and Structures*, *39*(1), 3–29. https://doi.org/10.1111/ffe.12365

Mayer, H., Papakyriacou, M., Pippan, R., & Stanzl-tschegg, S. (2001). *Influence of loading frequency on the high cycle fatigue properties of AlZnMgCu1.5 aluminium alloy*. *314*, 48–54.

Mayer, H., Schuller, R., & Fitzka, M. (2013). Fatigue of 2024-T351 aluminium alloy at different load ratios up to 10 10 cycles. *International Journal of Fatigue*, *57*, 113–119. https://doi.org/10.1016/j.ijfatigue.2012.07.013

McAllister, E. W. (2014). *Pipeline Rules of Thumb Handbook*.

https://doi.org/https://doi.org/10.1016/C2013-0-00277-0

Mei, H., Cheng, L., Zhang, L., & Xu, Y. (2007). Modeling the effects of thermal and mechanical load cycling on a C/SiC composite in oxygen/argon mixtures. *Carbon*, *45*(11), 2195–2204. https://doi.org/10.1016/j.carbon.2007.06.051

Meng, Z., Bessa, M. A., Xia, W., Kam Liu, W., & Keten, S. (2016). Predicting the Macroscopic Fracture Energy of Epoxy Resins from Atomistic Molecular Simulations. *Macromolecules*, *49*(24), 9474–9483. https://doi.org/10.1021/acs.macromol.6b01508

Mohan, K., Suresh, J. A., Ramu, P., & Jayaganthan, R. (2016). Microstructure and Mechanical Behavior of Al 7075-T6 Subjected to Shallow Cryogenic Treatment. *Journal of Materials Engineering and Performance*, *25*(6), 2185–2194. https://doi.org/10.1007/s11665-016-2052-1

Murakami, S. (1988). Mechanical modeling of material damage. *Journal of Applied Mechanics, Transactions ASME*, *55*(2), 280–286. https://doi.org/10.1115/1.3173673

Murakami, Y., Yokoyama, N. N., & Nagata, J. (2002). Mechanism of fatigue failure in ultralong life regime. *Fatigue and Fracture of Engineering Materials and Structures*, *25*(8–9), 735–746. https://doi.org/10.1046/j.1460-2695.2002.00576.x

Myung, N. J., & Choi, N. S. (2016). Dynamic stress analysis of the specimen gauge portion with a circular profile for the ultrasonic fatigue test. *International Journal of Fatigue*, *92*, 71–77. https://doi.org/10.1016/j.ijfatigue.2016.06.032

Nees, C. (1995). *Methodology for Implementing Fracture Mechanics in Global Structural Design of Aircraft*.

Neogi, A., Mitra, N., & Talreja, R. (2018). Cavitation in epoxies under composite-like stress states. *Composites Part A: Applied Science and Manufacturing*, *106*, 52–58. https://doi.org/10.1016/j.compositesa.2017.12.003

Newman, J. C. (2015). Fatigue and crack-growth analyses under Giga-cycle loading on aluminum alloys. *Procedia Engineering*, *101*(C), 339–346. https://doi.org/10.1016/j.proeng.2015.02.041

Odegard, G. M., Jensen, B. D., Gowtham, S., Wu, J., He, J., & Zhang, Z. (2014). Predicting mechanical response of crosslinked epoxy using ReaxFF. *Chemical Physics Letters*, *591*, 175–178. https://doi.org/10.1016/j.cplett.2013.11.036

Opila, E. J., & Serra, J. L. (2007). Oxidation of C/SiC Composites at Reduced Oxygen Partial Pressures. *32nd Annual Conference on Composites, Materials and Structures*.

Paolino, D. S., Tridello, A., Chiandussi, G., & Rossetto, M. (2014). On specimen design for size effect evaluation in ultrasonic gigacycle fatigue testing. *Fatigue and Fracture of Engineering Materials and Structures*, *37*(5), 570–579. https://doi.org/10.1111/ffe.12149

Papakyriacou, M., Mayer, H., Fuchs, U., Stanzl-Tschegg, S. E., & Wei, R. P. (2002). Influence of atmospheric moisture on slow fatigue crack growth at ultrasonic frequency in aluminium and magnesium alloys. *Fatigue and Fracture of Engineering Materials and Structures*, *25*(8–9), 795–804. https://doi.org/10.1046/j.1460-2695.2002.00571.x

Parthasarathy, T. A., Cox, B., Sudre, O., Przybyla, C., & Cinibulk, M. K. (2018). Modeling environmentally induced property degradation of SiC/BN/SiC ceramic matrix composites. *Journal of the American Ceramic Society*, *101*(3), 973–997. https://doi.org/10.1111/jace.15325

Patzák, B., & Jirásek, M. (2001). Consistent tangent stiffness for nonlocal material models. *Solids, Structures and Coupled Problems in Engineering*, *80*, 1279–1293.

Pilchak, A. L., Bhattacharjee, A., Rosenberger, A. H., & Williams, J. C. (2009). Low ΔK faceted crack growth in titanium alloys. *International Journal of Fatigue*, *31*(5), 989–994. https://doi.org/10.1016/j.ijfatigue.2008.03.036

Plimpton, S. (1997). Fast Parallel Algorithms for Short-Range Molecular Dynamics. *Journal of Computational Physics*, *117*(6), 1–42. https://doi.org/10.1006/jcph.1995.1039

Plummer, C. J. G., & Donald, A. M. (1991). The effect of cross-linking on crazing in polyethersulphone. *Journal of Materials Science*, *26*(5), 1165–1172. https://doi.org/10.1007/BF00544450

Potirniche, G. P., Horstemeyer, M. F., Wagner, G. J., & Gullett, P. M. (2006). A molecular dynamics study of void growth and coalescence in single crystal nickel. *International Journal of Plasticity*, *22*(2), 257–278. https://doi.org/10.1016/j.ijplas.2005.02.001

Racha, S. K. R. (2008). *Damage Characterization of four wrought aluminum alloys*. MS Thesis, Tennessee Technological University.

Rahul, R., & Kitey, R. (2016). Effect of cross-linking on dynamic mechanical and fracture behavior of epoxy variants. *Composites Part B: Engineering*, *85*, 336–342. https://doi.org/10.1016/j.compositesb.2015.09.017

Rai, A., Subramanian, N., Koo, B., & Chattopadhyay, A. (2017). Multiscale damage analysis of carbon nanotube nanocomposite using a continuum damage mechanics approach. *Journal of Composite Materials*, *51*(6), 847–858.

https://doi.org/10.1177/0021998316654304

Ramprasad, R., Batra, R., Pilania, G., Mannodi-Kanakkithodi, A., & Kim, C. (2017). Machine learning in materials informatics: Recent applications and prospects. In *npj Computational Materials* (Vol. 3, Issue 1, p. 54). Nature Publishing Group. https://doi.org/10.1038/s41524-017-0056-5

Rana, S., Alagirusamy, R., & Joshi, M. (2009). A review on carbon epoxy nanocomposites. *Journal of Reinforced Plastics and Composites*, *28*(4), 461–487. https://doi.org/10.1177/0731684407085417

Sakai, T., Lian, B., Takeda, M., Shiozawa, K., Oguma, N., Ochi, Y., Nakajima, M., & Nakamura, T. (2010). Statistical duplex S-N characteristics of high carbon chromium bearing steel in rotating bending in very high cycle regime. *International Journal of Fatigue*, *32*(3), 497–504. https://doi.org/10.1016/j.ijfatigue.2009.08.001

Sakai, T., Sato, Y., & Oguma, N. (2001). Characteristic S-N property of high carbon chromium bearing steel under axial loading in long life fatigue. *Nihon Kikai Gakkai Ronbunshu, A Hen/Transactions of the Japan Society of Mechanical Engineers, Part A*, *67*(664), 1980–1987. https://doi.org/10.1299/kikaia.67.1980

Schichtel, J. J., & Chattopadhyay, A. (2019). Modeling thermoset polymers using an improved molecular dynamics crosslinking methodology. *Computational Materials Science*, *174*(November 2019), 109469. https://doi.org/10.1016/j.commatsci.2019.109469

Schichtel, J. J., & Chattopadhyay, A. (2020). An atomistic study of damage and localized anisotropic mechanical property evolution in thermoset polymers. *International Journal of Mechanical Sciences*, *174*(November 2019), 105507. https://doi.org/10.1016/j.ijmecsci.2020.105507

Schichtel, J. J., & Chattopadhyay, A. (2022). Modeling the two-way coupling of stress, diffusion, and oxidation in heterogeneous CMC microstructures. *[Submitted Manuscript]*.

Schichtel, J. J., Datta, S., & Chattopadhyay, A. (2021). Study of Crack Initiation and Failure Mechanisms in Al 7075 T6 Alloy under Ultrasonic Fatigue. *AIAA SciTech 2021 Forum*.

Schichtel, J. J., Datta, S., & Chattopadhyay, A. (2022). Study of Aluminum Alloy 7075-T6 under Ultrasonic Fatigue Loading. *Journal of Aerospace Engineering*, *35*(4), 1–13. https://doi.org/10.1061/(asce)as.1943-5525.0001411

Schneider, N., Bödecker, J., Berger, C., & Oechsner, M. (2016). Frequency effect and influence of testing technique on the fatigue behaviour of quenched and tempered

steel and aluminium alloy. *International Journal of Fatigue*, *93*, 224–231. https://doi.org/10.1016/j.ijfatigue.2016.05.013

Seppälä, E. T., Belak, J., & Rudd, R. E. (2004). Effect of stress triaxiality on void growth in dynamic fracture of metals: A molecular dynamics study. *Physical Review B - Condensed Matter and Materials Physics*, *69*(13). https://doi.org/10.1103/PhysRevB.69.134101

Setoodeh, A. R., Attariani, H., & Khosrownejad, M. (2008). Nickel nanowires under uniaxial loads: A molecular dynamics simulation study. *Computational Materials Science*, *44*(2), 378–384. https://doi.org/10.1016/j.commatsci.2008.03.035

Shi, Q., Hsie, S. A., Jones, J. W., & Allison, J. E. (2019). Effects of alloying and processing on ultrasonic fatigue behavior in binary Ti-Al alloys. *Materials Science and Engineering A*, *756*(March), 564–577. https://doi.org/10.1016/j.msea.2019.03.079

Singh, S. K., Srinivasan, S. G., Neek-Amal, M., Costamagna, S., Van Duin, A. C. T., & Peeters, F. M. (2013). Thermal properties of fluorinated graphene. *Physical Review B - Condensed Matter and Materials Physics*, *87*(10), 2–7. https://doi.org/10.1103/PhysRevB.87.104114

Skinner, T., & Chattopadhyay, A. (2021). Multiscale temperature-dependent ceramic matrix composite damage model with thermal residual stresses and manufacturing-induced damage. *Composite Structures*, *268*(January), 114006. https://doi.org/10.1016/j.compstruct.2021.114006

Smith, M. (2009). *ABAQUS/Standard User's Manual, Version 6.9*. Dassault Systèmes Simulia Cor.

Stanzl-Tschegg, S. E., Mayer, H., Schuller, R., Przeorski, T., & Krug, P. (2012). Fatigue properties of spray formed hypereutectic aluminium silicon alloy DISPAL ® S232 at high and very high numbers of cycles. *Materials Science and Engineering A*, *538*, 327–334. https://doi.org/10.1016/j.msea.2012.01.052

Stanzl-Tschegg, S. E., Meischel, M., Arcari, A., Iyyer, N., Apetre, N., & Phan, N. (2016). Combined cycle fatigue of 7075 aluminum alloy – Fracture surface characterization and short crack propagation. *International Journal of Fatigue*, *91*, 352–362. https://doi.org/10.1016/j.ijfatigue.2015.10.022

Stukowski, A. (2010). Visualization and analysis of atomistic simulation data with OVITO-the Open Visualization Tool. *Modelling and Simulation in Materials Science and Engineering*, *18*(1). https://doi.org/10.1088/0965-0393/18/1/015012

Stukowski, A. (2014). Computational analysis methods in atomistic modeling of crystals. *Jom*, *66*(3), 399–407. https://doi.org/10.1007/s11837-013-0827-5

Subramanian, N., Koo, B., Rai, A., & Chattopadhyay, A. (2017). Molecular dynamics-based multiscale damage initiation model for CNT/epoxy nanopolymers. *Journal of Materials Science*, *53*(4), 2604–2617. https://doi.org/10.1007/s10853-017-1733-y

Subramaniyan, A. K., & Sun, C. T. (2008). Continuum interpretation of virial stress in molecular simulations. *International Journal of Solids and Structures*, *45*(14–15), 4340–4346. https://doi.org/10.1016/J.IJSOLSTR.2008.03.016

Sue, H. J., Garcia-Meitin, E. I., Yang, P. C., & Bishop, M. T. (1993). Crazing in high-performance thermoset resins. *Journal of Materials Science Letters*, *12*(18), 1463–1466. https://doi.org/10.1007/BF00591609

Sullivan, R. M. (2005). A model for the oxidation of carbon silicon carbide composite structures. *Carbon*, *43*(2), 275–285. https://doi.org/10.1016/j.carbon.2004.09.010

Sun, L., & Wagoner, R. H. (2011). Complex unloading behavior: Nature of the deformation and its consistent constitutive representation. *International Journal of Plasticity*, *27*(7), 1126–1144. https://doi.org/10.1016/j.ijplas.2010.12.003

Sun, L., Warren, G. L., O'Reilly, J. Y., Everett, W. N., Lee, S. M., Davis, D., Lagoudas, D., & Sue, H. J. (2008). Mechanical properties of surface-functionalized SWCNT/epoxy composites. *Carbon*, *46*(2), 320–328. https://doi.org/10.1016/j.carbon.2007.11.051

Sundararaghavan, V., & Lee, S. (2010). Multiscale modeling of oxidative degradation of C-SiC composite. *51st AIAA/ASME/ASCE/AHS/ASC Structures, Structural Dynamics, and Materials Conference*, *April*, 1–15.

Szlufarska, I. (2006). Atomistic simulations of nanoindentation. *Materials Today*, *9*(5), 42–50. https://doi.org/10.1016/S1369-7021(06)71496-1

Tack, J. L., & Ford, D. M. (2008). Thermodynamic and mechanical properties of epoxy resin DGEBF crosslinked with DETDA by molecular dynamics. *Journal of Molecular Graphics and Modelling*, *26*(8), 1269–1275. https://doi.org/10.1016/J.JMGM.2007.12.001

Takahashi, Y., Yoshitake, H., Nakamichi, R., Wada, T., Takuma, M., Shikama, T., & Noguchi, H. (2014). Fatigue limit investigation of 6061-T6 aluminum alloy in giga-cycle regime. *Materials Science and Engineering A*, *614*, 243–249. https://doi.org/10.1016/j.msea.2014.07.039

Tang, T., Kim, S., & Horstemeyer, M. F. (2010). Fatigue crack growth in magnesium single crystals under cyclic loading: Molecular dynamics simulation. *Computational Materials Science*, *48*(2), 426–439. https://doi.org/10.1016/j.commatsci.2010.02.003

Tracy, J. M. (2014). *Multi-scale Investigation of Damage Mechanisms in SiC/SiC Ceramic Matrix Composites.* https://deepblue.lib.umich.edu/handle/2027.42/110358

Unger, R., Braun, U., Fankhänel, J., Daum, B., Arash, B., & Rolfes, R. (2019). Molecular modelling of epoxy resin crosslinking experimentally validated by near-infrared spectroscopy. *Computational Materials Science*, *161*, 223–235. https://doi.org/10.1016/j.commatsci.2019.01.054

Van Duin, A. C. T., Dasgupta, S., Lorant, F., & Goddard, W. A. (2001). ReaxFF: A reactive force field for hydrocarbons. *Journal of Physical Chemistry A*, *105*(41), 9396–9409. https://doi.org/10.1021/jp004368u

Varshney, V., Patnaik, S. S., Roy, A. K., & Farmer, B. L. (2008). A molecular dynamics study of epoxy-based networks: Cross-linking procedure and prediction of molecular and material properties. *Macromolecules*, *41*(18), 6837–6842. https://doi.org/10.1021/ma801153e

Vashisth, A., Ashraf, C., Zhang, W., Bakis, C. E., & Van Duin, A. C. T. (2018). Accelerated ReaxFF Simulations for Describing the Reactive Cross-Linking of Polymers. *Journal of Physical Chemistry A*, *122*(32), 6633–6642. https://doi.org/10.1021/acs.jpca.8b03826

Walsh, P., Omeltchenko, A., Kalia, R. K., Nakano, A., Vashishta, P., & Saini, S. (2003). Nanoindentation of silicon nitride: A multimillion-atom molecular dynamics study. *Applied Physics Letters*, *82*(1), 118–120. https://doi.org/10.1063/1.1535263

Wang, Q. Y., Kawagoishi, N., & Chen, Q. (2006). Fatigue and fracture behaviour of structural Al-alloys up to very long life regimes. *International Journal of Fatigue*, *28*(11), 1572–1576. https://doi.org/10.1016/j.ijfatigue.2005.09.017

Wang, Q. Y., Lib, T., & Zenga, X. G. (2010). Gigacycle fatigue behavior of high strength aluminum alloys. *Procedia Engineering*, *2*(1), 65–70. https://doi.org/10.1016/j.proeng.2010.03.007

Wolf, M., Wagner, G., & Eifler, D. (2014). Fatigue and fracture behavior of MMC in the HCF- and VHCF-regime. *Materials Science Forum*, *783–786*, 1597–1602. https://doi.org/10.4028/www.scientific.net/msf.783-786.1597

Wu, C., & Xu, W. (2006). Atomistic molecular modelling of crosslinked epoxy resin. *Polymer*, *47*(16), 6004–6009. https://doi.org/10.1016/j.polymer.2006.06.025

Xu, L., Wang, Q., & Zhou, M. (2018). Micro-crack initiation and propagation in a high strength aluminum alloy during very high cycle fatigue. *Materials Science and Engineering A*, *715*(November 2017), 404–413. https://doi.org/10.1016/j.msea.2018.01.008

Xu, Y., Zhang, P., Lu, H., & Zhang, W. (2015). Numerical modeling of oxidized C/SiC microcomposite in air oxidizing environments below 800 ◦C: Microstructure and mechanical behavior. *Journal of the European Ceramic Society*, *35*(13), 3401–3409. https://doi.org/10.1016/j.jeurceramsoc.2015.05.039

Xu, Y., & Zhang, W. (2011). Numerical modelling of oxidized microstructure and degraded properties of 2D C/SiC composites in air oxidizing environments below 800°C. *Materials Science and Engineering A*, *528*(27), 7974–7982. https://doi.org/10.1016/j.msea.2011.07.037

Xue, H., Sun, Z., Zhang, X., Gao, T., & Li, Z. (2018). Very High Cycle Fatigue of a Cast Aluminum Alloy: Size Effect and Crack Initiation. *Journal of Materials Engineering and Performance*, *27*(10), 5406–5416. https://doi.org/10.1007/s11665-018-3617-y

Xue, Y., El Kadiri, H., Horstemeyer, M. F., Jordon, J. B., & Weiland, H. (2007). Micromechanisms of multistage fatigue crack growth in a high-strength aluminum alloy. *Acta Materialia*, *55*(6), 1975–1984. https://doi.org/10.1016/j.actamat.2006.11.009

Yang, S., & Qu, J. (2012). Computing thermomechanical properties of crosslinked epoxy by molecular dynamic simulations. *Polymer*, *53*(21), 4806–4817. https://doi.org/10.1016/j.polymer.2012.08.045

Yang, S., & Qu, J. (2014). Coarse-grained molecular dynamics simulations of the tensile behavior of a thermosetting polymer. *Physical Review E - Statistical, Nonlinear, and Soft Matter Physics*, *90*(1), 12601. https://doi.org/10.1103/PhysRevE.90.012601

Yashiro, K., Naito, M., Ueno, S. ichi, & Jie, F. (2010). Molecular dynamics simulation of polyethylene under cyclic loading: Effect of loading condition and chain length. *International Journal of Mechanical Sciences*, *52*(2), 136–145. https://doi.org/10.1016/j.ijmecsci.2009.08.005

Yin, Y., Binner, J. B. Z., & Cross, T. E. (1994). The oxidation behaviour of carbon fibres. *Journal of Materials Science*, *29*, 2250–2254. https://doi.org/10.1023/A:1018612214572

Yu, G., Shi, X., Wang, Y., Du, J., Ni, Z., Gao, X., Wang, F., & Song, Y. (2021). An equivalent diffusion coefficient model of the oxidation of ceramic matrix composites. *Ceramics International*, *47*(April), 20857–20866. https://doi.org/10.1016/j.ceramint.2021.04.084

Zhang, W., Srivastava, I., Zhu, Y. F., Picu, C. R., & Koratkar, N. A. (2009). Heterogeneity in epoxy nanocomposites initiates crazing: Significant improvements in fatigue resistance and toughening. *Small*, *5*(12), 1403–1407. https://doi.org/10.1002/smll.200801910

Zhao, Y., Chen, Y., He, C., Ai, S., & Fang, D. (2019). A damage-induced short-circuit diffusion model applied to the oxidation calculation of ceramic matrix composites (CMCs). *Composites Part A: Applied Science and Manufacturing*, *127*(July), 105621. https://doi.org/10.1016/j.compositesa.2019.105621

Zhu, X., Jones, J. W., & Allison, J. E. (2008). Effect of frequency, environment, and temperature on fatigue behavior of E319 cast aluminum alloy: Stress-controlled fatigue life response. *Metallurgical and Materials Transactions A: Physical Metallurgy and Materials Science*, *39*(11), 2681–2688. https://doi.org/10.1007/s11661-008-9631-1

Zoete, V., Cuendet, M. A., Grosdidier, A., & Michielin, O. (2011). SwissParam: A fast force field generation tool for small organic molecules. *Journal of Computational Chemistry*, *32*(11), 2359–2368. https://doi.org/10.1002/jcc.21816

APPENDIX A.

MULTIPHYSICS OXIDATION MODEL: DERIVATION OF DISCRETIZED WEAK FORM EQUATIONS

General Definitions

Displacement vector definition:

$$\boldsymbol{u} = \begin{bmatrix} u_x \\ u_y \\ u_z \end{bmatrix} \tag{A.1}$$

Vectorized strain definition:

$$\boldsymbol{\varepsilon} = [\varepsilon_x \quad \varepsilon_y \quad \varepsilon_z \quad 2\varepsilon_{xy} \quad 2\varepsilon_{xz} \quad 2\varepsilon_{yz}]^{\mathrm{T}} \tag{A.2}$$

Kinematic strain-displacement definition:

$$\boldsymbol{\varepsilon} = \frac{1}{2}(\boldsymbol{u}\boldsymbol{\nabla} + \boldsymbol{\nabla}\boldsymbol{u}) = \boldsymbol{\nabla}_s \boldsymbol{u} \tag{A.3}$$

Symmetric gradient definition:

$$\boldsymbol{\nabla}_s = \begin{bmatrix} \frac{\partial}{\partial x} & 0 & 0 \\ 0 & \frac{\partial}{\partial y} & 0 \\ 0 & 0 & \frac{\partial}{\partial z} \\ \frac{\partial}{\partial y} & \frac{\partial}{\partial x} & 0 \\ \frac{\partial}{\partial z} & 0 & \frac{\partial}{\partial x} \\ 0 & \frac{\partial}{\partial z} & \frac{\partial}{\partial y} \end{bmatrix} \tag{A.4}$$

Shape function approximation equation:

$$\phi \approx \boldsymbol{N}\boldsymbol{\phi}^e \tag{A.5}$$

Scattered shape function approximation equation:

$$\boldsymbol{u} \approx \mathbb{N}\boldsymbol{u}^{e} \tag{A.6}$$

Shape function definition where n_n denotes the number of nodes in an element:

$$\boldsymbol{N} = [N_1 \quad N_2 \quad \dots \quad N_{n_n}] \tag{A.7}$$

Scattered shape function definition:

$$\mathbb{N} = \begin{bmatrix} N_1 & 0 & 0 & N_2 & \dots & N_{n_n} & 0 & 0 \\ 0 & N_1 & 0 & 0 & \dots & 0 & N_{n_n} & 0 \\ 0 & 0 & N_1 & 0 & \dots & 0 & 0 & N_{n_n} \end{bmatrix} \tag{A.8}$$

Gradient of shape function definition:

$$\boldsymbol{\nabla N} = \begin{bmatrix} \dfrac{\partial N_1}{\partial x} & \dfrac{\partial N_2}{\partial x} & \dots & \dfrac{\partial N_{n_n}}{\partial x} \\ \dfrac{\partial N_1}{\partial y} & \dfrac{\partial N_2}{\partial y} & \dots & \dfrac{\partial N_{n_n}}{\partial y} \\ \dfrac{\partial N_1}{\partial z} & \dfrac{\partial N_2}{\partial z} & \dots & \dfrac{\partial N_{n_n}}{\partial z} \end{bmatrix} \tag{A.9}$$

Symmetric discrete gradient matrix definition:

$$\boldsymbol{B} = \boldsymbol{\nabla}_s \mathbb{N} = \begin{bmatrix} \dfrac{\partial N_1}{\partial x} & 0 & 0 & \dfrac{\partial N_2}{\partial x} & \dots & \dfrac{\partial N_{n_n}}{\partial x} & 0 & 0 \\ 0 & \dfrac{\partial N_1}{\partial y} & 0 & 0 & \dots & 0 & \dfrac{\partial N_{n_n}}{\partial y} & 0 \\ 0 & 0 & \dfrac{\partial N_1}{\partial z} & 0 & \dots & 0 & 0 & \dfrac{\partial N_{n_n}}{\partial z} \\ \dfrac{\partial N_1}{\partial y} & \dfrac{\partial N_1}{\partial x} & 0 & \dfrac{\partial N_2}{\partial y} & \dots & \dfrac{\partial N_{n_n}}{\partial y} & \dfrac{\partial N_{n_n}}{\partial x} & 0 \\ \dfrac{\partial N_1}{\partial z} & 0 & \dfrac{\partial N_1}{\partial x} & \dfrac{\partial N_2}{\partial z} & \dots & \dfrac{\partial N_{n_n}}{\partial z} & 0 & \dfrac{\partial N_{n_n}}{\partial x} \\ 0 & \dfrac{\partial N_1}{\partial z} & \dfrac{\partial N_1}{\partial y} & 0 & \dots & 0 & \dfrac{\partial N_{n_n}}{\partial z} & \dfrac{\partial N_{n_n}}{\partial y} \end{bmatrix} \tag{A.10}$$

A.1 Derivation of Discretized Weak Form Equations for Force Equilibrium

Strong form multiplied by arbitrary test function $\boldsymbol{w}$ and integrated over domain, where $\mathbf{w}_\mathrm{F}$ corresponds to the nodes not on the essential boundary:

$$\int_\Omega \boldsymbol{w} \cdot (\boldsymbol{\nabla} \cdot \boldsymbol{\sigma}) d\Omega = 0, \qquad \forall \mathbf{w}_\mathrm{F} \tag{A.11}$$

Integration by parts:

$$\int_\Omega \boldsymbol{\nabla} \cdot (\mathbf{w}\boldsymbol{\sigma}) d\Omega - \int_\Omega (\boldsymbol{\nabla}_\mathrm{s}\mathbf{w})^\mathrm{T} \boldsymbol{\sigma}\, d\Omega = 0, \qquad \forall \mathbf{w}_\mathrm{F} \tag{A.12}$$

Divergence theorem:

$$\int_\Gamma (\mathbf{w}\boldsymbol{\sigma}) \cdot \mathbf{n}\, d\Gamma - \int_\Omega (\boldsymbol{\nabla}_\mathrm{s}\mathbf{w})^\mathrm{T} \boldsymbol{\sigma}\, d\Omega = 0, \qquad \forall \mathbf{w}_\mathrm{F} \tag{A.13}$$

Surface traction definition natural boundary condition:

$$\int_\Gamma \mathbf{w}^\mathrm{T} \bar{\boldsymbol{t}}\, d\Gamma - \int_\Omega (\boldsymbol{\nabla}_\mathrm{s}\mathbf{w})^\mathrm{T} \boldsymbol{\sigma}\, d\Omega = 0, \qquad \forall \mathbf{w}_\mathrm{F} \tag{A.14}$$

Discretization of weak form:

$$\int_{\Gamma^e} \left(\boldsymbol{w}^{e\mathrm{T}} \mathbb{N}^\mathrm{T}\right) \bar{\boldsymbol{t}}\, d\Gamma^e - \int_{\Omega^e} \left(\boldsymbol{w}^{e\mathrm{T}} \mathbb{N}^\mathrm{T} \boldsymbol{\nabla}_s^\mathrm{T}\right) \boldsymbol{\sigma}^e\, d\Omega^e = 0, \qquad \forall \mathbf{w}_\mathrm{F} \tag{A.15}$$

$$\int_{\Gamma^e} \left(\boldsymbol{w}^{e\mathrm{T}} \mathbb{N}^\mathrm{T}\right) \bar{\boldsymbol{t}}\, d\Gamma^e - \int_{\Omega^e} \boldsymbol{w}^{e\mathrm{T}} \mathbf{B}^\mathrm{T} \boldsymbol{\sigma}^e\, d\Omega^e = 0, \qquad \forall \mathbf{w}_\mathrm{F} \tag{A.16}$$

$$\boldsymbol{w}^{e\mathrm{T}} \left(\int_{\Gamma^e} (\mathbb{N}^\mathrm{T}) \bar{\boldsymbol{t}}\, d\Gamma^e - \int_{\Omega^e} \mathbf{B}^\mathrm{T} \boldsymbol{\sigma}^e\, d\Omega^e \right) = 0, \qquad \forall \mathbf{w}_\mathrm{F} \tag{A.17}$$

A.2 Derivation of Discretized Weak Form for Conservation of Oxygen

Normalized concentration substituted in for the absolute concentration in strong form:

$$\frac{d\left(s_{(O_2)}\phi_{(O_2)}\right)}{dt} + \boldsymbol{\nabla}\cdot\left(-s_{(O_2)}D_{(O_2)}\boldsymbol{\nabla}\phi_{(O_2)}\right) - \xi_{(O_2)} = 0 \qquad \text{(A. 18)}$$

Product rule:

$$\phi_{(O_2)}\frac{ds_{(O_2)}}{dt} + s_{(O_2)}\frac{d\phi_{(O_2)}}{dt} + \boldsymbol{\nabla}\cdot\left(-s_{(O_2)}D_{(O_2)}\boldsymbol{\nabla}\phi_{(O_2)}\right) - \xi_{(O_2)} = 0 \qquad \text{(A. 19)}$$

Strong form multiplied by arbitrary test function w and integrated over domain, where w_F corresponds to the nodes not on the essential boundary:

$$\begin{aligned}\int_\Omega w\left(\phi_{(O_2)}\frac{ds_{(O_2)}}{dt} + s_{(O_2)}\frac{d\phi_{(O_2)}}{dt}\right)d\Omega + \\ \int_\Omega w\left(\boldsymbol{\nabla}\cdot\left(-s_{(O_2)}D_{(O_2)}\boldsymbol{\nabla}\phi_{(O_2)}\right)\right)d\Omega + \\ \int_\Omega w\left(-\xi_{(O_2)}\right)d\Omega = 0, \qquad \forall w_F\end{aligned} \qquad \text{(A. 20)}$$

Integration by parts:

$$\begin{aligned}\int_\Omega w\left(\phi_{(O_2)}\frac{ds_{(O_2)}}{dt} + s_{(O_2)}\frac{d\phi_{(O_2)}}{dt}\right)d\Omega + \int_\Omega \boldsymbol{\nabla}\cdot\left(w\left(-s_{(O_2)}D_{(O_2)}\boldsymbol{\nabla}\phi_{(O_2)}\right)\right)d\Omega \\ -\int_\Omega\left(-s_{(O_2)}D_{(O_2)}\boldsymbol{\nabla}\phi_{(O_2)}\right)\cdot(\boldsymbol{\nabla}w)d\Omega + \int_\Omega w\left(-\xi_{(O_2)}\right)d\Omega = 0, \qquad \forall w_F\end{aligned} \qquad \text{(A. 21)}$$

Divergence theorem

$$\begin{aligned}\int_\Omega w\left(\phi_{(O_2)}\frac{ds_{(O_2)}}{dt} + s_{(O_2)}\frac{d\phi_{(O_2)}}{dt}\right)d\Omega + \int_\Gamma\left(w\left(-s_{(O_2)}D_{(O_2)}\boldsymbol{\nabla}\phi_{(O_2)}\right)\right)\cdot\boldsymbol{n}\,d\Gamma \\ -\int_\Omega\left(-s_{(O_2)}D_{(O_2)}\boldsymbol{\nabla}\phi_{(O_2)}\right)\cdot(\boldsymbol{\nabla}w)d\Omega + \int_\Omega w\left(-\xi_{(O_2)}\right)d\Omega = 0, \qquad \forall w_F\end{aligned} \qquad \text{(A. 22)}$$

Natural flux boundary condition:

$$\int_{\Omega} w\left(\phi_{(\mathrm{O}_2)}\frac{ds_{(\mathrm{O}_2)}}{dt}+s_{(\mathrm{O}_2)}\frac{d\phi_{(\mathrm{O}_2)}}{dt}\right)d\Omega+\int_{\Gamma} w\bar{J}_{(\mathrm{O}_2)}\,d\Gamma$$
$$-\int_{\Omega}\left(-s_{(\mathrm{O}_2)}D_{(\mathrm{O}_2)}\boldsymbol{\nabla}\phi_{(\mathrm{O}_2)}\right)\cdot(\boldsymbol{\nabla}w)d\Omega+\int_{\Omega} w\left(-\xi_{(\mathrm{O}_2)}\right)d\Omega=0,\qquad \forall \mathrm{w}_{\mathrm{F}} \qquad (\mathrm{A}.23)$$

Discretization of weak form for first order reaction:

$$\int_{\Omega^e}\boldsymbol{w}^{e\mathrm{T}}\boldsymbol{N}^{\mathrm{T}}\left(\boldsymbol{N}\boldsymbol{\phi}^{e}_{(\mathrm{O}_2)}\frac{ds_{(\mathrm{O}_2)}}{dt}+s_{(\mathrm{O}_2)}\frac{d\boldsymbol{N}\boldsymbol{\phi}^{e}_{(\mathrm{O}_2)}}{dt}\right)d\Omega^e$$
$$+\int_{\Gamma^e}\boldsymbol{w}^{e\mathrm{T}}\boldsymbol{N}^{\mathrm{T}}\bar{J}_{(\mathrm{O}_2)}\,d\Gamma^e$$
$$+\int_{\Omega^e}\boldsymbol{w}^{e\mathrm{T}}(\boldsymbol{\nabla}\boldsymbol{N})^{\mathrm{T}}\left(s_{(\mathrm{O}_2)}D_{(\mathrm{O}_2)}\boldsymbol{\nabla}\boldsymbol{N}\boldsymbol{\phi}^{e}_{(\mathrm{O}_2)}\right)d\Omega^e$$
$$+\int_{\Omega^e}\boldsymbol{w}^{e\mathrm{T}}\boldsymbol{N}^{\mathrm{T}}\left(\frac{\lambda_{(\mathrm{O}_2)}}{\lambda_{(\mathrm{C})}}R_{(\mathrm{C})}s_{(\mathrm{O}_2)}\boldsymbol{N}\boldsymbol{\phi}^{e}_{(\mathrm{O}_2)}\delta_{(\mathrm{C})}\right)d\Omega^e=0,\qquad \forall\mathbf{w}_{\mathrm{F}} \qquad (\mathrm{A}.24)$$

$$\boldsymbol{w}^{e\mathrm{T}}\int_{\Omega^e}\begin{pmatrix}\boldsymbol{N}^{\mathrm{T}}\boldsymbol{N}\boldsymbol{\phi}^{e}_{(\mathrm{O}_2)}\dfrac{ds_{(\mathrm{O}_2)}}{dt}\\ +\boldsymbol{N}^{\mathrm{T}}\boldsymbol{N}s_{(\mathrm{O}_2)}\dfrac{d\boldsymbol{\phi}^{e}_{(\mathrm{O}_2)}}{dt}\\ +(\boldsymbol{\nabla}\boldsymbol{N})^{\mathrm{T}}\left(s_{(\mathrm{O}_2)}D_{(\mathrm{O}_2)}\boldsymbol{\nabla}\boldsymbol{N}\boldsymbol{\phi}^{e}_{(\mathrm{O}_2)}\right)\\ +\boldsymbol{N}^{\mathrm{T}}\left(\dfrac{\lambda_{(\mathrm{O}_2)}}{\lambda_{(\mathrm{C})}}R_{(\mathrm{C})}s_{(\mathrm{O}_2)}\boldsymbol{N}\boldsymbol{\phi}^{e}_{(\mathrm{O}_2)}\delta_{(\mathrm{C})}\right)\end{pmatrix}d\Omega^e$$
$$+\boldsymbol{w}^{e\mathrm{T}}\int_{\Gamma^e}\boldsymbol{N}^{\mathrm{T}}\bar{J}_{(\mathrm{O}_2)}\;d\Gamma^e=0,\qquad \forall\mathbf{w}_{\mathrm{F}} \qquad (\mathrm{A}.25)$$

A.3 Derivation of Discretized Weak Form Equations for Conservation of Carbon

Normalized concentration substituted in for the absolute concentration in strong form:

$$\int_{\Omega^e}\left(\frac{d\left(s_{(\mathrm{C})}\phi_{(\mathrm{C})}\right)}{dt}-\xi_{(\mathrm{C})}\right)d\Omega^e=0 \qquad (\mathrm{A}.26)$$

Simplification for constant carbon capacity:

$$\int_{\Omega^e} \left(s_{(\mathrm{C})} \frac{d\phi_{(\mathrm{C})}}{dt} \pm \xi_{(\mathrm{O}_2)} \right) d\Omega^e = 0 \tag{A. 27}$$

Strong form multiplied by test function and integrated over domain:

$$\int_{\Omega^e} w \left(s_{(\mathrm{C})} \frac{d\phi_{(\mathrm{C})}}{dt} \right) d\Omega^e + \int_{\Omega^e} w \left(-\xi_{(\mathrm{C})} \right) d\Omega^e = 0, \qquad \forall \mathrm{w_F} \tag{A. 28}$$

Discretization of weak form for first order reaction:

$$\int_{\Omega^e} \boldsymbol{w}^{e\mathrm{T}} \boldsymbol{N}^{\mathrm{T}} \left(s_{(\mathrm{C})} \frac{d\boldsymbol{N}\boldsymbol{\phi}^e_{(\mathrm{C})}}{dt} \right) d\Omega^e + \int_{\Omega^e} \boldsymbol{w}^{e\mathrm{T}} \boldsymbol{N}^{\mathrm{T}} \left(R_{(\mathrm{C})} c^n_{(\mathrm{O}_2)} \delta_{(\mathrm{C})} \right) d\Omega^e = 0, \qquad \forall \mathbf{w_F} \tag{A. 29}$$

$$\boldsymbol{w}^{e\mathrm{T}} \left(\int_{\Omega^e} \left(\boldsymbol{N}^{\mathrm{T}} \left(s_{(\mathrm{C})} \frac{d\boldsymbol{N}\boldsymbol{\phi}^e_{(\mathrm{C})}}{dt} \right) + \boldsymbol{N}^{\mathrm{T}} \left(R_{(\mathrm{C})} s_{(\mathrm{O}_2)} \boldsymbol{N}\boldsymbol{\phi}^e_{(\mathrm{O}_2)} \delta_{(\mathrm{C})} \right) \right) d\Omega^e \right) = 0, \qquad \forall \mathbf{w_F} \tag{A. 30}$$

APPENDIX B.

MULTIPHYSICS OXIDATION MODEL: FINITE ELEMENT EQUATIONS

B.1 Residuals and Jacobians for Displacement Unknowns

General form for displacement residual component:

$$\boldsymbol{F}_{\boldsymbol{u}}^{e} = \int_{\Omega^e} (\boldsymbol{B}^{\mathrm{T}} \boldsymbol{C} \boldsymbol{B} \boldsymbol{u}^{e}) d\Omega^{e} - \int_{\Gamma^e} (\mathbb{N}^{\mathrm{T}} \bar{\boldsymbol{t}})\, d\Gamma^{e} \tag{B.1}$$

Specific components of displacement residuals and Jacobians:

$$\boldsymbol{F}_{\boldsymbol{u}}^{e(\mathrm{C})} = \int_{\Omega^e} \left(\boldsymbol{B}^{\mathrm{T}} \boldsymbol{N} \boldsymbol{\phi}_{(\mathrm{C})}^{e} \boldsymbol{C}_{0}^{(\mathrm{C})} \boldsymbol{B} \boldsymbol{u}^{e} \right) d\Omega^{e} - \int_{\Gamma^e} (\mathbb{N}^{\mathrm{T}} \bar{\boldsymbol{t}})\, d\Gamma^{e} \tag{B.2}$$

$$\boldsymbol{K}_{\boldsymbol{uu}}^{e(\mathrm{C})} = -\int_{\Omega^e} \left(\boldsymbol{N} \boldsymbol{\phi}_{(\mathrm{C})}^{e} \boldsymbol{B}^{\mathrm{T}} \boldsymbol{C}_{0}^{(\mathrm{C})} \boldsymbol{B} \right) d\Omega^{e} \tag{B.3}$$

$$\boldsymbol{K}_{\boldsymbol{u}\phi_{(\mathrm{O}_2)}}^{e(\mathrm{C})} = \boldsymbol{0} \tag{B.4}$$

$$\boldsymbol{K}_{\boldsymbol{u}\phi_{(\mathrm{C})}}^{e(\mathrm{C})} = -\int_{\Omega^e} \left(\boldsymbol{B}^{\mathrm{T}} \boldsymbol{C}_{0}^{(\mathrm{C})} \boldsymbol{B} \boldsymbol{u}^{e} \boldsymbol{N} \right) d\Omega^{e} \tag{B.5}$$

$$\boldsymbol{F}_{\boldsymbol{u}}^{e(\mathrm{SiC})} = \int_{\Omega^e} \left(\boldsymbol{B}^{\mathrm{T}} (1-d) \boldsymbol{C}_{0}^{(\mathrm{SiC})} \boldsymbol{B} \boldsymbol{u}^{e} \right) d\Omega^{e} - \int_{\Gamma^e} (\mathbb{N}^{\mathrm{T}} \bar{\boldsymbol{t}})\, d\Gamma^{e} \tag{B.6}$$

$$\boldsymbol{K}_{\boldsymbol{uu}}^{e(\mathrm{SiC})} = -\int_{\Omega^e} \left(\boldsymbol{B}^{\mathrm{T}} (1-d) \boldsymbol{C}_{0}^{(\mathrm{SiC})} \boldsymbol{B} \right) d\Omega^{e} - \int_{\Omega^e} \left(\left(-\boldsymbol{B}^{\mathrm{T}} \boldsymbol{C}_{0}^{(\mathrm{SiC})} \boldsymbol{B} \boldsymbol{u}^{e} \right) \frac{\boldsymbol{\partial} d}{\boldsymbol{\partial} \boldsymbol{\varepsilon}} \boldsymbol{B} \right) d\Omega^{e} \tag{B.7}$$

$$\boldsymbol{K}_{\boldsymbol{u}\phi_{(\mathrm{O}_2)}}^{e(\mathrm{SiC})} = \boldsymbol{K}_{\boldsymbol{u}\phi_{(\mathrm{C})}}^{e(\mathrm{SiC})} = \boldsymbol{0} \tag{B.8}$$

$$\boldsymbol{F}_{\boldsymbol{u}}^{e(\mathrm{void})} = \int_{\Omega^e} \left(\boldsymbol{B}^{\mathrm{T}} \boldsymbol{C}_{0}^{(\mathrm{void})} \boldsymbol{B} \boldsymbol{u}^{e} \right) d\Omega^{e} - \int_{\Gamma^e} (\mathbb{N}^{\mathrm{T}} \bar{\boldsymbol{t}})\, d\Gamma^{e} \tag{B.9}$$

$$\boldsymbol{K}_{\boldsymbol{uu}}^{e(\mathrm{void})} = -\int_{\Omega^e} \left(\boldsymbol{B}^{\mathrm{T}} \boldsymbol{C}_{0}^{(\mathrm{void})} \boldsymbol{B} \right) d\Omega^{e} \tag{B.10}$$

$$\boldsymbol{K}_{\boldsymbol{u}\phi_{(\mathrm{O}_2)}}^{e(\mathrm{void})} = \boldsymbol{K}_{\boldsymbol{u}\phi_{(\mathrm{C})}}^{e(\mathrm{void})} = \boldsymbol{0} \tag{B. 11}$$

B.2 Residuals and Jacobians for Normalized Oxygen Concentration Unknowns

General form for normalized oxygen concentration residual component:

$$\boldsymbol{F}_{\phi_{(\mathrm{O}_2)}}^{e} = \int_{\Omega^e} \begin{pmatrix} \boldsymbol{N}^{\mathrm{T}}\boldsymbol{N}\boldsymbol{\phi}_{(\mathrm{O}_2)}^{e}\dfrac{ds_{(\mathrm{O}_2)}}{dt} \\ +\boldsymbol{N}^{\mathrm{T}}\boldsymbol{N}s_{(\mathrm{O}_2)}\dfrac{d\boldsymbol{\phi}_{(\mathrm{O}_2)}^{e}}{dt} \\ +(\boldsymbol{\nabla N})^{\mathrm{T}}(\boldsymbol{\nabla N})\boldsymbol{\phi}_{(\mathrm{O}_2)}^{e}s_{(\mathrm{O}_2)}D_{(\mathrm{O}_2)} \\ +\boldsymbol{N}^{\mathrm{T}}\left(\dfrac{\lambda_{(\mathrm{O}_2)}}{\lambda_{(\mathrm{C})}}R_{(\mathrm{C})}s_{(\mathrm{O}_2)}\boldsymbol{N}\boldsymbol{\phi}_{(\mathrm{O}_2)}^{e}\delta_{(\mathrm{C})}\right) \end{pmatrix} d\Omega^e + \int_{\Gamma^e} \boldsymbol{N}^{\mathrm{T}}\bar{J}_{(\mathrm{O}_2)}\ d\Gamma^e \tag{B. 12}$$

Specific components of normalized oxygen concentration residuals and Jacobians:

$$\boldsymbol{F}_{\phi_{(\mathrm{O}_2)}}^{e(\mathrm{C})} = \int_{\Omega^e} \begin{pmatrix} \boldsymbol{N}^{\mathrm{T}}\boldsymbol{N}\boldsymbol{\phi}_{(\mathrm{O}_2)}^{e}\left(-\left(s_{max_{(\mathrm{O}_2)}} - s_{min_{(\mathrm{O}_2)}}^{(\mathrm{C})}\right)\boldsymbol{N}\right)\dfrac{d\boldsymbol{\phi}_{(\mathrm{C})}^{e}}{dt} \\ +\boldsymbol{N}^{\mathrm{T}}\boldsymbol{N}\left(-\left(s_{max_{(\mathrm{O}_2)}} - s_{min_{(\mathrm{O}_2)}}^{(\mathrm{C})}\right)\boldsymbol{N}\boldsymbol{\phi}_{(\mathrm{C})}^{e} + s_{max_{(\mathrm{O}_2)}}\right)\dfrac{d\boldsymbol{\phi}_{(\mathrm{O}_2)}^{e}}{dt} \\ +(\boldsymbol{\nabla N})^{\mathrm{T}}(\boldsymbol{\nabla N})\boldsymbol{\phi}_{(\mathrm{O}_2)}^{e}\begin{pmatrix}\left(-\left(s_{max_{(\mathrm{O}_2)}} - s_{min_{(\mathrm{O}_2)}}^{(\mathrm{C})}\right)\boldsymbol{N}\boldsymbol{\phi}_{(\mathrm{C})}^{e} + s_{max_{(\mathrm{O}_2)}}\right) \\ *\left(-\left(D_{max_{(\mathrm{O}_2)}}^{(\mathrm{C})} - D_{min_{(\mathrm{O}_2)}}^{(\mathrm{C})}\right)\boldsymbol{N}\boldsymbol{\phi}_{(\mathrm{C})}^{e} + D_{max_{(\mathrm{O}_2)}}^{(\mathrm{C})}\right)\end{pmatrix} \\ +\boldsymbol{N}^{\mathrm{T}}\left(\dfrac{\lambda_{(\mathrm{O}_2)}}{\lambda_{(\mathrm{C})}}R_{(\mathrm{C})}\left(-\left(s_{max_{(\mathrm{O}_2)}} - s_{min_{(\mathrm{O}_2)}}^{(\mathrm{C})}\right)\boldsymbol{N}\boldsymbol{\phi}_{(\mathrm{C})}^{e} + s_{max_{(\mathrm{O}_2)}}\right)\boldsymbol{N}\boldsymbol{\phi}_{(\mathrm{O}_2)}^{e}\delta_{(\mathrm{C})}\right) \end{pmatrix} d\Omega^e + \int_{\Gamma^e} \boldsymbol{N}^{\mathrm{T}}\bar{J}_{(\mathrm{O}_2)}\ d\Gamma^e \tag{B. 13}$$

$$\boldsymbol{K}_{\phi_{(\mathrm{O}_2)}\boldsymbol{u}}^{e(\mathrm{C})} = \boldsymbol{0} \tag{B. 14}$$

$$\boldsymbol{K}^{e(\mathrm{C})}_{\phi_{(\mathrm{O}_2)}\phi_{(\mathrm{O}_2)}} =$$

$$-\int_{\Omega^e}\begin{pmatrix}\boldsymbol{N}^{\mathrm{T}}\boldsymbol{N}\left(-\left(s_{max_{(\mathrm{O}_2)}}-s_{min^{(\mathrm{C})}_{(\mathrm{O}_2)}}\right)\boldsymbol{N}\dfrac{d\boldsymbol{\phi}^e_{(\mathrm{C})}}{dt}\right)+\boldsymbol{N}^{\mathrm{T}}\boldsymbol{N}s^{(\mathrm{C})}_{(\mathrm{O}_2)}\dfrac{1}{\Delta t}\\ +(\boldsymbol{\nabla N})^{\mathrm{T}}\left(s^{(\mathrm{C})}_{(\mathrm{O}_2)}D^{(\mathrm{C})}_{(\mathrm{O}_2)}(\boldsymbol{\nabla N})\right)+\boldsymbol{N}^{\mathrm{T}}\left(\dfrac{\lambda_{(\mathrm{O}_2)}}{\lambda_{(\mathrm{C})}}R_{(\mathrm{C})}s^{(\mathrm{C})}_{(\mathrm{O}_2)}\boldsymbol{N}\delta_{(\mathrm{C})}\right)\end{pmatrix}d\Omega^e \qquad \text{(B. 15)}$$

$$\boldsymbol{K}^{e(\mathrm{C})}_{\phi_{(\mathrm{O}_2)}\phi_{(\mathrm{C})}} =$$

$$-\int_{\Omega^e}\begin{pmatrix}\boldsymbol{N}^{\mathrm{T}}\boldsymbol{N}\boldsymbol{\phi}^e_{(\mathrm{O}_2)}\left(-\left(s_{max_{(\mathrm{O}_2)}}-s_{min^{(\mathrm{C})}_{(\mathrm{O}_2)}}\right)\boldsymbol{N}\right)\dfrac{1}{\Delta t}\\ +\boldsymbol{N}^{\mathrm{T}}\boldsymbol{N}\left(-\left(s_{max_{(\mathrm{O}_2)}}-s_{min^{(\mathrm{C})}_{(\mathrm{O}_2)}}\right)\boldsymbol{N}\right)\dfrac{d\boldsymbol{\phi}^e_{(\mathrm{O}_2)}}{dt}\\ +(\boldsymbol{\nabla N})^{\mathrm{T}}(\boldsymbol{\nabla N})\boldsymbol{\phi}^e_{(\mathrm{O}_2)}\boldsymbol{N}\begin{pmatrix}-\left(s_{max_{(\mathrm{O}_2)}}-s_{min^{(\mathrm{C})}_{(\mathrm{O}_2)}}\right)D^{(\mathrm{C})}_{(\mathrm{O}_2)}\\ -\left(D_{max^{(\mathrm{C})}_{(\mathrm{O}_2)}}-D_{min^{(\mathrm{C})}_{(\mathrm{O}_2)}}\right)s^{(\mathrm{C})}_{(\mathrm{O}_2)}\end{pmatrix}\\ +\boldsymbol{N}^{\mathrm{T}}\boldsymbol{N}\left(\dfrac{\lambda_{(\mathrm{O}_2)}}{\lambda_{(\mathrm{C})}}R_{(\mathrm{C})}\left(-\left(s_{max_{(\mathrm{O}_2)}}-s_{min^{(\mathrm{C})}_{(\mathrm{O}_2)}}\right)\right)\boldsymbol{N}\boldsymbol{\phi}^e_{(\mathrm{O}_2)}\delta_{(\mathrm{C})}\right)\end{pmatrix}d\Omega^e \qquad \text{(B. 16)}$$

$$\boldsymbol{F}^{e(\mathrm{SiC})}_{\phi_{(\mathrm{O}_2)}} =$$

$$\int_{\Omega^e}\begin{pmatrix}\boldsymbol{N}^{\mathrm{T}}\boldsymbol{N}\boldsymbol{\phi}^e_{(\mathrm{O}_2)}\left(s_{max_{(\mathrm{O}_2)}}-s_{min^{(\mathrm{SiC})}_{(\mathrm{O}_2)}}\right)\dfrac{\partial d}{\partial\boldsymbol{\varepsilon}}\boldsymbol{B}\dfrac{d\boldsymbol{u}^e}{dt}\\ +\boldsymbol{N}^{\mathrm{T}}\boldsymbol{N}\left(\left(s_{max_{(\mathrm{O}_2)}}-s_{min^{(\mathrm{SiC})}_{(\mathrm{O}_2)}}\right)d+s_{min^{(\mathrm{SiC})}_{(\mathrm{O}_2)}}\right)\dfrac{d\boldsymbol{\phi}^e_{(\mathrm{O}_2)}}{dt}\\ +(\boldsymbol{\nabla N})^{\mathrm{T}}(\boldsymbol{\nabla N})\boldsymbol{\phi}^e_{(\mathrm{O}_2)}\begin{pmatrix}\left(\left(s_{max_{(\mathrm{O}_2)}}-s_{min^{(\mathrm{SiC})}_{(\mathrm{O}_2)}}\right)d+s_{min^{(\mathrm{SiC})}_{(\mathrm{O}_2)}}\right)\\ *\left(\left(D_{max^{(\mathrm{SiC})}_{(\mathrm{O}_2)}}-D_{min^{(\mathrm{SiC})}_{(\mathrm{O}_2)}}\right)d+D_{min^{(\mathrm{SiC})}_{(\mathrm{O}_2)}}\right)\end{pmatrix}\\ +\boldsymbol{N}^{\mathrm{T}}\left(\dfrac{\lambda_{(\mathrm{O}_2)}}{\lambda_{(\mathrm{C})}}R_{(\mathrm{C})}\left(\left(s_{max_{(\mathrm{O}_2)}}-s_{min^{(\mathrm{SiC})}_{(\mathrm{O}_2)}}\right)d+s_{min^{(\mathrm{SiC})}_{(\mathrm{O}_2)}}\right)\boldsymbol{N}\boldsymbol{\phi}^e_{(\mathrm{O}_2)}\delta_{(\mathrm{C})}\right)\end{pmatrix}d\Omega^e$$

$$+\int_{\Gamma^e}\boldsymbol{N}^{\mathrm{T}}\bar{J}_{(\mathrm{O}_2)}\,d\Gamma^e \qquad \text{(B. 17)}$$

$$\boldsymbol{K}^{e\,(\mathrm{SiC})}_{\phi_{(\mathrm{O}_2)}\boldsymbol{u}} =$$

$$-\int_{\Omega^e}\begin{pmatrix}\boldsymbol{N}^{\mathrm{T}}\boldsymbol{N}\boldsymbol{\phi}^e_{(\mathrm{O}_2)}\left(s_{max_{(\mathrm{O}_2)}}-s_{min^{(\mathrm{SiC})}_{(\mathrm{O}_2)}}\right)\dfrac{\partial d}{\partial\boldsymbol{\varepsilon}}\boldsymbol{B}\dfrac{1}{\Delta t}\\ +\boldsymbol{N}^{\mathrm{T}}\boldsymbol{N}\dfrac{d\boldsymbol{\phi}^e_{(\mathrm{O}_2)}}{dt}\left(\left(s_{max_{(\mathrm{O}_2)}}-s_{min^{(\mathrm{SiC})}_{(\mathrm{O}_2)}}\right)\dfrac{\partial d}{\partial\boldsymbol{\varepsilon}}\boldsymbol{B}\right)\\ +(\boldsymbol{\nabla N})^{\mathrm{T}}(\boldsymbol{\nabla N})\boldsymbol{\phi}^e_{(\mathrm{O}_2)}\begin{pmatrix}D^{(\mathrm{SiC})}_{(\mathrm{O}_2)}\left(s_{max_{(\mathrm{O}_2)}}-s_{min^{(\mathrm{SiC})}_{(\mathrm{O}_2)}}\right)\dfrac{\partial d}{\partial\boldsymbol{\varepsilon}}\boldsymbol{B}\\ +s^{(\mathrm{SiC})}_{(\mathrm{O}_2)}\left(D_{max^{(\mathrm{SiC})}_{(\mathrm{O}_2)}}-D_{min^{(\mathrm{SiC})}_{(\mathrm{O}_2)}}\right)\dfrac{\partial d}{\partial\boldsymbol{\varepsilon}}\boldsymbol{B}\end{pmatrix}\end{pmatrix}d\Omega^e \tag{B. 18}$$

$$\boldsymbol{K}^{e\,(\mathrm{SiC})}_{\phi_{(\mathrm{O}_2)}\phi_{(\mathrm{O}_2)}} =$$

$$-\int_{\Omega^e}\begin{pmatrix}\boldsymbol{N}^{\mathrm{T}}\boldsymbol{N}\left(\left(s_{max_{(\mathrm{O}_2)}}-s_{min^{(\mathrm{SiC})}_{(\mathrm{O}_2)}}\right)\dfrac{\partial d}{\partial\boldsymbol{\varepsilon}}\boldsymbol{B}\dfrac{d\boldsymbol{u}^e}{dt}\right)\\ +\boldsymbol{N}^{\mathrm{T}}\boldsymbol{N}s^{(\mathrm{SiC})}_{(\mathrm{O}_2)}\dfrac{1}{\Delta t}\\ +(\boldsymbol{\nabla N})^{\mathrm{T}}\left(s^{(\mathrm{SiC})}_{(\mathrm{O}_2)}D^{(\mathrm{SiC})}_{(\mathrm{O}_2)}(\boldsymbol{\nabla N})\right)\end{pmatrix}d\Omega^e \tag{B. 19}$$

$$\boldsymbol{K}^{e\,(\mathrm{SiC})}_{\phi_{(\mathrm{O}_2)}\phi_{(\mathrm{C})}} = \boldsymbol{0} \tag{B. 20}$$

$$\boldsymbol{F}^{e\,(\mathrm{void})}_{\phi_{(\mathrm{O}_2)}} =$$

$$\int_{\Omega^e}\begin{pmatrix}\boldsymbol{N}^{\mathrm{T}}\boldsymbol{N}s_{max_{(\mathrm{O}_2)}}\dfrac{d\boldsymbol{\phi}^e_{(\mathrm{O}_2)}}{dt}\\ +(\boldsymbol{\nabla N})^{\mathrm{T}}\left(s_{max_{(\mathrm{O}_2)}}D^{(\mathrm{void})}_{max_{(\mathrm{O}_2)}}(\boldsymbol{\nabla N})\boldsymbol{\phi}^e_{(\mathrm{O}_2)}\right)\end{pmatrix}d\Omega^e+\int_{\Gamma^e}\boldsymbol{N}^{\mathrm{T}}\bar{J}_{(\mathrm{O}_2)}\,d\Gamma^e \tag{B. 21}$$

$$\boldsymbol{K}^{e\,(\mathrm{void})}_{\phi_{(\mathrm{O}_2)}\boldsymbol{u}} = \boldsymbol{0} \tag{B. 22}$$

$$\boldsymbol{K}^{e\,(\mathrm{void})}_{\phi_{(\mathrm{O}_2)}\phi_{(\mathrm{O}_2)}} = -\int_{\Omega^e}\begin{pmatrix}\boldsymbol{N}^{\mathrm{T}}\boldsymbol{N}s_{max_{(\mathrm{O}_2)}}\dfrac{1}{\Delta t}\\ +(\boldsymbol{\nabla N})^{\mathrm{T}}\left(s_{max_{(\mathrm{O}_2)}}D^{(\mathrm{void})}_{max_{(\mathrm{O}_2)}}(\boldsymbol{\nabla N})\right)\end{pmatrix}d\Omega^e \tag{B. 23}$$

$$\boldsymbol{K}^{e\,(\mathrm{void})}_{\phi_{(\mathrm{O}_2)}\phi_{(\mathrm{C})}} = \boldsymbol{0} \tag{B. 24}$$

B.3 Residuals and Jacobians for Normalized Carbon Concentration Unknowns

General form for normalized carbon concentration residual component:

$$\boldsymbol{F}^{e}_{\phi_{(\mathrm{C})}} = \int_{\Omega^e} \left(\boldsymbol{N}^{\mathrm{T}} \boldsymbol{N} s_{(\mathrm{C})} \frac{d\boldsymbol{\phi}^{e}_{(\mathrm{C})}}{dt} + \boldsymbol{N}^{\mathrm{T}} R_{(\mathrm{C})} s_{(\mathrm{O}_2)} \boldsymbol{N} \boldsymbol{\phi}^{e}_{(\mathrm{O}_2)} \delta_{(\mathrm{C})} \right) d\Omega^e \tag{B.25}$$

Specific components of normalized carbon concentration residuals and Jacobians:

$$\boldsymbol{F}^{e^{(\mathrm{C})}}_{\phi_{(\mathrm{C})}} = \int_{\Omega^e} \begin{pmatrix} \boldsymbol{N}^{\mathrm{T}} \boldsymbol{N} \left(c_{0\,(\mathrm{C})} \dfrac{d\boldsymbol{\phi}^{e}_{(\mathrm{C})}}{dt} \right) \\ + \boldsymbol{N}^{\mathrm{T}} \left(R_{(\mathrm{C})} \left(- \left(s_{max\,(\mathrm{O}_2)} - s_{min\,(\mathrm{O}_2)}^{(\mathrm{C})} \right) \phi_{(\mathrm{C})} + s_{max\,(\mathrm{O}_2)} \right) \boldsymbol{N} \boldsymbol{\phi}^{e}_{(\mathrm{O}_2)} \delta_{(\mathrm{C})} \right) \end{pmatrix} d\Omega^e \tag{B.26}$$

$$\boldsymbol{K}^{e^{(\mathrm{C})}}_{\phi_{(\mathrm{C})}\boldsymbol{u}} = \boldsymbol{0} \tag{B.27}$$

$$\boldsymbol{K}^{e^{(\mathrm{C})}}_{\phi_{(\mathrm{C})}\phi_{(\mathrm{O}_2)}} = - \int_{\Omega^e} \boldsymbol{N}^{\mathrm{T}} \left(R_{(\mathrm{C})} \left(- \left(s_{max\,(\mathrm{O}_2)} - s_{min\,(\mathrm{O}_2)}^{(\mathrm{C})} \right) \phi_{(\mathrm{C})} + s_{max\,(\mathrm{O}_2)} \right) \boldsymbol{N} \delta_{(\mathrm{C})} \right) d\Omega^e \tag{B.28}$$

$$\boldsymbol{K}^{e^{(\mathrm{C})}}_{\phi_{(\mathrm{C})}\phi_{(\mathrm{C})}} = - \int_{\Omega^e} \boldsymbol{N}^{\mathrm{T}} \boldsymbol{N} c_{0\,(\mathrm{C})} \frac{1}{\Delta t} d\Omega^e \tag{B.29}$$

$$\boldsymbol{F}^{e^{(\mathrm{SiC})}}_{\phi_{(\mathrm{C})}} = \boldsymbol{F}^{e^{(\mathrm{void})}}_{\phi_{(\mathrm{C})}} = \boldsymbol{0} \tag{B.30}$$

$$\boldsymbol{K}^{e^{(\mathrm{SiC})}} = \boldsymbol{K}^{e^{(\mathrm{void})}} = \boldsymbol{0} \tag{B.31}$$